Generalized Frequency Plane Model of Integrated Electromagnetic Power Passives

by

Lingyin Zhao

Dissertation submitted to the Faculty of the Virginia Polytechnic Institute and State University in partial fulfillment of the requirements for the degree of

DOCTOR OF PHILOSOPHY
in
ELECTRICAL ENGINEERING

Prof. J.D. van Wyk, Chair

Prof. W. G. Odendaal

Prof. Alex. Q. Huang

Prof. G. Q. Lu

Prof. Yilu Liu

May. 2004
Blacksburg, Virginia

Keywords: Integrated Passives, Transmission Line, Generalized Transmission Structure, Frequency Plane Modeling, Multi-cell Structure Integrated Passives, Integrated RF-EMI Filter

Copyright 2004, Lingyin Zhao

Generalized Frequency Plane Model of Integrated Electromagnetic Power Passives

Lingyin Zhao

Abstract

The challenge to put power electronics on the same cost reduction spiral as integrated signal electronics has yet to be met. In the ongoing work for achieving complete power electronic converter integration, it has proven to be essential to develop a technology for integration of electromagnetic power passives. This integration will enable the incorporation of resonant circuits, transformers, EMI filters and the like into the integrated power electronics modules. These integrated electromagnetic power passives have been realized in terms of distributed structures, utilizing magnetic layers, conductive layers and dielectric layers. Because of the compact structures and the special implementation techniques of these integrated modules, the high frequency parasitic resonance are normally significant and may have negative impact on the performance and EMI characteristics. However, the existing modeling technique can only predict the fundamental resonant frequency and showed neither the causes of the high frequency resonance nor how to calculate those accurately.

In this dissertation, comprehensive research work towards higher order electromagnetic modeling of integrated passive components is presented. Firstly, an L-C cell is identified as the basic building block of integrated passives such as an integrated series resonator. As an essential mistake in the structure evolution process of the original resonant transmission line primitive, the well-known conventional transmission line equivalent circuit as well as the equations are not applicable for the unbalanced current in an integrated passive module. For this particular application, a generalized transmission structure theory that applies to both balanced and unbalanced current has to be developed. The impedances of a generalized transmission structure with various loads and interconnections have been studied. An open-circuited load and a short-circuited load lead to series resonance and parallel resonance, respectively. The equations are substantiated with experimental results. Some preliminary study indicates the advantages

of this unbalanced current passives integration technique. Since the existing integrated passive components are no other than some combination of this generalized transmission line primitive, the theoretical analysis may be applied to the further modeling of all integrated passive components.

As the extension of the generalized two-conductor transmission structure model developed for the two-conductor approach, the generalized multi-conductor transmission structure theory has been proposed. As multiple L-C cells are putting in parallel, magnetic and capacitive coupling between cells cannot be neglected. To determine the capacitance between two adjacent conductors on top of the same dielectric substrate, Schwarz-Christoffel transformation and its inverse transformation have been applied with the calculation results verified by measurement. Based on the original voltage and current equations written in matrix form, modal analysis has been conducted to solve the equations. All these provide the basis for any further modeling of an integrated passive structure.

Based on the basic L-C cell structure, this dissertation proposes an alternative multi-cell approach to the integration of reactive components and establishes the principles for its design and operation. It achieves the 3-D integration and has a PCB-mount chip-like structure which may have the potential to be more manufacturable, modularizable and mechanically robust. Different functional equivalents can be obtained by different PCB interconnections. The experimental results confirm the functionality as integrated reactive components for applications such as high frequency resonators.

To apply the multi-conductor generalized transmission structure model to practical integrated passives structures, three typical cases have been studied: spiral-winding structure integrated series resonator, multi-cell structure integrated series resonator and integrated RF EMI filter. All these structures can be treated as one or more multi-conductor transmission structures connected in certain patterns. Different connection patterns only determine the voltage and current boundary conditions with which the equations can be solved. After obtaining the voltages and currents at each point, the impedance or transfer gain of a structure can be obtained. The MATLAB calculation results correlate well with the measurement results. The calculation sensitivities with

respect to variation of various parameters are also discussed and causes of resonance at different frequency range are identified.

The proposed generalized transmission structure model based on matrix modal analysis is rather complex and takes a lot of computer time especially when the number of turns is large. Furthermore, the operating frequency of an integrated resonant module is normally around its 1st resonant frequency and up to the 2nd resonant frequency. Therefore, a more simplistic higher order lumped element model which covers the operating range up to the 2nd resonant frequency may be good enough for the general design purpose. A higher order equivalent circuit model for integrated series resonant modules as an example of integrated power passives is presented in this dissertation. Inter-winding capacitance is also considered compared to the conventional 1st order approximation model. This model has been verified by small-signal test results and can be easily implemented into the design algorithm as part of the high frequency design considerations.

The wide band modeling and proposed new structure mentioned above provide a comprehensive basis for better design of integrated passive components. As a general frequency plane modeling approach, the work presented in this dissertation may be extended to other passive structures, such as multi-layer capacitors, planar magnetics, etc..

Dedication

For as long as space endures,
And for as long as living beings remain,
Until then may I too abide,
To attain the ultimate truth;
Until then may I too abide,
To dispel the misery of the world.

Acknowledgements

Foremost, appreciation goes to my parents, Zijing Zhao and Zhenxiu Tan. It was your encouragement and support that made me to face up to any difficulties and accomplish goals that I had not thought possible. I wish you can share the joy of my achievement and be proud of your son.

My advisor and mentor, Dr. J. D. van Wyk, has directly involved with many aspects of this work. But far more than that, you have exemplified what a real explorer and educator should be. I have been impressed by your brilliancy, diligence, efficiency, and pedagogical excellence for which I will be longing all my life. Your guidance, patience, and selflessness during the development of this work are greatly appreciated. The experience working with you is an enjoyable time period which I will never forget. I have been fortunate to have had the opportunity to work under your supervision.

I also want to express my gratitude to my committee members: Dr. Odendaal, Dr. Alex Q. Huang, Dr. G. Q. Lu, and Dr. Yilu Liu. You have provided, with kindness, your insight and suggestions which are very precious to me, improved my understanding, and broadened my vision.

Specifically, I would like to thank my co-workers Mr. Rengang Chen, Dr. Johan. T. Strydom, Dr. Zhenxian Liang and Dr. Sihua Wen for teaching me use the equipments and precious discussions and comments they have granted me. I am immensely appreciative for your great help. Also I am very grateful to Mr. Dan Huff for helping me do the laser cutting and tremendous technical support;

The people in CPES, Mr. Yuancheng Ren, Mr. Julu Sun, Mr. Ming Xu and Mr. Shuo Wang are gratefully thanked for the assistance you have provided. Your great job and skills help me making my work go smoothly.

I wish to thank all my colleagues and friends in CPES including the staffs and technitians. Thanks for all the help you gave to me during this work.

This work was supported primarily by the ERC Program of the National Science Foundation under Award Number EEC-9731677. This work would not have been possible were it not for their kind support.

Finally, special thanks go to my Buddhist Master Guru Zhi Min Rinpoche. Thanks for your teachings and blessings throughout my life, until the end of samsara.

Lingyin Zhao

May 2004
Blacksburg, Virginia

Table of Contents

Abstract ..... **ii**

Dedication ..... **v**

Acknowledgements ..... **vi**

Table of Contents ..... **vii**

List of Figures ..... **x**

List of Tables ..... **xvi**

Chapter 1: Introduction ..... **- 1 -**
1.1. Background of passives integration ..... - 1 -
1.2. Electromagnetic integration of passives ..... - 2 -
1.2.1. The history of integrated electromagnetic components ..... - 2 -
1.2.2. State-of-the-art integrated passive components ..... - 7 -
1.3. Previous work on modeling of the spiral winding structure integrated passives ..... - 9 -
1.3.1. Lumped Parameter Models ..... - 9 -
1.3.2. Distributed Model or Quasi-distributed Model ..... - 15 -
1.3.3. Loss Model ..... - 17 -
1.3.4. Other Related Modeling Work ..... - 17 -
1.4. Aim of this study ..... - 18 -
1.4.1. Disadvantages of the Previous Modeling ..... - 18 -
1.4.2. Why an Improved Model Needed? ..... - 19 -
1.4.3. Research Work Covered in this Dissertation ..... - 22 -

Chapter 2: Generalized Two-Conductor Transmission Structure ..... **- 23 -**
2.1. Introduction ..... - 23 -
2.2. A Generalized Transmission Structure Model ..... - 26 -
2.3. Impedance Calculations ..... - 29 -
2.3.1. Impedance Z_{AD} with load across BC ..... - 29 -
2.3.2. Impedance Z_{AD} with load across AC ..... - 36 -
2.3.3. Impedance Z_{AC} ..... - 40 -
2.3.4. Impedance Z_{AB} ..... - 41 -
2.4. Current and Voltage Distribution ..... - 42 -
2.5. Cascaded Transmission Line Model ..... - 47 -
2.6. Case Study ..... - 52 -
2.7. Discussion ..... - 56 -
2.8. Conclusion ..... - 60 -

Chapter 3: Multi-conductor Generalized Transmission Structure ..... **- 61 -**
3.1. Introduction ..... - 61 -
3.2. Coplanar Structure Capacitance Calculation ..... - 62 -
3.3. Formulation of Generalized Multi-conductor Transmission Structure ..... - 66 -
3.4. Application of Multi-conductor Transmission Structure to Integrated Passives ..... - 72 -
3.5. Conclusion ..... - 74 -

Chapter 4: Case Study: The Frequency Plane Modeling of the Conventional Spiral Winding Structure Integrated Power Passives ..... **- 75 -**

4.1. Introduction ..... - 75 -
4.2. Modeling of a Conventional Structure Integrated Passives ..... - 75 -
4.3. Case Study ..... - 82 -
4.3.1. A Prototype and The Technical Parameters ..... - 82 -
4.3.2. Parameters Extraction ..... - 83 -
4.3.3. Calculation Results and Small-Signal Measurement Results ..... - 85 -
4.3.4. Large Signal Measurement Results ..... - 87 -
4.4. Discussion ..... - 89 -
4.5. Conclusion ..... - 92 -

Chapter 5: Case Study: The Modeling of an Alternative Multi-cell Structure Integrated Reactive Components ..... - 93 -
5.1. Introduction ..... - 93 -
5.2. Proposed Structure ..... - 94 -
5.3. The First Order Models for Various Interconnections ..... - 95 -
5.4. Design Issues ..... - 98 -
5.4.1. Conductor Design ..... - 98 -
5.4.2. Dielectric Material Selection ..... - 99 -
5.4.3. Magnetic Core Selection ..... - 99 -
5.5. Design Examples and Experimental Results ..... - 100 -
5.5.1. The Design Specifications ..... - 100 -
5.5.2. Technical Aspects of the Prototype ..... - 100 -
5.5.3. Test Results ..... - 101 -
5.6. Generalized Modeling of a Multi-cell Integrated Series Resonator ..... - 106 -
5.7. Case Study ..... - 108 -
5.8. Discussion ..... - 110 -
5.9. Conclusion ..... - 113 -

Chapter 6: Case Study: Electromagnetic Modeling of an Integrated Differential Mode RF EMI Filter ..... - 115 -
6.1. Introduction ..... - 115 -
6.2. Multi-conductor Generalized Transmission Structure Modeling of the Filter ..... - 116 -
6.2.1. The Preliminary Model Based on Multi-conductor Generalized Transmission Structure ..... - 116 -
6.2.2. Improved Model Considering Measurement Issues ..... - 118 -
6.2.3. Loss Modeling ..... - 120 -
6.2.4. Modeling of the Inductive Couplings ..... - 121 -
6.3. Case Study ..... - 123 -
6.3.1. The Prototype ..... - 123 -
6.3.2. Parameters Calculations and Extractions ..... - 124 -
6.3.3. Calculation Results and Measurement Results ..... - 127 -
6.4. Discussion ..... - 128 -
6.5. Proposed New Structure ..... - 132 -
6.6. Conclusion ..... - 135 -

Chapter 7: Simplified Equivalent Circuit Model for Integrated Power Passives ..... - 136 -
7.1. Introduction ..... - 136 -
7.2. Inter-winding Capacitance Calculation ..... - 137 -

7.2.1. Inter-winding Capacitance Calculation -Conventional Spiral Winding Structure - 137 -
7.2.2. Inter-winding Capacitance Calculation - Multi-cell Structure ..... - 139 -
7.3. The Complete Higher Order Impedance Model ..... - 140 -
7.4. Case Study ..... - 142 -
7.4.1. Conventional Spiral Winding Structure ..... - 142 -
7.4.2. Multi-cell Structure ..... - 143 -
7.5. Discussion ..... - 145 -
7.6. Conclusion ..... - 146 -
Chapter 8: Conclusion ..... - 148 -
8.1. Introduction ..... - 148 -
8.2. Generalized Transmission Structures ..... - 148 -
8.3. Case Studies: Frequency Plane Modeling of Integrated Passive Modules ..... - 149 -
8.4. An Improved Lumped Circuit Model for Integrated Passive Modules ..... - 151 -
Bibliography ..... - 152 -
Vita ..... - 155 -

List of Figures

Figure 1-1: Converter integration ..... - 1 -
Figure 1-2: Construction of a classical barrel type integrated series LC structure. ..... - 2 -
Figure 1-3: Self-resonant foil inductor by Kemp [8]. ..... - 2 -
Figure 1-4: Inductor-capacitor hybrid by Reeves [9]. ..... - 3 -
Figure 1-5: Two geometries for integrated series LC components by Stielau [10]. ..... - 4 -
Figure 1-6: Transmission line terminated in a general load ..... - 4 -
Figure 1-7: Series resonant cascaded transmission line primitive ..... - 5 -
Figure 1-8: Parallel resonant cascaded transmission line primitive ..... - 5 -
Figure 1-9: Evolution of a series resonant transmission line primitive to a planar integrated component. ..... - 6 -
Figure 1-10: Toroidal L-C-T transformer structure ..... - 6 -
Figure 1-11: A fully integrated converter with integrated passives. ..... - 7 -
Figure 1-12: Typical structure of a planar integrated L-C module. ..... - 8 -
Figure 1-13: Terminals of the integrated structure and its equivalent circuit. ..... - 8 -
Figure 1-14: Various functional circuits that can be achieved from an integrated L-C. ..... - 8 -
Figure 1-15: Lumped model for an inductor-capacitor hybrid as described by Reeves [9]. ..... - 9 -
Figure 1-16: Currents and voltages within the hybrid. ..... - 11 -
Figure 1-17: Comparison between the impedances derived from Reeves' model and the real case. ..... - 12 -
Figure 1-18: Discrete circuit representations of integrated LC components as described by Murgatroyed [15]. ..... - 12 -
Figure 1-19: Comparison between the typical results derived from Murgatroyed' model and the measurement results. ..... - 13 -
Figure 1-20: Only two possible discrete low frequency equivalent circuits of an integrated series LC component as described by Stielau [16]. ..... - 13 -
Figure 1-21: General transformer model approach for integrated LC. ..... - 14 -
Figure 1-22: Series resonant integrated LC circuit. ..... - 14 -
Figure 1-23: Typical LCT circuit ..... - 14 -
Figure 1-24: Comparison between the typical results derived from Ehsani' model and the measurement results (integrated series resonator). ..... - 15 -
Figure 1-25: Discrete circuit representations of integrated parallel LC components as described by Kemp in [8]. ..... - 16 -
Figure 1-26: Distributed circuit of the integrated LCT transmission line [13]. ..... - 17 -

Figure 1-27: Modeling of a wound LC in [19]. ..... - 17 -
Figure 1-28: Integrated LCT as described by Shoyama [20]. ..... - 18 -
Figure 1-29: Comparison between a typical measured impedance of an integrated series resonator and the ideal impedance; operating region for resonant and non-resonant applications. ..... - 20 -
Figure 1-30: Experimental waveforms of a DPS front-end DC-DC converter with and without integrated LCT [21]. ..... - 21 -
Figure 1-31: Measured transfer gain of an integrated RF-EMI filter [22][23]. ..... - 21 -
Figure 2-1: Classification of typical integrated resonators. ..... - 23 -
Figure 2-2: The most important step in the evolution process of the SR transmission line primitive in [11][7]. ..... - 24 -
Figure 2-3: Spiral winding (a) and multi-cell structure (b), identifying the L-C cell as generalized building block. ..... - 25 -
Figure 2-4: A generalized L-C cell. ..... - 26 -
Figure 2-5: The difference between the current flow of a classical transmission line and a typical L-C cell as encountered in a class of electromagnetically integrated passives [3][4][5]. ..... - 26 -
Figure 2-6: Equivalent circuit of an infinitesimal length Δx of an L-C cell in a generalized transmission structure. ..... - 27 -
Figure 2-7: Equivalent circuit of an infinitesimal length Δx of a generalized transmission structure and a conventional balanced transmission line. ..... - 28 -
Figure 2-8: Current flowing direction for impedance Z_{AD} calculation with load across B and C. ..... - 29 -
Figure 2-9: Impedance Z_{AD} with various resistive loads across B and C. ..... - 31 -
Figure 2-10: Impedance Z_{AD} with various capacitive loads across B and C. ..... - 31 -
Figure 2-11: Impedance Z_{AD} with various inductive loads across B and C. ..... - 31 -
Figure 2-12: Impedance Z_{AD} with various capacitive and inductive loads across B and C. ..... - 32 -
Figure 2-13: An integrated series resonator. ..... - 33 -
Figure 2-14: Z_{AD} with various coupling coefficients k. ..... - 34 -
Figure 2-15: An integrated parallel resonator. ..... - 35 -
Figure 2-16: Typical Z_{AD} with $Z_L=0$. ..... - 36 -
Figure 2-17: Current flowing direction for impedance Z_{AD} calculation with load across B and C. ..... - 36 -
Figure 2-18: Impedance of ZAD with various loads at AC. ..... - 39 -
Figure 2-19: Current flowing direction for impedance Z_{AC} calculation. ..... - 40 -
Figure 2-20: Typical impedance Z_{AC}. ..... - 41 -

Figure 2-21: Current flowing direction for impedance Z_{AB} calculation. - 41 -
Figure 2-22: Typical impedance Z_{AB}. - 42 -
Figure 2-23: Normalized current (magnitude) distributions of the top and bottom conductors at various frequencies. - 45 -
Figure 2-24: Normalized voltage (magnitude) distributions across the top and bottom conductors at various frequencies. - 47 -
Figure 2-25: Spiral winding transmission structure. - 47 -
Figure 2-26: MAXWELL simulation model for the study of mutual inductance. - 48 -
Figure 2-27: Difference between $M_{1,3}$ and $M_{1,4}$ as a function of t, d and w. - 49 -
Figure 2-28: A spiral winding integrated passives module and its equivalent model. - 50 -
Figure 2-29: Cascaded generalized transmission lines. - 50 -
Figure 2-30: Typical impedance characteristics of a series resonator. - 52 -
Figure 2-31: Picture and dimensions of the transmission line prototype. - 53 -
Figure 2-32: Calculation results and measurement results of Z_{AD} without load. - 54 -
Figure 2-33: Calculation results and measurement results of Z_{AC}. - 54 -
Figure 2-34: Calculation results and measurement results of Z_{AB}. - 56 -
Figure 2-35: Typical impedance of an inversely balanced series resonant transmission structure - 56 -
Figure 2-36: Current distributions at low frequency - 57 -
Figure 2-37: The common mode and differential mode currents on the top and bottom conductors. - 58 -
Figure 3-1: Magnetic and capacitive coupling between sections of windings (top view, spiral winding structure) - 61 -
Figure 3-2: Discrepancies between the two-conductor model and the measurement results of an integrated series resonator. - 61 -
Figure 3-3: The cross-sectional view of a building block of an ISRM structure. - 62 -
Figure 3-4: Schwarz-Christoffel transformation. - 63 -
Figure 3-5: Normalized C_{gd} as a function of d, w and t. - 66 -
Figure 3-6: An n-cell integrated passives structure. - 66 -
Figure 3-7: The lossless distributed equivalent circuit of the structure in Figure 3-4. - 67 -
Figure 3-8: Interconnections for series resonator and parallel resonator. - 72 -
Figure 3-9: Typical impedance of the series resonant structure shown in Figure 3-8(a). - 73 -
Figure 3-10: Typical impedance of the series resonant structure shown in Figure 3-8(b). - 73 -
Figure 4-1: 5 sections of a conventional structure integrated passives (top internal view). - 76 -

Figure 4-2: Conductor numbering of a 3-turn structure and its equivalent cascaded multi-conductor transmission structures. - 76 -
Figure 4-3: The pictures of the prototype. - 83 -
Figure 4-4: MAXWELL simulation schematics for different sections. - 84 -
Figure 4-5: Calculation results and measurement results. - 86 -
Figure 4-6: Large-signal measurement setup. - 87 -
Figure 4-7: Comparison between small-signal and large-signal measurement results - 88 -
Figure 4-8: Waveforms of V1 and V2 at various frequencies. - 89 -
Figure 4-9: Changing trends of the impedance when varying parameters. - 91 -
Figure 4-10: Impedance tests across terminal AD and BD. - 92 -
Figure 5-1: Conceptual evolution from an L-C cell to a new planar integrated reactive module - 95 -
Figure 5-2: Proposed structure for integrated reactive components. - 95 -
Figure 5-3: An L-C cell and its lumped equivalent circuit model. - 95 -
Figure 5-4: Various interconnections with their equivalent circuits. - 98 -
Figure 5-5: Definitions of the dimensions. - 99 -
Figure 5-6: Photographs of the prototype. - 101 -
Figure 5-7: PCB for series resonance test. Input terminals AB (see Figure 5-4(a)). - 102 -
Figure 5-8: Impedance analyzer test results for series resonance. - 102 -
Figure 5-9: The topology of test circuit. - 102 -
Figure 5-10: The voltage gain versus frequency characteristics with various load resistance R_L. - 103 -
Figure 5-11: V_{FG} and V_O waveforms at R_L=9.6Ω and f=100kHz. - 104 -
Figure 5-12: PCB for parallel resonance test. Input terminals AB (see Figure 5-4(d)). - 105 -
Figure 5-13: Impedance analyzer test results for parallel resonance. - 105 -
Figure 5-14: PSPICE simulation results and experimental results at R_L=80Ω. - 106 -
Figure 5-15: V_{FG} and V_{AB} waveforms at R_L=9.6Ω and f=150kHz. - 106 -
Figure 5-16: A typical series resonant interconnections. - 107 -
Figure 5-17: interconnections the prototype. - 108 -
Figure 5-18: Calculation and measurement results of the impedance of the prototype - 110 -
Figure 5-19: Sensitivity of impedance to interconnection inductance Lc. - 112 -
Figure 5-20: Sensitivity of impedance to external interconnection inductance L_w. - 113 -
Figure 6-1: Integrated RF-EMI filter for IPEM. - 116 -

Figure 6-2: 4-conductor model of the integrated RF-EMI filter. - 117 -
Figure 6-3: Measurement setup - 119 -
Figure 6-4: The improved model. - 119 -
Figure 6-5: A conductor foil with external magnetic field - 120 -
Figure 6-6: Self and mutual resistance at one conduction path. - 121 -
Figure 6-7: Model improvement with proximity effect taken into account (an infinitesimal length). - 123 -
Figure 6-8: The prototype of an integrated RF EMI filter. - 123 -
Figure 6-9: MAXWELL Q3D model for inductance matrix extraction. - 124 -
Figure 6-10: Inductance of a nickel layer as a function of frequency. - 125 -
Figure 6-11: The ceramic dielectric material permittivity measurement sample and results. - 126 -
Figure 6-12: Measurement results of transfer gain at Z_L=50Ω. - 127 -
Figure 6-13: Calculation results - 127 -
Figure 6-14: Difference made by common-ground measurement setup. - 128 -
Figure 6-15: Calculation results without considering proximity effects. - 129 -
Figure 6-16: Current density distribution inside conductors at 1MHz (Only one edge of a cross section is shown) - 129 -
Figure 6-17: Behavioral model of an integrated RF EMI filter. - 130 -
Figure 6-18: Effect of nickel layer resistance on the filter transfer gain. - 130 -
Figure 6-19: Effect of filter element characteristic impedance on the filter transfer gain. - 131 -
Figure 6-20: Two-conductor transmission structure representation of an integrated RF-EMI filter. - 131 -
Figure 6-21: Approaches to achieve higher attenuation. - 132 -
Figure 6-22: The power losses in each layer versus copper width. - 133 -
Figure 6-23: Proposed higher attenuation filter structure. - 133 -
Figure 6-24. The prototype of an integrated RF EMI filter. - 134 -
Figure 6-25: Measurement results of transfer gain at Z_L=50Ω with the proposed structure... - 135 -
Figure 7-1: Typical impedance of an ISRM - 136 -
Figure 7-2: 1st order approximation lossless model. - 137 -
Figure 7-3: Cascaded transmission line model for a 2-turn conductor winding on one side of the ceramic dielectric substrate - 138 -
Figure 7-4: Multi-turn winding model for conductor on one side. - 139 -
Figure 7-5: Winding top view with distributed parameters: multi-cell structure. - 140 -

Figure 7-6: The complete higher order equivalent circuit of an ISRM. .....- 140 -
Figure 7-7: Simulation results and the small-signal test results. .....- 143 -
Figure 7-8: Pictures of the prototype. .....- 144 -
Figure 7-9: Simulation results and the small-signal test results. .....- 145 -
Figure 7-10: Inter-winding capacitance versus d with various numbers of turns. .....- 145 -
Figure 7-11: Inter-winding capacitance versus core aspect ratio with various N. .....- 146 -

List of Tables

Table 2-1: Technical parameters assumed for the calculation in Figure 2-9 ..... - 32 -
Table 2-2: Technical parameters assumed for the calculation in Figure 2-18 ..... - 39 -
Table 2-3: PARAMETERS OF THE TRANSMISSION STRUCTURE ..... - 43 -
Table 2-4: Technical parameters for the transmission structure prototype ..... - 53 -
Table 3-1: Inter-electrode capacitance calculation examples ..... - 65 -
Table 4-1: Parameters and dimensions ..... - 83 -
Table 5-1: Design specifications for a series resonant module ..... - 100 -
Table 5-2: Technical parameters for the module ..... - 101 -
Table 5-3: Design specifications for a parallel resonant module ..... - 104 -
Table 6-1: Technical parameters of the RF-EMI filter prototype ..... - 124 -
Table 6-2: Technical parameters of the RF-EMI filter prototype ..... - 134 -
Table 7-1: Technical parameters for the module ..... - 144 -

Chapter 1: Introduction

1.1. Background of passives integration

To increase the switching performance and power density, a current trend in converter manufacturing is the integration of semiconductor devices into hybrid modules. The technology for integrating power switching stages has already been well advanced. However, the largest part of converter volume now consists of electromagnetic passives. As a result, the next advance may be passives integration [1] which aims to achieve the following characteristics:

- Functional integration.
- Modularization.
- A reduction in volume, profile and mass.
- Improved manufacturability for mass production.
- Improvement in ruggedness and reliability.

This integration will enable the incorporation of resonant circuits, transformers, EMI filters and the like into the integrated power electronics modules. A fully integrated power converter could be constructed to consist of only a number of integrated active stages and integrated passive stages, as shown in Figure 1-1. Such integration of reactive components in resonant and soft-switching power electronic converters has been reported in the literature [1][2][3][4][5][6].

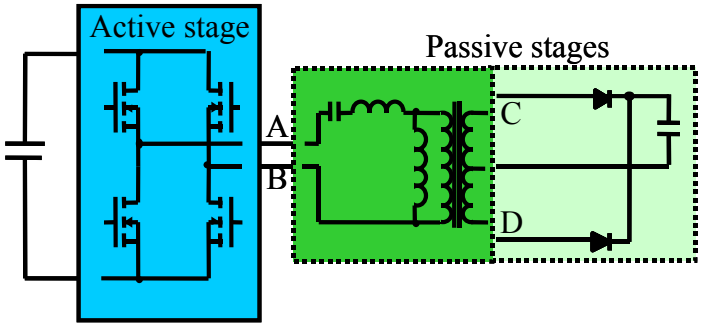

Figure 1-1: Converter integration

1.2. Electromagnetic integration of passives

1.2.1. The history of integrated electromagnetic components

The first integrated LC component, known as a "Wickelkondensator", was made in 1929 [7], and the first patent for such a component was granted in 1949 [7]. This so-called barrel type integrated LC structure normally consists of a multi turn inductor with barrel type windings of bifilar foil conductors with dielectric material placed in between, as shown in Figure 1-2. Parallel or series resonance can be achieved by either providing a conductive path between the two bifilar winding, or by electrically insulating them, respectively.

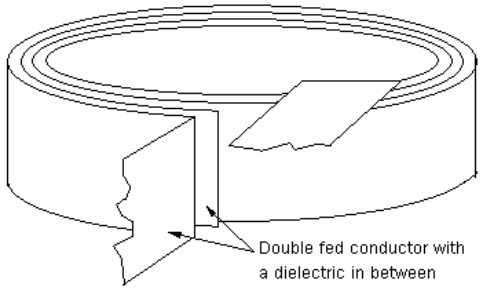

Figure 1-2: Construction of a classical barrel type integrated series LC structure.

Parallel resonant foil inductors have been developed by Kemp [8] in 1975 though the original motivation of this research is to investigate the self-resonance phenomenon in wire coils. These coils are made from a single strip of aluminium foil and a slightly wider strip of plastics foil, wound together on a core of the plastics foil, using a capacitor-winding machine. The method of construction and the principal dimensions are shown in Figure 1-3.

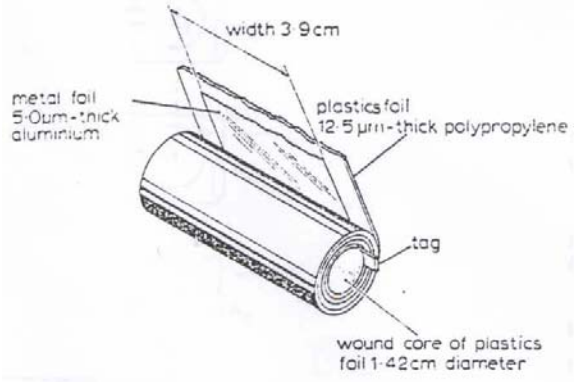

Figure 1-3: Self-resonant foil inductor by Kemp [8].

In 1975, Reeves' research work on so called inductor-capacitor hybrid was published on [9]. The four-terminal inductor-capacitor hybrid component is very similar to the classical barrel integrated LC structure, as shown in Figure 1-4(a). A conventional type of capacitor is wound with a large internal diameter so that it can be fitted over a core of magnetic material, and the plates are connected as in Figure 1-4(b), so that current flows in the same direction in each conductor, thus allowing inductive effects to occur. There are two input terminals and two output terminals, which are connected to a load resistance R. The unit is characterized by the capacitance C between the plates and by its "single-plate inductance" L which can be measured by connecting only one of the plates to a bridge.

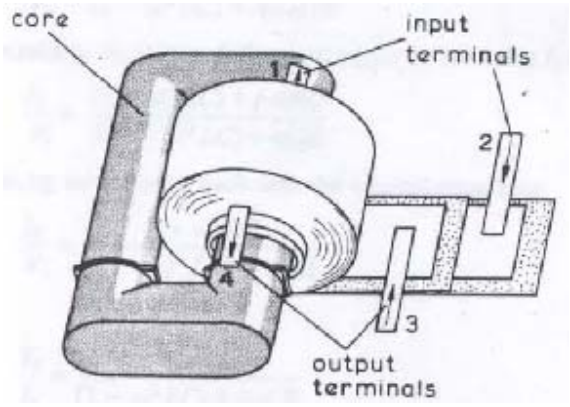

(a) Construction

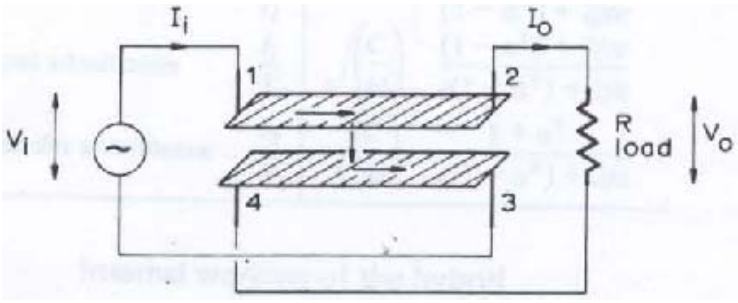

(b) Connections to the hybrid

Figure 1-4: Inductor-capacitor hybrid by Reeves [9].

Two alternative structures for integrated LC components, as shown in Figure 1-5, were made in 1990 by Stielau [10]. They are actually based on the same concept as the classical barrel type LC.

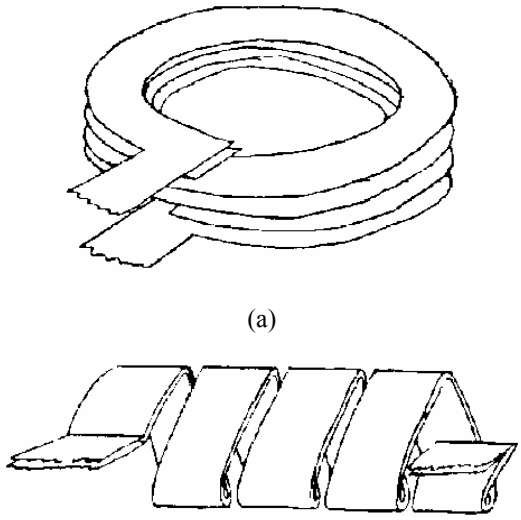

(a)

(b)

Figure 1-5: Two geometries for integrated series LC components by Stielau [10].

Though quarter wavelength transmission line and microstrip filters or resonators have been widely used in microwave technology, transmission line type of integrated power passives were firstly proposed by Smit in [11]. When the length of the transmission line shown in Figure 1-6 is exactly a quarter wavelength ($\lambda/4$) and the load is short-circuited, the input impedance of the structure is infinite, thus resulting in a parallel tuned circuit. If a quarter wavelength transmission line has an open-circuited load, then the input impedance appears to be zero, or a series tuned circuit.

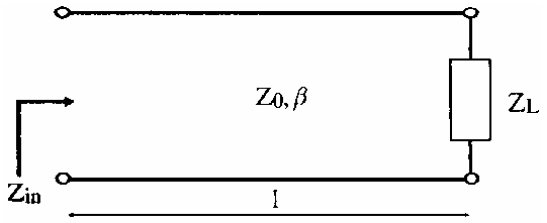

Figure 1-6: Transmission line terminated in a general load

If the same open-circuited or short-circuited quarter wavelength transmission line is used, but the transmission line medium is changed at some discrete point along the length of the line it will now be shown that the resonance can occur at a much lower frequency than that of the initial transmission line. This change of medium results in a change of characteristic impedance, thus resulting in two sections of transmission lines with characteristic impedance Z_{01} and Z_{02}, and length l_1 and l_2, both shorter than a quarter

wavelength. The characteristic impedances can be further changed by altering the physical dimensions of the two sections of transmission lines. Section 1 consists of a short circuited transmission line in ferrite medium (μ_r>>1 and ε_r=1) resulting in a large characteristic impedance, while section 2 consists of an open circuit transmission line (much wider than section 1) in a dielectric medium (μ_r=1 and ε_r>>1) resulting in a very low characteristic impedance. A series resonant cascaded transmission lines and a parallel resonant cascaded transmission lines are shown in Figure 1-7 and Figure 1-8, respectively.

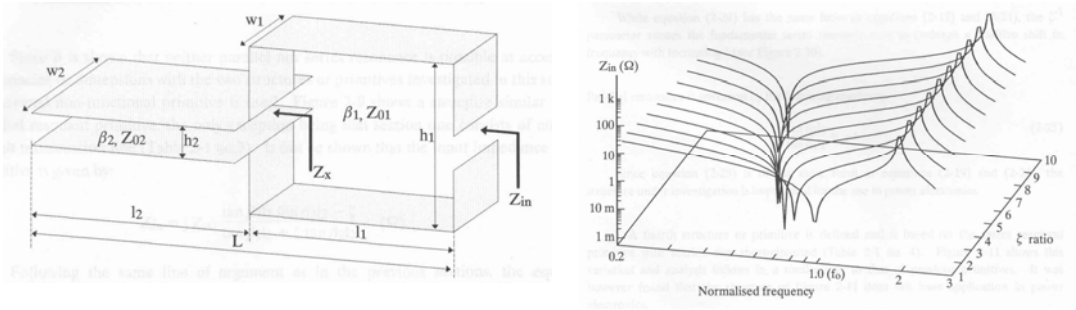

(a) Series resonant cascaded transmission line primitive

(b) Input impedance as a function of frequency and characteristic impedance ratio

Figure 1-7: Series resonant cascaded transmission line primitive

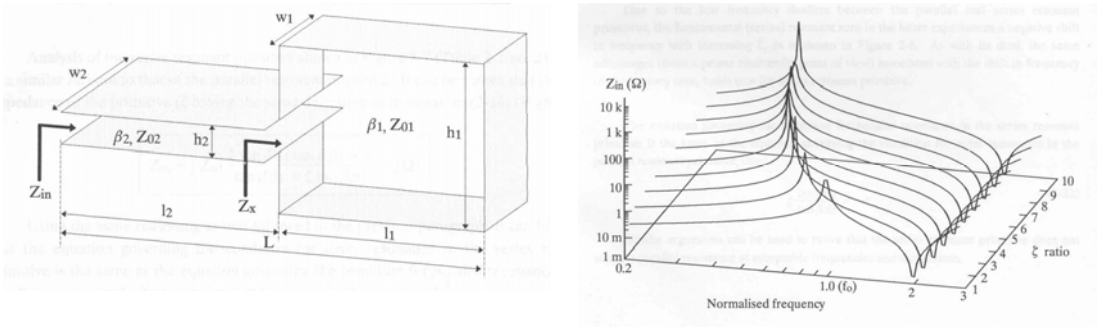

(a) Parallel resonant cascaded transmission line primitive

(b) Input impedance as a function of frequency and characteristic impedance ratio

Figure 1-8: Parallel resonant cascaded transmission line primitive

To realize the series resonant transmission line primitive shown in Figure 1-7, a few evolution steps have been taken [7], as shown in Figure 1-9. It ends up with a planar integrated structure as shown in Figure 1-9(f). It is actually the theoretical basis of the planar spiral-winding structure integrated passives that has been implemented in some practical power converters [2][6][12].

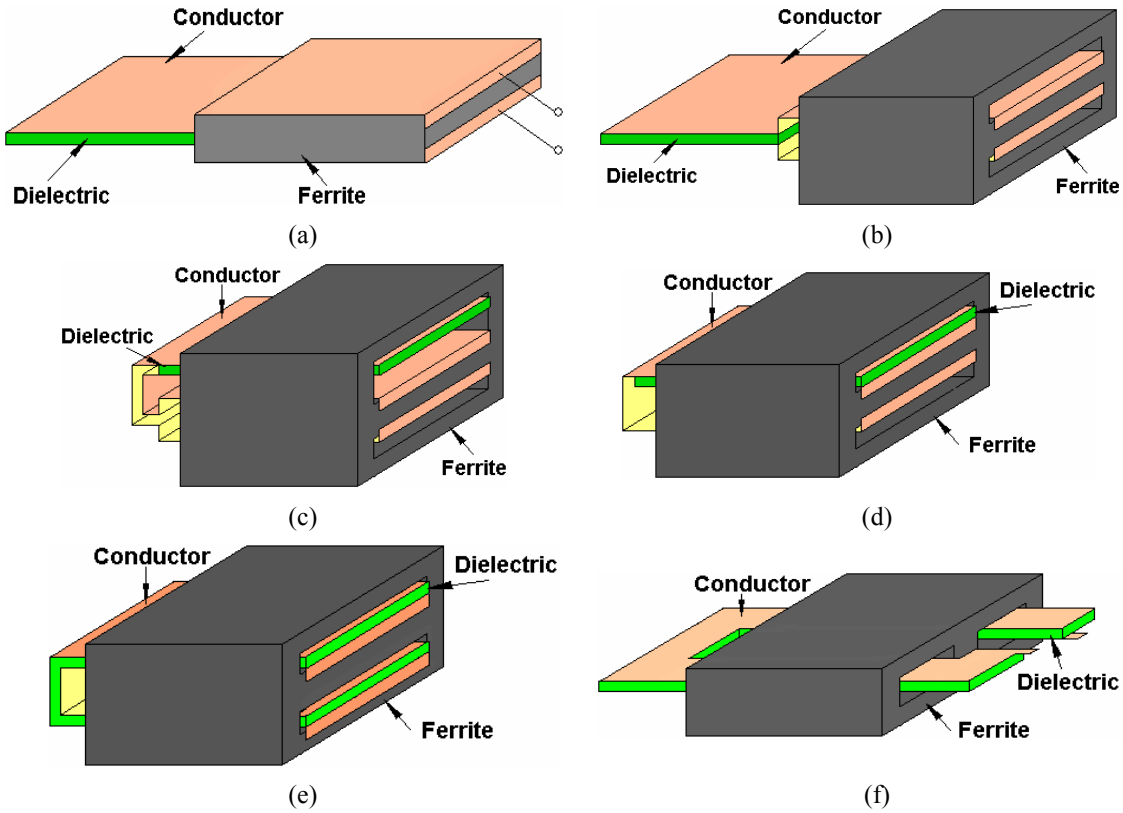

Figure 1-9: Evolution of a series resonant transmission line primitive to a planar integrated component.

L-C-T integration was first introduced by Ferreira and Smit, and the technology was successfully demonstrated in a high frequency series resonant converter [13]. The configuration is illustrated in Figure 1-10. The primary consists of bifilar foil windings, separated by a suitable dielectric, wound directly on the core. The single-turn secondary forms a shell which contains the core and the primary. The space between the primary winding and the internal walls determines the leakage or series inductance.

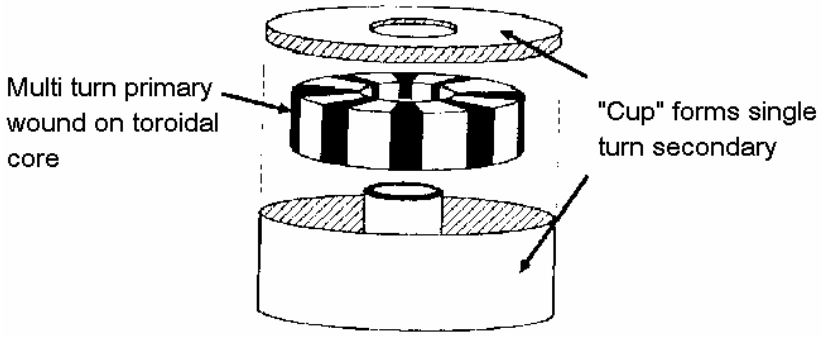

Figure 1-10: Toroidal L-C-T transformer structure

1.2.2. State-of-the-art integrated passive components

As mentioned in 1.2.1, today's spiral-winding structure integrated passives basically follows the structure shown in Figure 1-9(f). These integrated electromagnetic power passives have been realized in terms of distributed structures, utilizing magnetic layers, conductive layers and dielectric layers [4][12][14]. The magnetic layers were ferrite based, the conductive layers were initially in terms of winding spirals and the dielectric layers used high permittivity (normally $100<\varepsilon_r<10000$) dielectric ceramics with frequencies of operation stretching from some 10kHz to 1MHz. A typical converter structure to be integrated is shown in Figure 1-11(a), with an exploded view of such a distributed, integrated structure for the electromagnetic power passives shown in Figure 1-11(b).

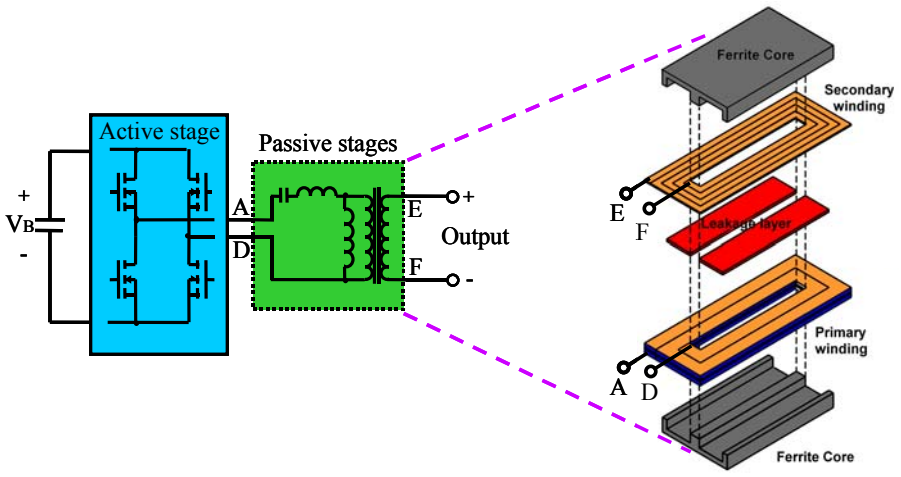

(a) An integrated converter structure

(b) Exploded view of the integrated passive stage shown in the middle block of (a)

Figure 1-11: A fully integrated converter with integrated passives.

To illustrate the versatility of the integrated LCT, let us focus on a simple integrated L-C module, which is shown in Figure 1-12. As an alternative to a discrete inductor and capacitor L-C circuit, the planar integrated L-C module has been demonstrated to be a viable and promising option for power electronic applications [5][6][14]. An integrated L-C module is based on planar ferrites and high permittivity ceramic type dielectrics which has spiral conductor windings metalized on its both sides, as shown in Figure 1-12.

The terminals of the structure are labeled as in Figure 1-13(a) and the corresponding distributed model of the unfolded structure is shown in Figure 1-13(b).

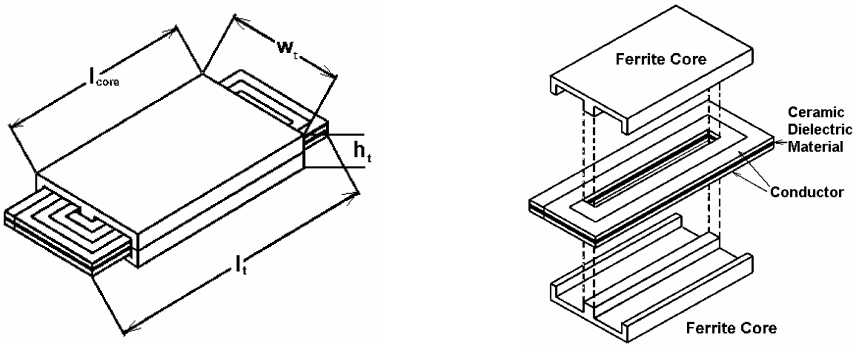

(a) Overview (b) Exploded view

Figure 1-12: Typical structure of a planar integrated L-C module.

(a) Spiral winding structure with its terminals labeled (b) Equivalent circuit

Figure 1-13: Terminals of the integrated structure and its equivalent circuit.

This basic structure can be used in at least three different ways, by choosing the various sets of connections. A parallel resonator is realized if it is connected as in Figure 1-14(a). A series resonator is achieved if terminals A-D or B-C are chosen, as shown in Figure 1-14(b). The same structure can also be used as a low pass LC filter if an input is applied between A and D and the output is taken from C-D, as shown in Figure 1-14(c).

(a) Parallel resonant (b) Series resonant (c) Low-pass filter

Figure 1-14: Various functional circuits that can be achieved from an integrated L-C.

1.3. Previous work on modeling of the spiral winding structure integrated passives

Many different methods for modeling these integrated resonator structures have been proposed. These include lumped models by Reeves [9], P.N. Murgatroyed [15], Stielau [16], and M. Ehsani [17], distributed model by Kemp [8] and J. Smit [13], and loss model by J. T. Strydom [18]. Besides all these, basic modeling and identifications of the parasitics in some integrated electromagnetic components for power electronic applications have been reported in [19][20].

1.3.1. Lumped Parameter Models

The first order approximation model is simply an inductor and a capacitor in some form of combination, normally series resonator, parallel resonator or low-pass filter, depending on the interconnections [5][17][24]. Apparently, this first order approximation is far from enough especially when high frequency characteristics are concerned because the impedances of these structures normally tend to have many higher order poles and zeros apart from the fundamental resonant frequency. Thus, some higher order lumped parameter models have been proposed such as the model by Reeves [9], the model by Murgatroyed [15], the model by Stielau [16] and Ehsani [17].

Reeves' model is shown in Figure 1-15. The inductor-capacitor hybrid structure shown in Figure 1-4 is modeled as two coupled inductors with two capacitors in between. As a general model, a load Z_L is added across terminal B and C. The impedance Z_{AD} varies with load impedance. For instance, series resonator and parallel resonator can be achieved by making the load open-circuited or short-circuited.

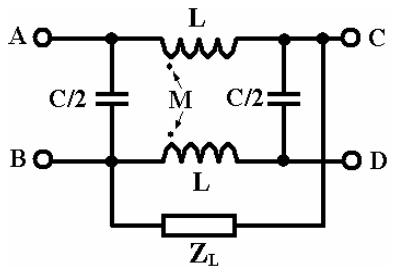

Figure 1-15: Lumped model for an inductor-capacitor hybrid as described by Reeves [9].

The impedance across terminal A and D is given by

$$Z_{AD}(s) = \frac{s(L+M)(\frac{4}{sC} + Z_L) + \frac{2Z_L}{sC}}{s(L+M) + \frac{2}{sC} + 2Z_L} \tag{1-1}$$

The voltage and current distribution diagram with short-circuited and open-circuited load are shown in Figure 1-16(a) and (b), respectively. The two conductors are represented by parallel lines, with black dots marking the input and open circles the output terminals. Arrows show the current, their size giving an indication of magnitude. Although the gain and impedance calculations are based on the lumped model shown in Figure 1-15, the voltage and current distribution diagrams actually took some transmission structure effects into account, more or less.

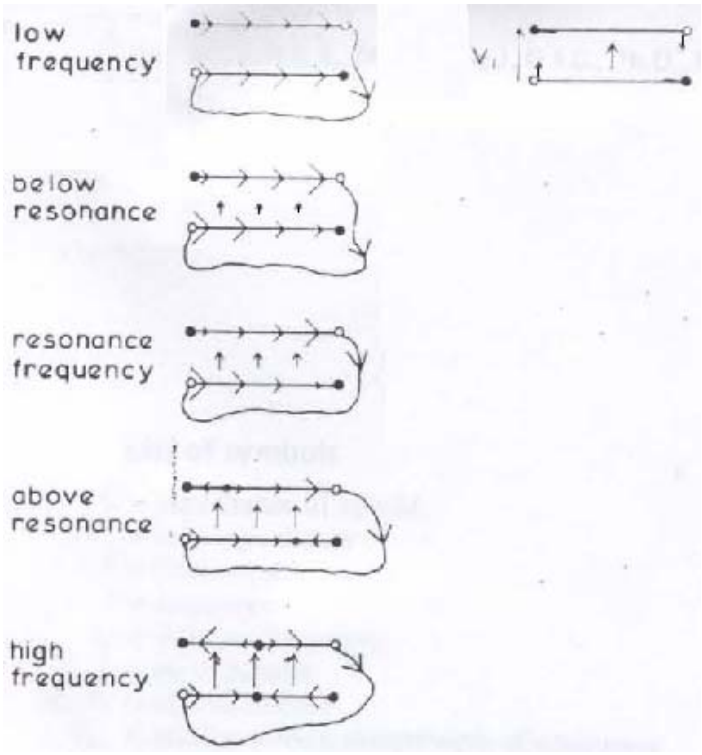

(a) Short-circuited output

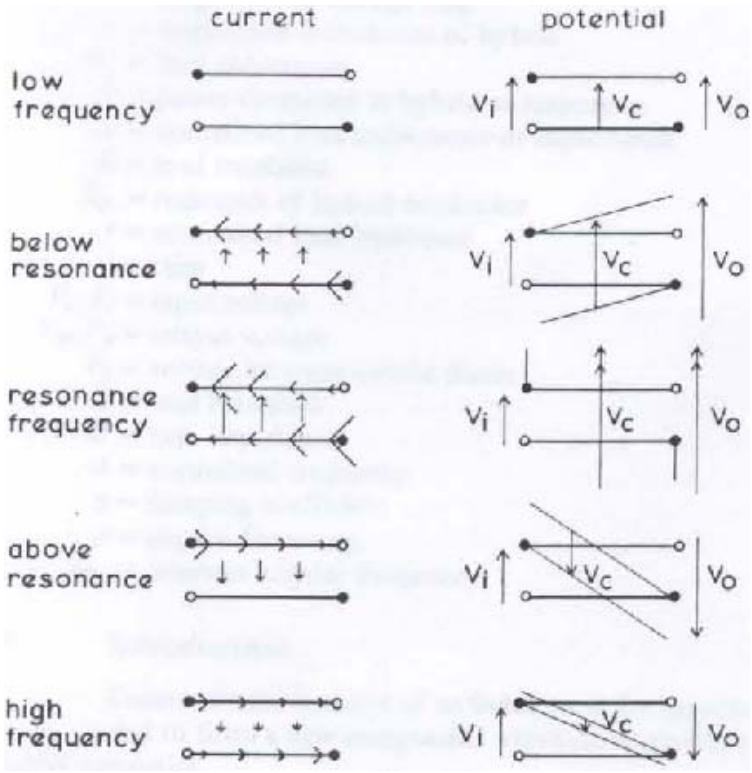

(b) Open-circuited output

Figure 1-16: Currents and voltages within the hybrid.

However, this lumped model can not predict the high frequency resonances present on the impedance curve. Figure 1-17 compares the impedances of a real case and that developed by Reeves' model which demonstrates significant differences at high frequencies.

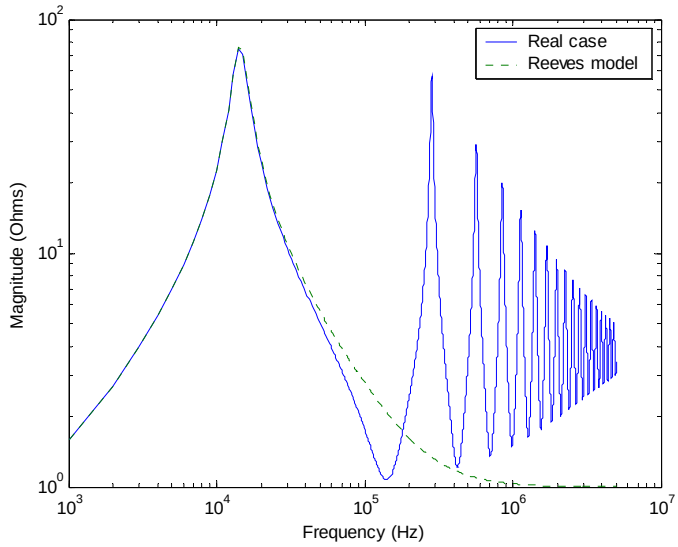

(a) Z_L=1MΩ

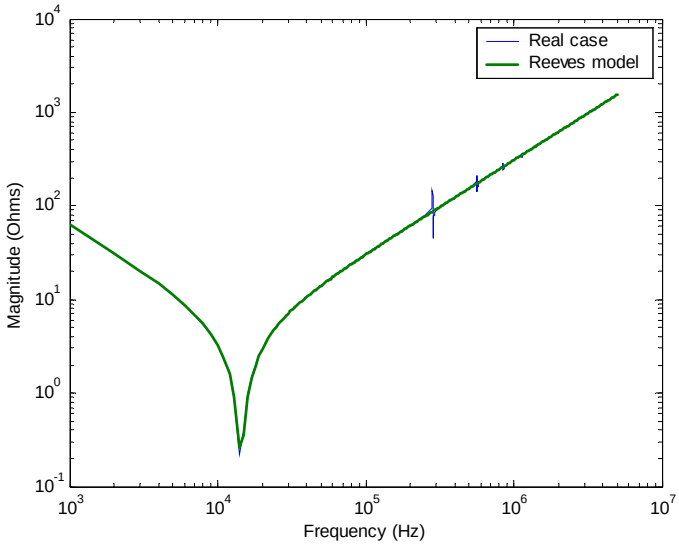

(b) Z_L=1Ω

Figure 1-17: Comparison between the impedances derived from Reeves' model and the real case.

Murgatroyed's alternative model for an inductor-capacitor hybrid proposed by Reeves [9] is depicted in Figure 1-18. Each metal foil is notionally divided into two parts connected in series, each half having inductance L and resistance R in series. The capacitance of the hybrid is represented, in this simplest of models, by a single capacitance C connected between the midpoints of the foils. This model can only predict the fundamental resonance and demonstrates a very significant discrepancy at higher frequency range, as shown in Figure 1-19.

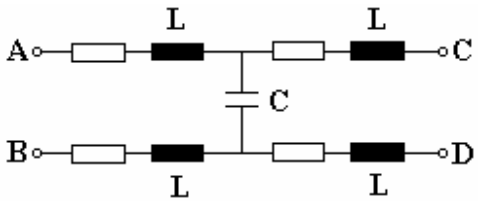

Figure 1-18: Discrete circuit representations of integrated LC components as described by Murgatroyed [15].

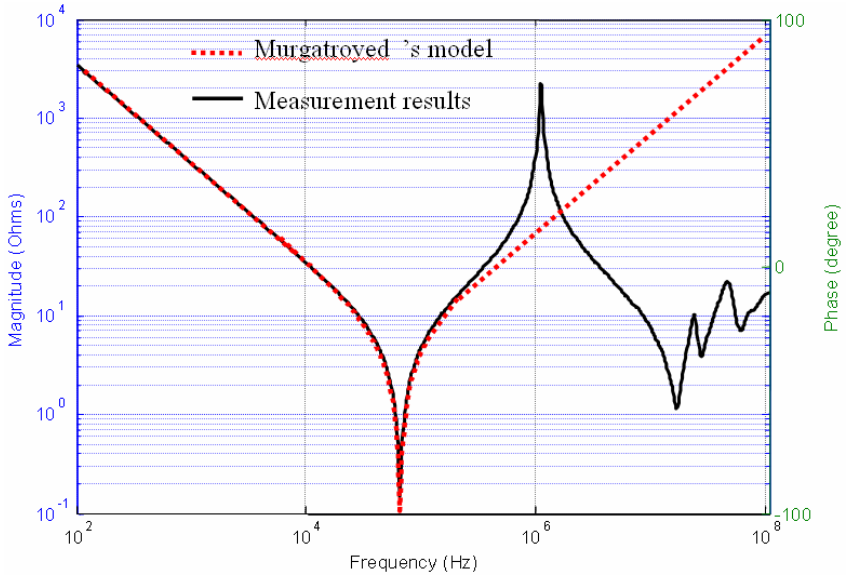

Figure 1-19: Comparison between the typical results derived from Murgatroyed' model and the measurement results.

Stielau [16] did an in-depth analysis of integrated LC components, based on circuit point of view. One of the important contributions that he had made to this technology, is to prove that there are only two possible discrtete equivalent circuit representations of an integrated series LC component, at low frequencies. These were derived from an expression for the input impedance of a component, and is shown in Figure 1-20.

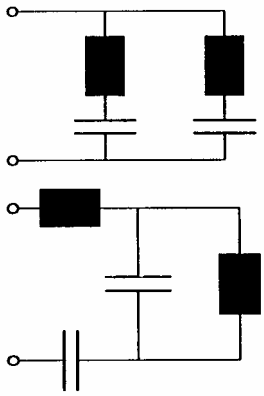

Figure 1-20: Only two possible discrete low frequency equivalent circuits of an integrated series LC component as described by Stielau [16].

An integrated LC can be modeled by a transformer-based structure, as shown in reference [17]. The two conductors of the LC can be viewed as the primary and secondary windings of a classical transformer, as shown in Figure 1-21. The general LC model of Figure 1-21 can be reduced to a series LC model by considering terminals 1 and

4 only. The resulting specific model is shown in Figure 1-22. Similarly, the model for an integrated LCT will have an additional third winding, as shown in Figure 1-23.

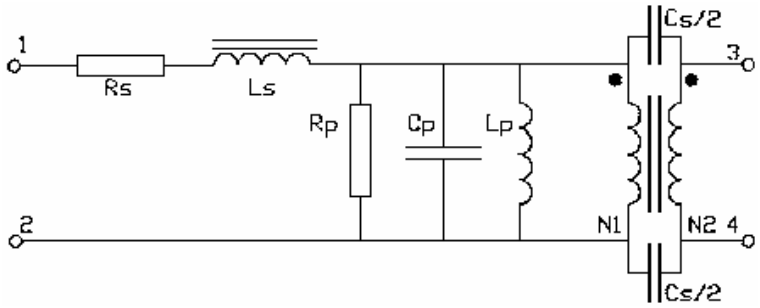

Figure 1-21: General transformer model approach for integrated LC.

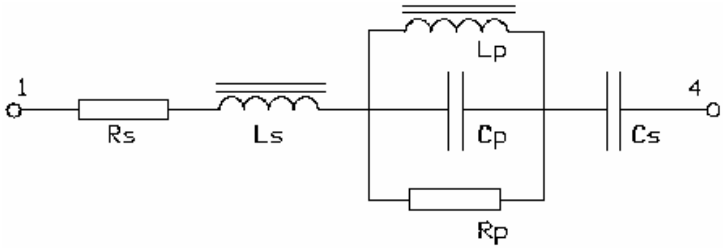

Figure 1-22: Series resonant integrated LC circuit.

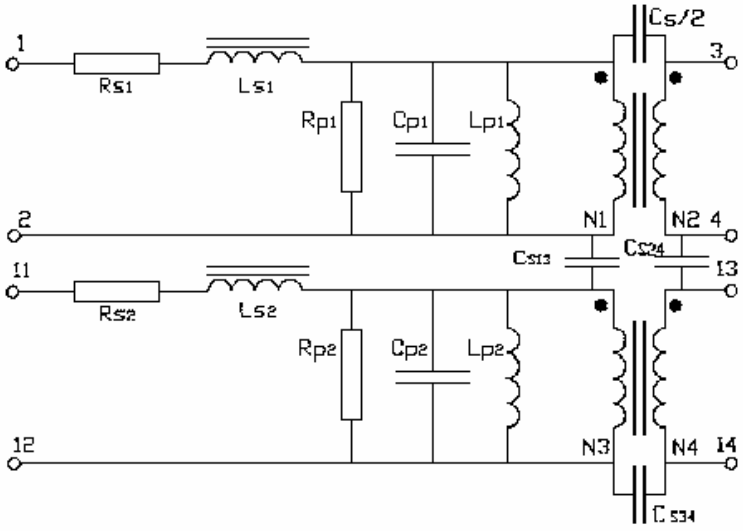

Figure 1-23: Typical LCT circuit

Ehsani's model, especially the one shown in Figure 1-22, is actually the same as Stielau's model, ignoring the resistances representing the losses. Their model may have a rather good prediction up to the third resonant frequency, from the circuit theory point of view. However, it is not able to model the resonances at higher frequencies, as shown in Figure 1-24. On the other hand, the calculation of some of the parameters in their model seems questionable. For instance, the parallel capacitance C_p "estimate is derived from

the fact that at high frequencies each of the wound plates will behave as (2N-1) single turn capacitors in series" [17].

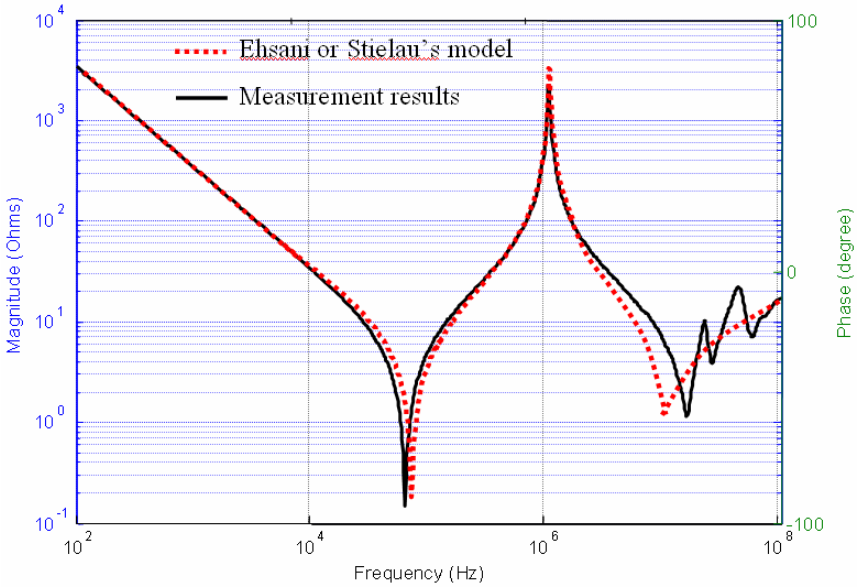

Figure 1-24: Comparison between the typical results derived from Ehsani' model and the measurement results (integrated series resonator).

1.3.2. Distributed Model or Quasi-distributed Model

Kemp's model for a parallel LC component shown in Figure 1-3 is illustrated in Figure 1-25. The coil is divided into S subsections, within which phase shifts are deemed negligible. The u^{th} subsection is then considered to have a self inductance L_u, a self capacitance C_u, a resistance R_u, and a mutual inductance M_{uv} with the v^{th} subsection. The self inductances L_u are estimated by assuming that the current is uniform across the width of the foil and that $L_u=n_u^2 l_u$ where l_u is the self inductance of a single turn at the centre of the subsection which has n_u turns. A similar procedure gives the mutual inductances. The capacitances C_u are found by treating each turn and its neighbour as a parallel plate capacitor and the mid-section value is c_u, thus $C_u=c_u/N_u$.

This is a so-called quasi-distributed model in the sense that it consists of a number of LC elements thus may predict the higher order resonances. However, one of the most critical issues with this model still remains unsolved: the determination of S, the number of subsections. Preliminary calculation found out that the higher order resonant

frequencies vary with S. In another word, one could “fit” the curve well by tuning the number of subsections without a deep insight into the physical meanings.

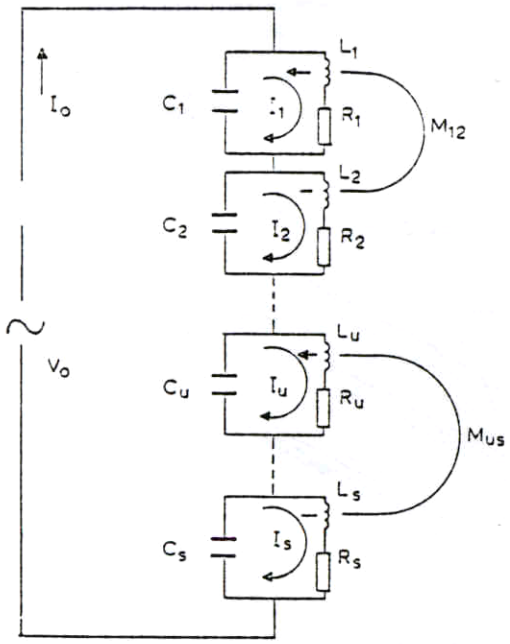

Figure 1-25: Discrete circuit representations of integrated parallel LC components as described by Kemp in [8].

Reference [13] introduced by Ferreira, Van Wyk and Smit showed a distributed model of the LCT, which is based on microstrip technology. It consists of a number of cells, each with resistive, inductive and capacitive components, as shown in Figure 1-26. “It is however necessary that the new structure behaves in the same manner as the transmission line structure, because the experimental and theoretical work conducted within the scope of this project, indicated that the distributed network is a workable alternative to the lump ed L-C-T” [13]. However, the reference does not go to the details of the calculation and the parameter determination. Neither did it show the calculation results with distributed model compared with the measurement results.

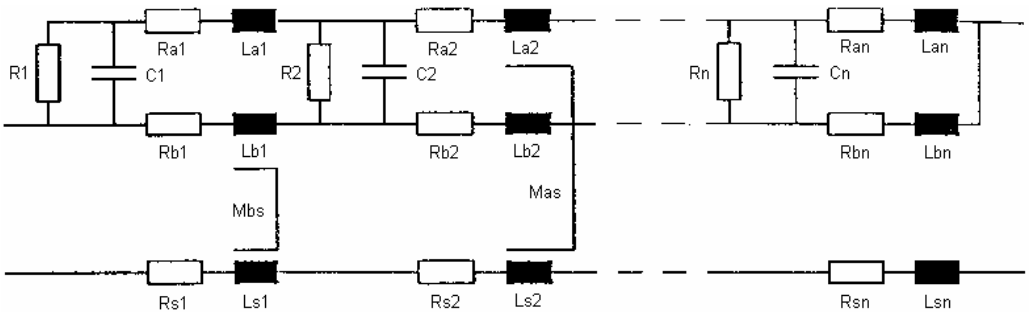

Figure 1-26: Distributed circuit of the integrated LCT transmission line [13].

1.3.3. Loss Model

A loss model for the planar integrated L-L-C-T is presented in [18]. The loss model takes non-sinusoidal core excitation losses, both skin and proximity effect conductor losses and dielectric losses into account. The linear current distribution assumes that the winding length is much shorter than a wavelength in the operating frequency range, and that the resistive voltage drop is negligible compared to the excitation voltage.

1.3.4. Other Related Modeling Work

Figure 1-27 shows the modeling of a wound LC proposed by S. J. Marais and J. A. Ferreira [19]. The concept of the ideal electromagnetic material is introduced as a means to investigate the formation of high frequency parasitics effects, and to act as an intermediate step to generate an equivalent circuit model. The influences of the inter-winding capacitance on the practical multi-turn bifilar capacitance winding have been discussed.

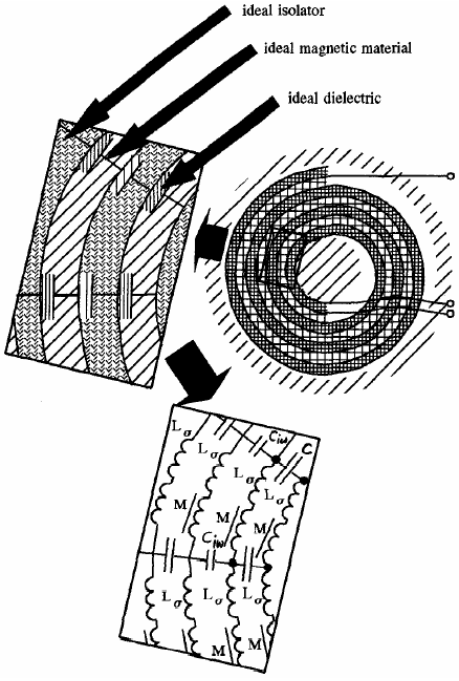

Figure 1-27: Modeling of a wound LC in [19].

An integrated multi-layer transformer by Shoyama [20] used in a resonant buck-boost converter is illustrated in Figure 1-28(a). It utilizes the winding capacitance as part of the resonant tank without making the operation complex. Figure 1-28(b) shows its lumped equivalent circuit model with the measured values of all the parameters given in [20].

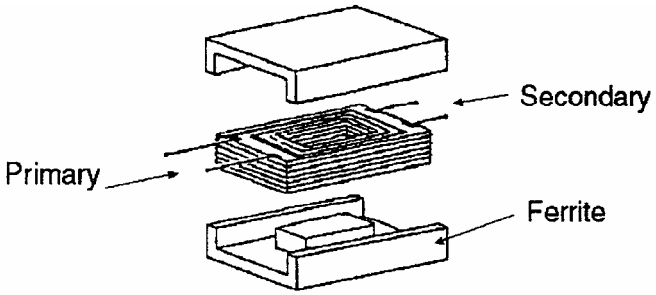

(a) Physical structure

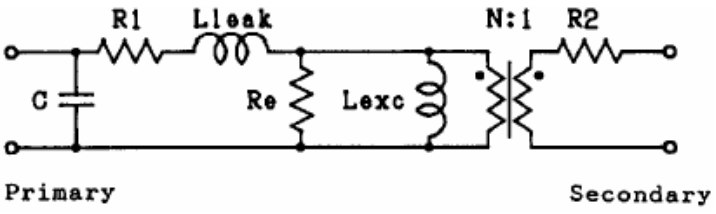

(b) Equivalent circuit

Figure 1-28: Integrated LCT as described by Shoyama [20].

1.4. Aim of this study

1.4.1. Disadvantages of the Previous Modeling

From the previous sections, it can be seen that there are numerous methods for the modeling of integrated passive components. Loss modeling is not the major focus of this research and will not be covered in this dissertation. The other electromagnetic models may be sufficient for general design purpose and correlate the low frequency characteristics well. However, some of the disadvantages of these lumped parameter modeling including the parasitics investigations in [19][20] are:

1) The modeling is only accurate for a limited frequency range. The higher order resonances are totally neglected.
2) No convincing identification of the causes of the high frequency resonance.

3) None of the previous models show the details on how to structure-orientedly calculate the parasitics such as the inter-winding capacitance.
4) The models are not necessarily related to the physical structure of the system, but merely tries to emulate measurements on the system.
5) By changing the terminal connections, the L-C structure can change to a different electromagnetic functionality. The structure stays the same, but must now be modeled with a completely different circuit.

The disadvantages of the distributed modeling technique presented in [13] are:

1) This model is trying to model the two primary conductor windings and one secondary winding as three separate conductor sections with magnetic and capacitive coupling between each other. Each conductor has been unwound into a straight line and can be divided into many resistive and inductive cells. Cells at the same position along the line are coupled with each other. However, considering a multi-turn LCT, each cell may not only be magnetically coupled with the cells of other two conductors but also have magnetic coupling with some other cells of the same conductor.
2) Similarly, this model also ignores the capacitive coupling between cells of the same conductor in a multi-turn structure.
3) This model shows neither the causes of the high frequency resonance nor how to calculate those accurately.
4) Difficult to assess the number of cells needed to model the structure sufficiently.
5) A complex model results, making analysis and simulation difficult.

1.4.2. Why an Improved Model Needed?

The typical impedance of an integrated series resonator is shown in the solid curve of Figure 1-29. Obviously, it has a lot of high frequency resonances and is significantly different from the ideal impedance shown in the dashed curve.

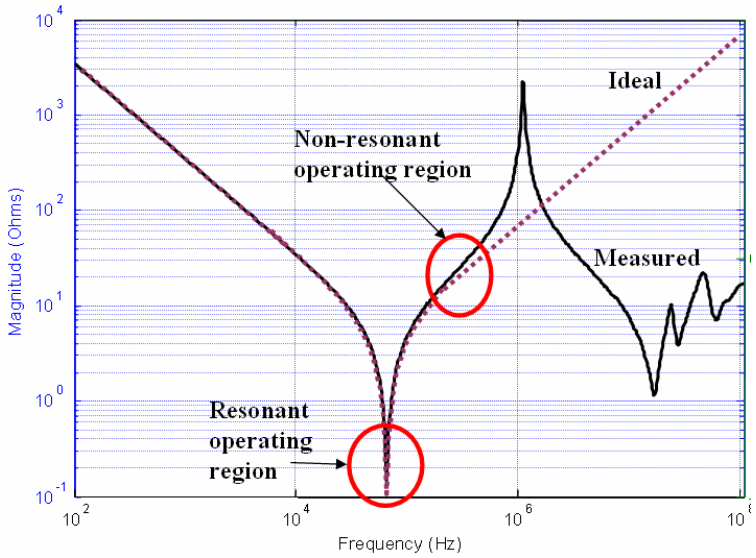

Figure 1-29: Comparison between a typical measured impedance of an integrated series resonator and the ideal impedance; operating region for resonant and non-resonant applications.

During the design process of an integrated passive component, it is necessary to consider the high frequency characteristics because:

1) For some applications, especially the non-resonant applications, the operating frequency may be located at or close to where the parasitic resonances occur if it is not designed carefully. The operating regions for resonant and non-resonant applications are marked in Figure 1-29.

2) The high frequency resonances may result in negative EMI effects such as severe ringing on voltage and current waveforms even if the operating frequency is not very close to them. As a matter of fact, the compact size of integrated passives and the high μ, high ε materials normally used raise the probability of enhanced magnetic and capacitive coupling among elements inside a module. Thus, the EMI problems may become more severe and the parasitic resonances may shift to even lower frequencies than those of discrete passive components. As an example, the test waveforms of a DPS front-end DC-DC converter with discrete components and integrated LCT [21] are compared in Figure 1-30. With the other part of the circuit kept the same or very similar, the integrated LCT actually introduced higher parasitics that lead to heavier ringing.

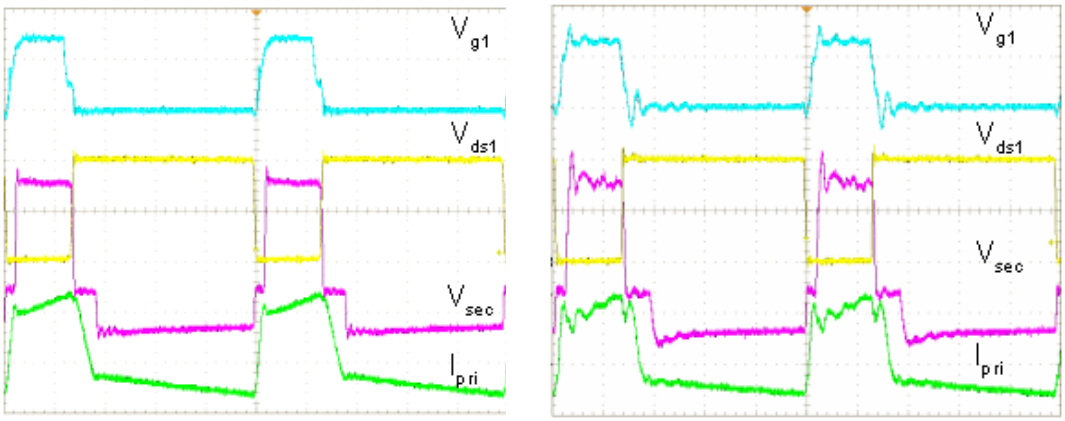

(a) Baseline converter with discrete components.

(b) Converter with integrated LCT

Figure 1-30: Experimental waveforms of a DPS front-end DC-DC converter with and without integrated LCT [21].

3) For integrated EMI filter design, accurate modeling and analysis of the high frequency characteristics become extremely important since the major goal of an EMI filter is to achieve as high as possible high frequency attenuation. The measured transfer gain of an integrated RF-EMI filter [22][23] is shown in Figure 1-31. Without a good model that covers all over the frequency range, an optimized design is hard to achieve.

However, none of the existing model could achieve a real wide-band model that predicts the component behavior at both low frequencies and high frequencies. Therefore, an improved frequency-plane wide-band model is going to be developed in this research.

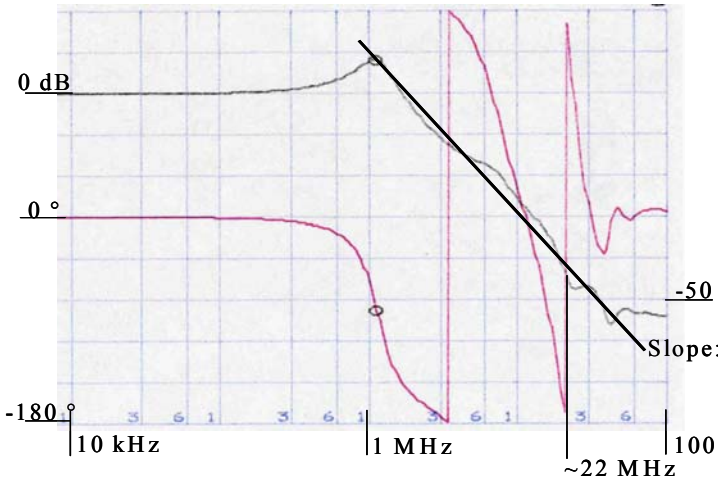

Figure 1-31: Measured transfer gain of an integrated RF-EMI filter [22][23].

1.4.3. Research Work Covered in this Dissertation

In this dissertation, a few structures of integrated passive components are investigated. This investigation considers the electromagnetic modeling of the planar integrated power resonators with the aim of developing accurate transmission structure based modeling process. The following aspects will be included in this dissertation:

1) Identify the limitations of the previous modeling work on integrated passives.
2) Investigate the essential natures of integrated passives by modeling the basic building block.
3) Identify the causes of the high frequency resonance and model the integrated passives structures with a detailed higher order calculation based on generalized transmission structure theory.
4) Develop systematic rules and formulas to facilitate the design process from a parasitics point of view.
5) Investigate alternative structures for integrated passive components.

Chapter 2: Generalized Two-Conductor Transmission Structure

2.1. Introduction

The part of the structure giving it the unique characteristics, is the parallel plate metallized ceramic, so this will be considered as in Figure 2-1(a), with its general schematic shown in Figure 2-1(b). With different interconnections, it has been practically found that the structure shows different characteristics, as shown in Figure 2-1(c)-(f). For instance, an integrated series resonator and parallel resonator can be achieved by the interconnections shown in Figure 2-1(c) and (e), respectively. Both these structures can be modeled well by classical transmission lines. However, previous modeling in terms of transmission line structures [11] and planar layers[25] only offered a partial explanation of the frequency plane behavior of the structures shown in Figure 2-1(d) and (f). In particular, practical experience has shown that a structure such as Figure 2-1(d) will have – for the same dimensions as that of a structure connected as in Figure 2-1(c) – a much lower series resonant frequency [14].

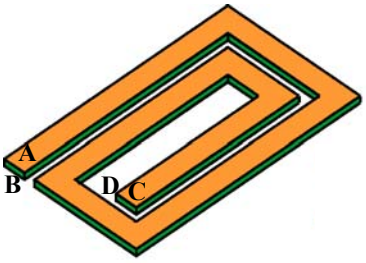

(a) A simplified integrated passives structure

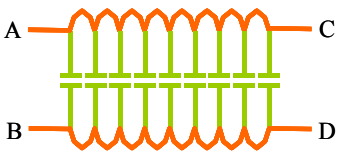

(b) A general model of (a)

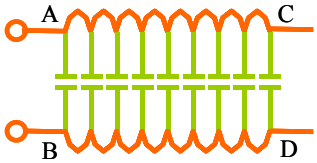

(c) Series resonance (open quarter wave transmission line)

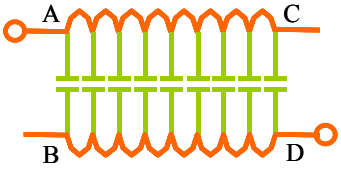

(d) Series resonance (used for integrated resonators in power electronics)

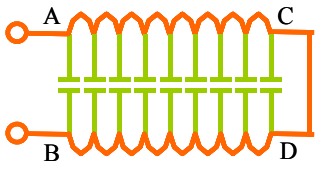

(e) Parallel resonance (short-circuit quarter wave transmission line)

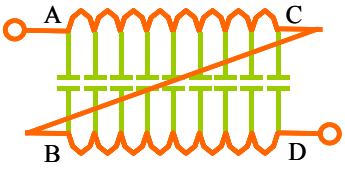

(f) Parallel resonance (used for integrated resonators in power electronics)

Figure 2-1: Classification of typical integrated resonators.

The practical spiral winding structures of the integrated passives were obtained from an evolution process of a classical resonant transmission line primitive proposed by Smit [11][7]. In this evolution process, one of the key steps is illustrated in Figure 2-2(a)-(b). And the corresponding cross-sectional views of the current distributions are given in Figure 2-2(c)-(d).

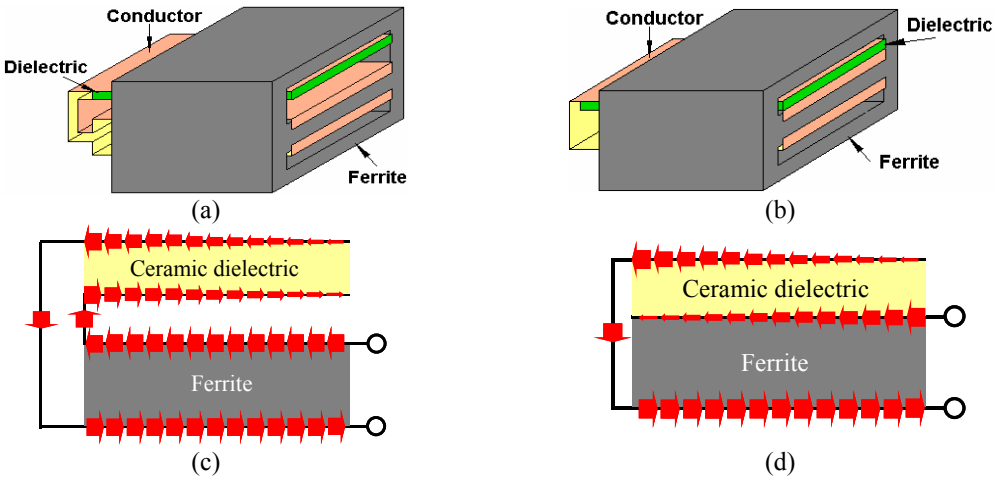

Figure 2-2: The most important step in the evolution process of the SR transmission line primitive in [11][7].

As we know, the usual form of the partial differential equations used for modeling classical transmission lines and satisfied by the voltage and current are valid only when the current in the two conductors are balanced. The transmission line is said to be balanced when the current in the two conductors are equal in magnitude but are opposite in direction. If unbalanced, the conventional equivalent circuits, and therefore, the voltage and current equations are not valid any longer [26]. From Figure 2-2, the current distribution in (c) and (d) are obviously different after this transformation. The current in the two conductors flow in direction and have a different magnitude at each infinitesimal length. Therefore, this transformation is unequal in principle and the modeling based on the conventional transmission line theory may not have convincing theoretic basis.

In order to model the practical integrated passives structure, the basic building block of the structures needs to be studied in the first place. Figure 2-3 demonstrates a few practical structures for integrated passives, in which Figure 2-3(c) is an alternative to the spiral winding integrated structures [27] (see Chapter 5). In all these practical structures, an L-C cell [27] can be identified as a basic building element for an integrated L-C module, as shown in Figure 2-3(a) to (c), and defined in (a). It is actually a dielectric

substrate with both sides metallized, with or without being enclosed in a magnetic core. It can be modeled as a distributed parameter system with four terminals A, B, C, D, as shown in Figure 2-4(b). This generalized L-C cell can provide a sound basis for the further modeling of integrated passives structures, as well as point the way to new innovations in this field, as will be discussed subsequently.

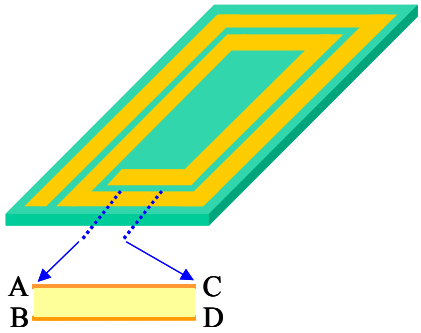

(a) Spiral winding

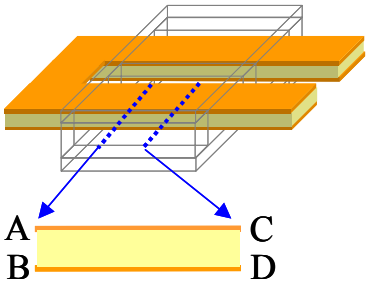

(b) Spiral winding in a core

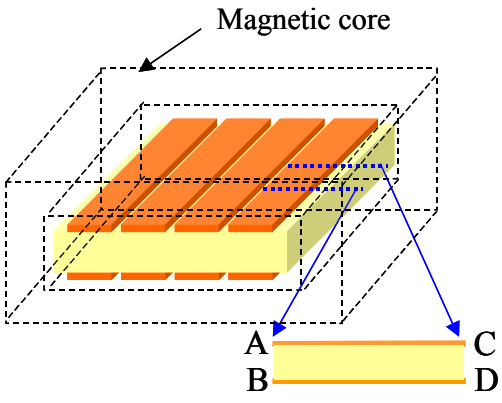

(c) Multi-cell structure

Figure 2-3: Spiral winding (a) and multi-cell structure (b), identifying the L-C cell as generalized building block.

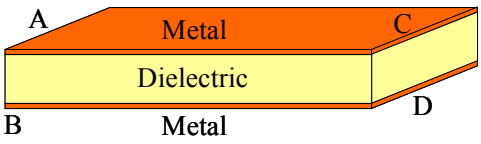

(a) Physical structure

(b) Equivalent two-port network

Figure 2-4: A generalized L-C cell.

The impedance between A and B can be calculated by classical transmission line equations. However, these equations do not apply to the modeling of the generalized L-C cell with arbitrary current distribution in conductors AC and BD for the reasons just discussed. The current magnitude and direction of a classical transmission line and that of a typical integrated L-C cell as encountered in a family of the integrated passives that have been practically applied [3][4][5] are compared in Figure 2-5. Therefore, in the following a generalized transmission structure model is proposed.

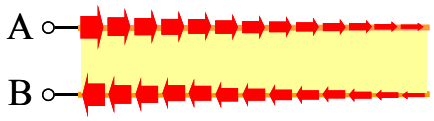

(a) Current flow from A to B (a classical transmission line)

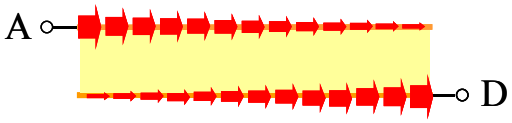

(b) Current flow from A to D (a typical generalized transmission structure used in integrated passives with anti-symmetrical current in two conductors)

Figure 2-5: The difference between the current flow of a classical transmission line and a typical L-C cell as encountered in a class of electromagnetically integrated passives [3][4][5].

2.2. A Generalized Transmission Structure Model

For a structure as in Figure 2-4, a generalized equivalent circuit for an infinitesimal length Δx is given in Figure 2-6. The two conductors have magnetic and capacitive coupling and the losses of the structure are represented by resistances and conductances. The most important assumption is that the currents in the two conductors are not

necessarily balanced. They can have any magnitude, flowing in either direction. The conventional transmission line is just a special case when $I_1(x,t)=-I_2(x,t)$.

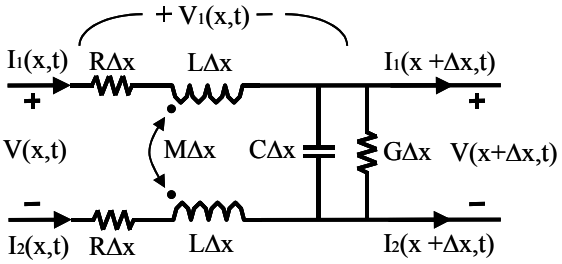

Figure 2-6: Equivalent circuit of an infinitesimal length Δx of an L-C cell in a generalized transmission structure.

From Figure 2-6, noting that

$$\begin{cases} \lim\limits_{\Delta x\to 0}\dfrac{V(x+\Delta x,t)-V(x,t)}{\Delta x}=\dfrac{\partial}{\partial x}V(x,t) \\ \lim\limits_{\Delta x\to 0}\dfrac{I_1(x+\Delta x,t)-I_1(x,t)}{\Delta x}=\dfrac{\partial}{\partial x}I_1(x,t) \\ \lim\limits_{\Delta x\to 0}\dfrac{I_2(x+\Delta x,t)-I_2(x,t)}{\Delta x}=\dfrac{\partial}{\partial x}I_2(x,t) \end{cases} \tag{2-1}$$

Kirchhoff's loop and node equations for the circuit shown in Figure 2-6 yield

$$\begin{cases} -\dfrac{\partial}{\partial x}V(x,t)=(L-M)\dfrac{\partial}{\partial t}[I_1(x,t)-I_2(x,t)]+R\cdot[I_1(x,t)-I_2(x,t)] \\ -\dfrac{\partial}{\partial x}I_1(x,t)=C\dfrac{\partial}{\partial t}V(x,t)+G\cdot V(x,t)=\dfrac{\partial}{\partial x}I_2(x,t) \end{cases} \tag{2-2}$$

For the special case in which the voltage and the current are periodic quantities of period $2\pi/\omega$, the first-order partial-differential equations for the phasor voltage and current become

$$\begin{cases} -\dfrac{d}{dx}V(x)=2[R+j\omega(L-M)]I_{DM}(x)=zI_{1-2}(x) \\ -\dfrac{d}{dx}I_{DM}(x)=(G+j\omega C)V(x)=yV(x) \end{cases} \tag{2-3}$$

in which,

$$I_{DM}(x)=\frac{I_1(x)-I_2(x)}{2} \tag{2-4}$$

$$z=2[R+j\omega(L-M)] \tag{2-5}$$

$$y=G+j\omega C \tag{2-6}$$

In a similar manner, we can obtain the second order partial-differential equations for either the voltage or the current:

$$\begin{cases} \dfrac{d^2V(x)}{dx^2} - \gamma^2 V(x) = 0 \\ \dfrac{d^2 I_{DM}(x)}{dx^2} - \gamma^2 I_{DM}(x) = 0 \end{cases} \tag{2-7}$$

in which, the propagation coefficient

$$\gamma = \sqrt{zy} = \sqrt{2[R + j\omega(L-M)][G + j\omega C]} = \alpha + j\beta \tag{2-8}$$

The characteristic impedance

$$Z_0 = \sqrt{\frac{z}{y}} = \sqrt{\frac{2[R + j\omega(L-M)]}{G + j\omega C}} \tag{2-9}$$

The wavelength

$$\lambda = \frac{2\pi}{\beta} \tag{2-10}$$

The following results can be obtained from the general solutions of (2-7)

$$\begin{cases} V(x) = V_a e^{-\gamma x} + V_b e^{\gamma x} \\ I_{DM}(x) = I_a e^{-\gamma x} + I_b e^{\gamma x} = \dfrac{V_a}{Z_0} e^{-\gamma x} - \dfrac{V_b}{Z_0} e^{\gamma x} \end{cases} \tag{2-11}$$

From equations (2-1)-(2-10), it is obvious that they reduce to those of a classical balanced transmission line when $I_1(x,t)=-I_2(x,t)$, or the classical transmission line is just a special case of the generalized transmission structure. The equivalent circuit of an infinitesimal length Δx of a generalized transmission structure and a conventional two-conductor balanced transmission line are compared in Figure 2-7. Referring to the generalized equivalent circuit in Figure 2-6, it can be found out that $R_A=2R$, $L_A=2(L-M)$, $G_A=G$, $C_A=C$. Additionally, they have the same propagation coefficients and characteristic impedance.

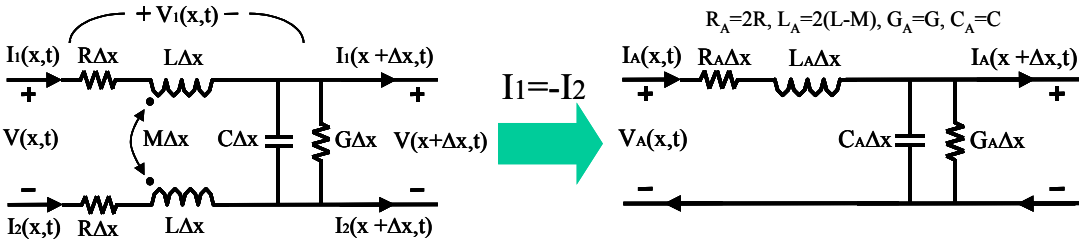

(a) Generalized transmission structure (a) Conventional transmission line

Figure 2-7: Equivalent circuit of an infinitesimal length Δx of a generalized transmission structure and a conventional balanced transmission line.

2.3. Impedance Calculations

2.3.1. Impedance Z_{AD} with load across BC

Before extending this generalized transmission structure to other integrated passives applications, impedance Z_{AD} with a load Z_L connected across B and C, as shown in Figure 2-8, needs to be investigated. In Figure 2-8, AC and BD represent the two conductors of a transmission line. The structure has a length of l. Z_{AD} is the impedance when applying a voltage across A and D and letting current I flow in at A and out at D.

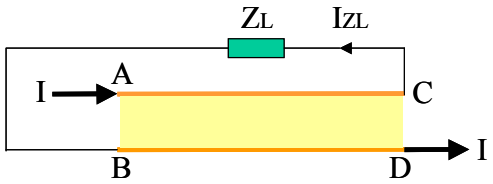

Figure 2-8: Current flowing direction for impedance Z_{AD} calculation with load across B and C.

Assume that at each infinitesimal length,

$$I_1(x) + I_2(x) = I + I_{ZL} \tag{2-12}$$

we obtain

$$\begin{cases} I_1(x) = \dfrac{I + I_{ZL}}{2} + I_{DM}(x) \\ I_2(x) = \dfrac{I + I_{ZL}}{2} - I_{DM}(x) \end{cases} \tag{2-13}$$

Therefore,

$$\begin{aligned} V_{AC} &= \int_A^C V_1(x) = \int_0^l [I_1(x)(R + j\omega L) + I_2(x) j\omega M]dx \\ &= (R + j\omega L)\int_0^l I_1(x)dx + j\omega M \int_0^l I_2(x)dx \\ &= \frac{(R + j\omega L)}{2}\left[2\int_0^l I_{DM}(x)dx + \int_0^l (I + I_{ZL})dx\right] + \frac{j\omega M}{2}\left[\int_0^l (I + I_{ZL})dx - 2\int_0^l I_{DM}(x)dx\right] \\ &= \frac{R + j\omega(L+M)}{2}(I + I_{ZL})\cdot l + [R + j\omega(L-M)]\frac{1}{Z_0\gamma}[V_a(1-e^{-\gamma l}) + V_b(1-e^{\gamma l})] \\ &= \frac{R + j\omega(L+M)}{2}(I + I_{ZL})\cdot l + \frac{1}{2}[V_a(1-e^{-\gamma l}) + V_b(1-e^{\gamma l})] \end{aligned} \tag{2-14}$$

It is known that

$$\begin{cases} I_1(0) = I \\ I_2(0) = I_{ZL} \\ I_1(l) = I_{ZL} \\ I_2(l) = I \end{cases} \tag{2-15}$$

We have the following boundary conditions

$$\begin{cases} V_{AB} - V_{AC} = I_{ZL} \cdot Z_L \\ I_{DM}(0) = \dfrac{I - I_{ZL}}{2} \\ I_{DM}(l) = \dfrac{I_{ZL} - I}{2} \end{cases} \tag{2-16}$$

It is known that $V_{AB}=V_a+V_b$, (2-16) can be manipulated into

$$\begin{cases} \dfrac{1}{2}[V_a(1+e^{-\gamma l}) + V_b(1+e^{\gamma l})] - \dfrac{R+j\omega(L+M)}{2}(2I - \dfrac{2V_a}{Z_0} + \dfrac{2V_b}{Z_0}) \cdot l = (I - \dfrac{2V_a}{Z_0} + \dfrac{2V_b}{Z_0}) \cdot Z_L \\ V_a = \dfrac{V_b(1+e^{\gamma l})}{1+e^{-\gamma l}} \end{cases} \tag{2-17}$$

which yields

$$\begin{cases} V_a = \dfrac{V_b(1+e^{\gamma l})}{1+e^{-\gamma l}} \\ V_b = IZ_0 \dfrac{\left\{\dfrac{Z_L}{Z_0} + \dfrac{[R+j\omega(L+M)]l}{Z_0}\right\}(1+e^{-\gamma l})}{2+e^{\gamma l}+e^{-\gamma l}+(e^{\gamma l}-e^{-\gamma l})\left[\dfrac{R+j\omega(L+M)}{Z_0}l + \dfrac{2Z_L}{Z_0}\right]} \end{cases} \tag{2-18}$$

The impedance Z_{AD} can be obtained by

$$Z_{AD} = \frac{V_{AD}}{I} = \frac{V_{AC}+V_{CD}}{I} = \frac{R+j\omega(L+M)}{2I} l\left[2I - 2\frac{V_a - V_b}{Z_0}\right] + \frac{1}{2I}\left[V_a(1+e^{-\gamma l}) + V_b(1+e^{\gamma l})\right]$$

$$= \frac{\left[R+j\omega(L+M)\right] \cdot l \cdot \left[\dfrac{2}{\sinh(\gamma l)} + \dfrac{2}{\tanh(\gamma l)} + \dfrac{2Z_L}{Z_0}\right] + Z_L\left[\dfrac{1}{\sinh(\gamma l)} + \dfrac{1}{\tanh(\gamma l)} - \dfrac{[R+j\omega(L+M)]l}{Z_0}\right]}{\dfrac{1}{\sinh(\gamma l)} + \dfrac{1}{\tanh(\gamma l)} + \dfrac{[R+j\omega(L+M)]l}{Z_0} + \dfrac{2Z_L}{Z_0}} \tag{2-19}$$

Typical impedances versus frequency characteristics with various resistive loads are shown in Figure 2-9. Impedance Z_{AD} with various capacitive loads, inductive loads and both across B and C are shown in Figure 2-10, Figure 2-11, Figure 2-12, respectively. The parameters assumed in these calculations are shown in Table 2-1.

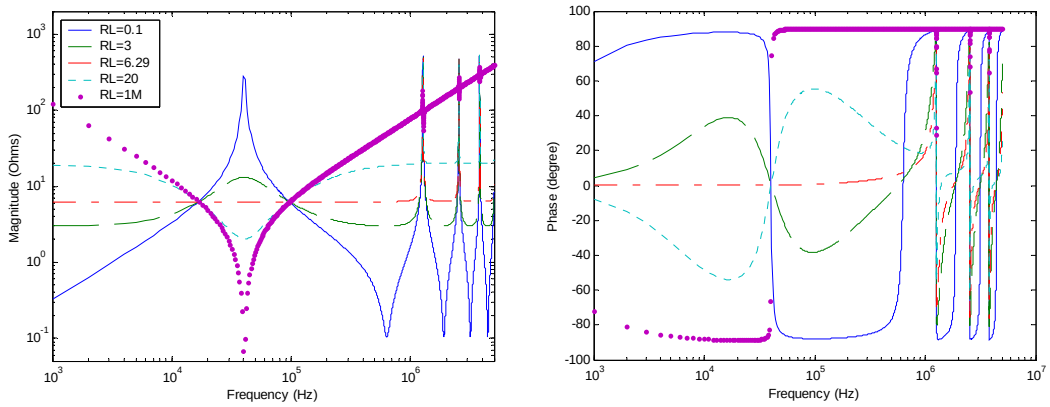

(a) Magnitude (b) Phase

Figure 2-9: Impedance Z_{AD} with various resistive loads across B and C.

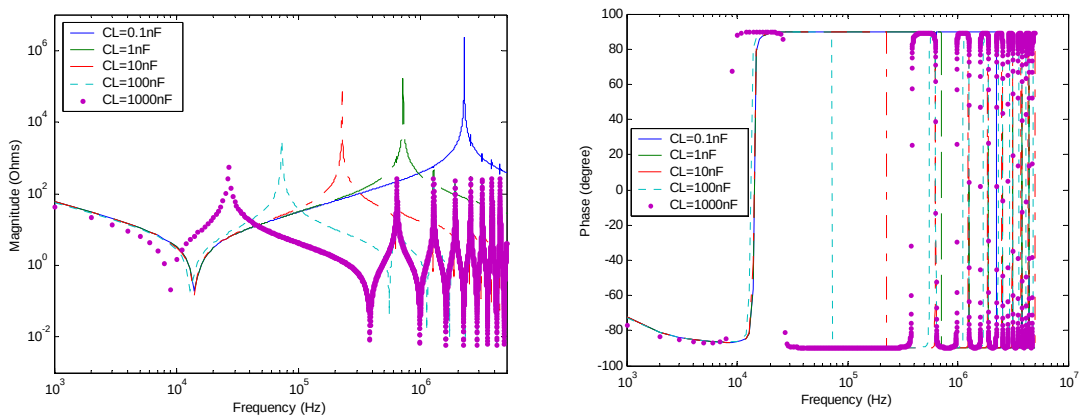

Figure 2-10: Impedance Z_{AD} with various capacitive loads across B and C.

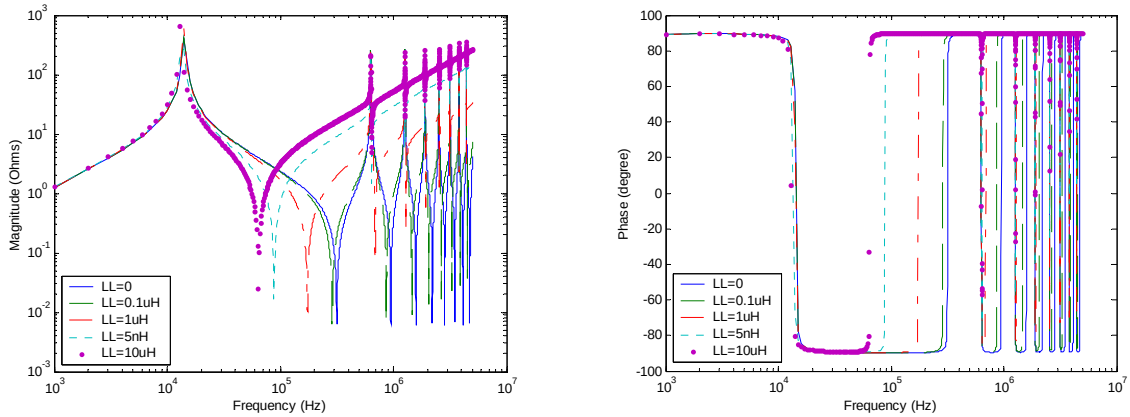

Figure 2-11: Impedance Z_{AD} with various inductive loads across B and C.

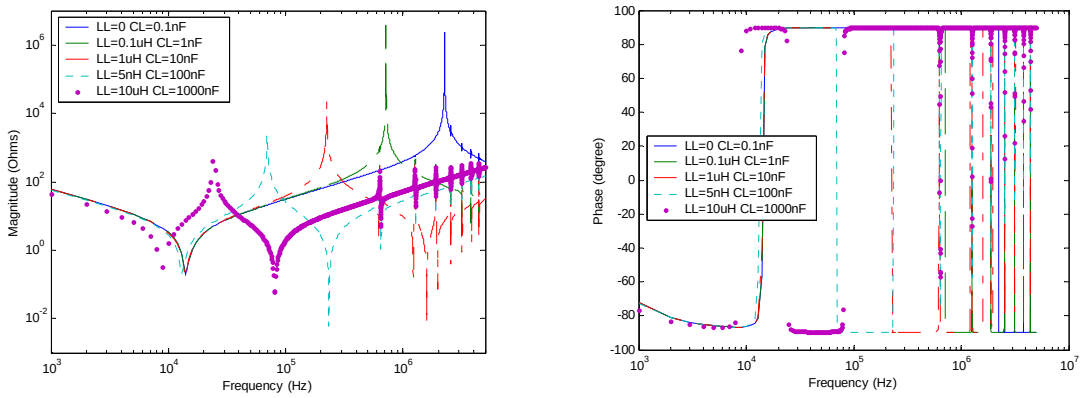

Figure 2-12: Impedance Z_{AD} with various capacitive and inductive loads across B and C.

Table 2-1: Technical parameters assumed for the calculation in Figure 2-9

Inductance per unit length L	50μH/m
Capacitance per unit length C	5μF/m
Mutual inductance per unit length M	49μH/m
Resistance per unit length R	0.01Ω/m
Conductance per unit length G	0.01/(Ω·m)
Total length of the transmission line	250mm

Equation (2-19) can be manipulated into

$$Z_{AD} = \frac{Z_L\left\{\frac{1}{\sinh(\gamma l)}+\frac{1}{\tanh(\gamma l)}+\frac{[R+j\omega(L+M)]l}{Z_0}+\frac{[R+j\omega(L+M)]\cdot l}{Z_L}\left[\frac{2}{\sinh(\gamma l)}+\frac{2}{\tanh(\gamma l)}\right]\right\}}{\frac{1}{\sinh(\gamma l)}+\frac{1}{\tanh(\gamma l)}+\frac{[R+j\omega(L+M)]l}{Z_0}+\frac{2Z_L}{Z_0}} \quad (2\text{-}20)$$

From (2-20), it is obvious that Z_{AD} equals Z_L when

$$Z_L = \sqrt{Z_0[R+j\omega(L+M)]\cdot l\cdot\left[\frac{1}{\sinh(\gamma l)}+\frac{1}{\tanh(\gamma l)}\right]} \quad (2\text{-}21)$$

When R and G are negligible, L-M<<L, Z_{AD} appears to be a constant resistance at low frequency, as shown in the dot-dashed curve in Figure 2-9, approximately when

$$Z_L = R_{L_cri} = \sqrt{\frac{2(L+M)}{C}} \quad (2\text{-}22)$$

R_{L_cri} is the so-called critical load resistance. Z_{AD} approaches series resonance when R_L increases and approaches parallel resonance when R_L decreases.

For the no load case, or $Z_L=\infty$, as shown in Figure 2-13(a),

$$Z_{AD} = \frac{R+j\omega(L+M)}{2}l+\frac{Z_0}{2}\left[\frac{1}{\sinh(\gamma l)}+\frac{1}{\tanh(\gamma l)}\right] \quad (2\text{-}23)$$

When the two conductors have a very good magnetic coupling and R=G=0 (lossless case), from (2-5)-(2-10), we have l<<2π/β, sinβl≅βl, therefore

$$Z_{AD} \cong \frac{j\omega(L+M)}{2} l - j\frac{1}{\omega C \cdot l} \tag{2-24}$$

The simplified lumped equivalent circuit is shown in Figure 2-13(b). The impedance approximately equals an inductance *(L+M)l/2* in series with a capacitance *C·l,* as shown in Figure 2-13(c). This is the theoretical basis for integrated series resonators. If k=1, the total inductance equals *4Ll* [9]. The equivalent circuit of an ideal series resonator is shown in Figure 2-13(b).

(a) Interconnections and current flowing direction

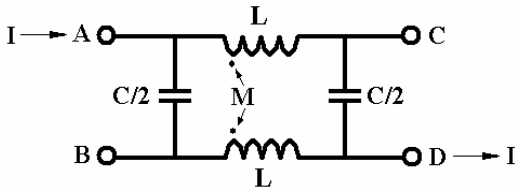

(b) The lumped equivalent circuit

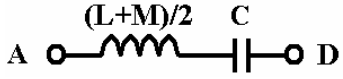

(c) The first order approximation

Figure 2-13: An integrated series resonator.

Figure 2-14(a)(b)(c)(d) show the impedance Z_{AD} versus frequency with the coupling coefficient k=1, 0.99, 0.7 and 0.5, respectively. The transmission structure is a perfect series resonator when k=1. With k=0.99 which is still a good coupling, there are only some insignificant spikes at high frequency and could be damped out provided there is a higher loss at high frequency. However, the high frequency oscillations become significant when k becomes lower. As part of the design considerations, decreasing the spacing between conductors and increasing the conductor width help to increase k. Besides that, employing ferrite cores in a practical design can provide not only a higher inductance but also a better magnetic coupling between conductors.

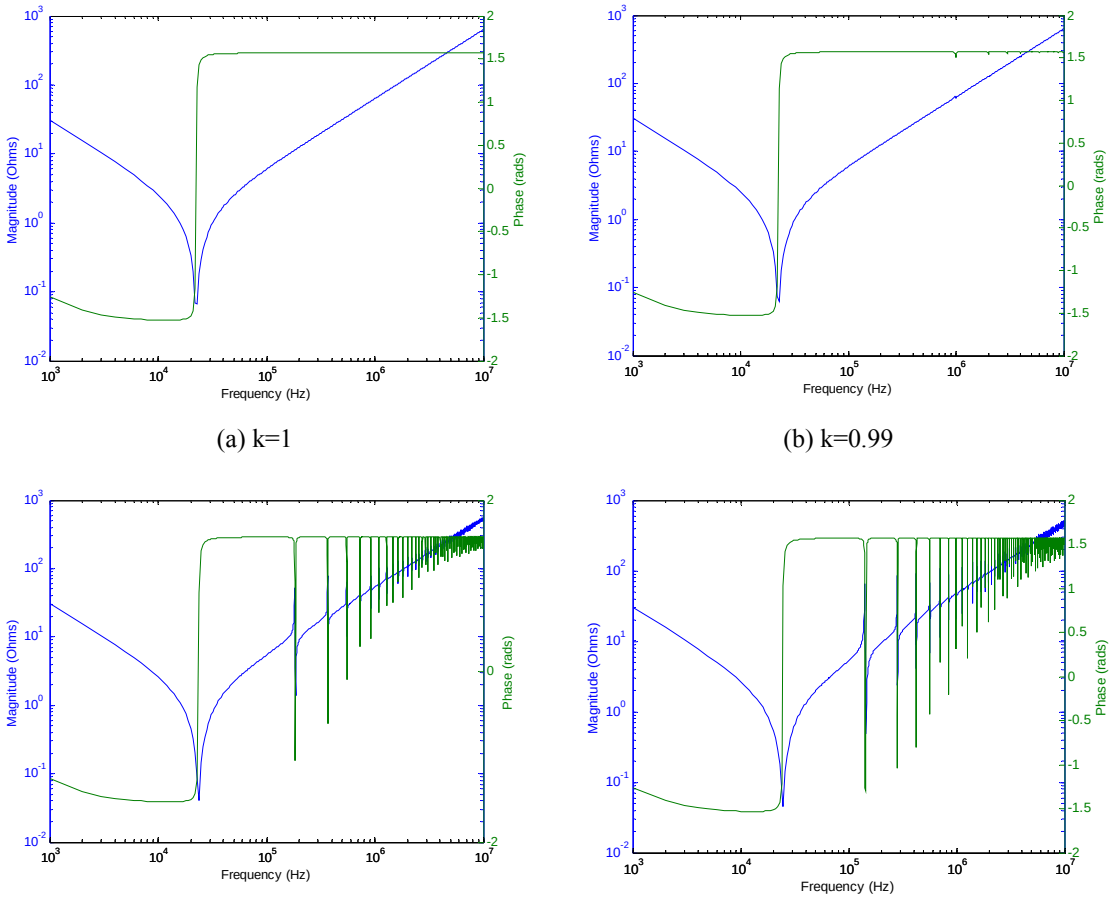

(a) k=1 (b) k=0.99

(c) k=0.7 (d) k=0.5

Figure 2-14: Z_{AD} with various coupling coefficients k.

When the load is short-circuited, or Z_L=0, as shown in Figure 2-15(a),

$$Z_{AD} = \frac{[R + j\omega(L+M)]\cdot l \cdot \left[\frac{2}{\sinh(\gamma l)} + \frac{2}{\tanh(\gamma l)}\right]}{\frac{1}{\sinh(\gamma l)} + \frac{1}{\tanh(\gamma l)} + \frac{[R + j\omega(L+M)]l}{Z_0} + \frac{2Z_L}{Z_0}} \tag{2-25}$$

and R=G=0 (lossless case), from (2-5)-(2-10), assume $l \ll 2\pi/\beta$, $\sin\beta l \cong \beta l$, $\cos\beta l \cong 1$, therefore

$$Z_{AD} \cong \frac{1}{\frac{1}{2j\omega(L+M)l} + \frac{1}{\frac{4}{j\omega Cl}}} \tag{2-26}$$

The simplified lumped equivalent circuit is shown in Figure 2-15(b). The impedance approximately equals an inductance *2(L+M)l* in parallel with a capacitance *C·l/4*, as

shown in Figure 2-15(c). This is the theoretical basis for integrated parallel resonators. The first order approximation equivalent circuit of an ideal parallel resonator is shown in Figure 2-15(b).

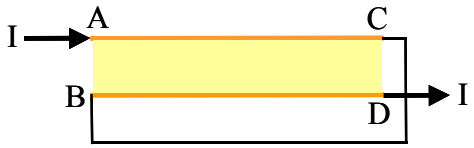

(a) Interconnections and current flowing direction

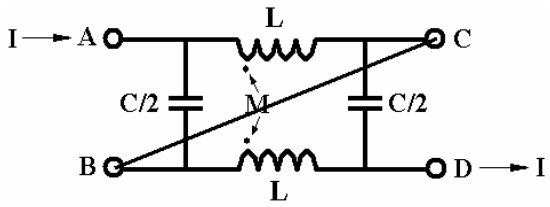

(b) The lumped equivalent circuit

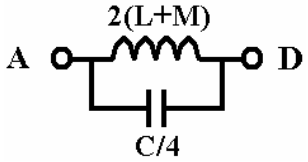

(c) The first order approximation

Figure 2-15: An integrated parallel resonator.

Z_{AD} has a parallel resonance at low frequency. The typical impedance characteristics of Z_{AD} with different magnetic coupling coefficients when Z_L=0 are plotted in Figure 2-16. Apparently, the higher the coupling coefficient, the closer this transmission structure approximates an ideal parallel resonator.

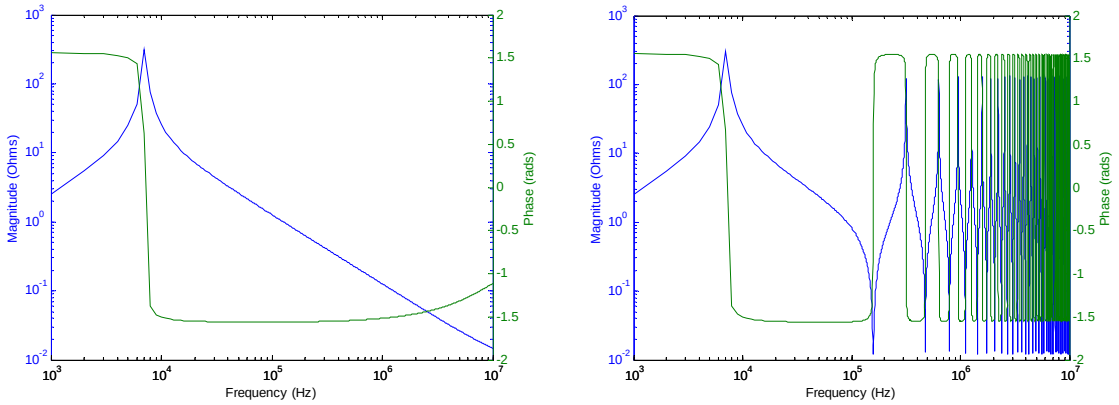

(a) k=1 (b) k=0.99

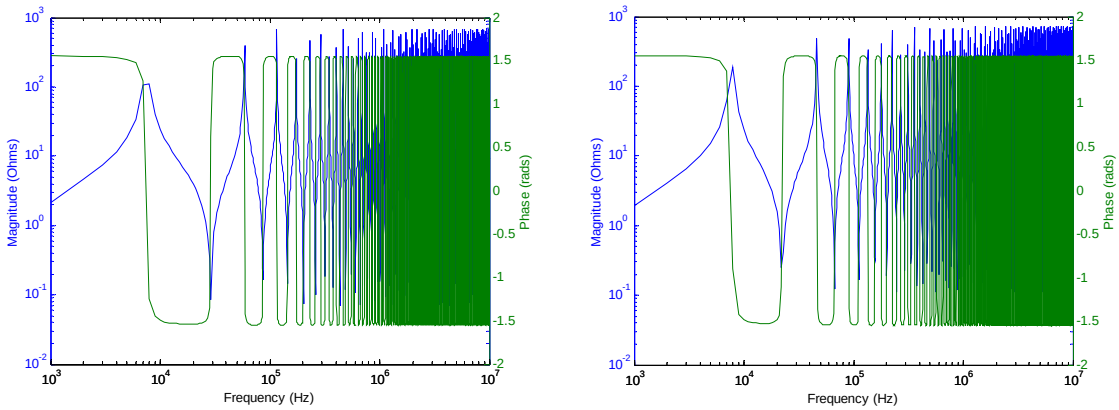

(c) k=0.7 (d) k=0.5

Figure 2-16: Typical Z_{AD} with Z_L=0.

2.3.2. Impedance Z_{AD} with load across AC

Another case to be investigated is a generalized transmission structure with a load Z_L connected across A and C, as shown in Figure 2-17.

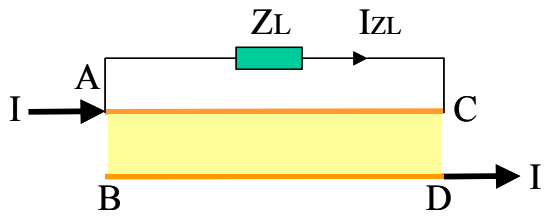

Figure 2-17: Current flowing direction for impedance Z_{AD} calculation with load across B and C.

Assume that at each infinitesimal length,

$$I_1(x) + I_2(x) = I_1(0) \tag{2-27}$$

We obtain

$$\begin{cases} I_1(x) = \dfrac{I_1(0)}{2} + I_{DM}(x) \\ I_2(x) = \dfrac{I_1(0)}{2} - I_{DM}(x) \end{cases} \tag{2-28}$$

Therefore,

$$\begin{aligned} V_{AC} &= \int_A^C V_1(x) = \int_0^l [I_1(x)(R + j\omega L) + I_2(x) j\omega M]dx \\ &= (R + j\omega L)\int_0^l I_1(x)dx + j\omega M \int_0^l I_2(x)dx \\ &= \frac{(R + j\omega L)}{2}\left[2\int_0^l I_{DM}(x)dx + \int_0^l I_1(0)dx\right] + \frac{j\omega M}{2}\left[\int_0^l I_1(0)dx - 2\int_0^l I_{DM}(x)dx\right] \\ &= \frac{R + j\omega(L+M)}{2} I_1(0)\cdot l + \frac{R + j\omega(L-M)}{Z_0\gamma}[V_a(1-e^{-\gamma l}) + V_b(1-e^{\gamma l})] \\ &= \frac{R + j\omega(L+M)}{2} I_1(0)\cdot l + \frac{1}{2}[V_a(1-e^{-\gamma l}) + V_b(1-e^{\gamma l})] \end{aligned} \tag{2-29}$$

The voltage and current boundary conditions are given by

$$\begin{cases} V_{AC} = I_{ZL}\cdot Z_L \\ I_1(0) + I_{ZL} = I \\ I_1(l) + I_{ZL} = 0 \\ I_2(l) = I \end{cases} \tag{2-30}$$

which can be rewritten as

$$\begin{cases} V_{AC} = I_{ZL}\cdot Z_L \\ I_{DM}(0) = \dfrac{I_1(0)}{2} = \dfrac{I - I_{ZL}}{2} \\ I_{DM}(l) = \dfrac{-I_{ZL} - I}{2} \end{cases} \tag{2-31}$$

or

$$\begin{cases} \dfrac{R + j\omega(L+M)}{2}(I - I_{ZL})\cdot l + \dfrac{1}{2}[V_a(1-e^{-\gamma l}) + V_b(1-e^{\gamma l})] = I_{ZL}\cdot Z_L \\ \dfrac{V_a}{Z_0} - \dfrac{V_b}{Z_0} = \dfrac{I - I_{ZL}}{2} \\ \dfrac{V_a}{Z_0}e^{-\gamma l} - \dfrac{V_b}{Z_0}e^{\gamma l} = \dfrac{-I_{ZL} - I}{2} \end{cases} \tag{2-32}$$

which yields

$$\begin{cases} V_a = \dfrac{IZ_0 + V_b(1-e^{\gamma l})}{1-e^{-\gamma l}} \\ V_b = IZ_0 \dfrac{\dfrac{Z_L}{Z_0}(1+e^{-\gamma l}) + \dfrac{1-e^{-\gamma l}}{2} + \dfrac{[R+j\omega(L+M)]l}{Z_0}}{\dfrac{2(e^{\gamma l}-e^{-\gamma l})}{Z_0}\left[\dfrac{R+j\omega(L+M)}{2}l + Z_L\right] - 2 + e^{\gamma l} + e^{-\gamma l}} \end{cases} \tag{2-33}$$

As a result, the impedance across A and D can be obtained by dividing V_{AD} by I:

$$Z_{AD} = \frac{V_{AD}}{I} = \frac{V_{AC}+V_{CD}}{I} = \frac{R+j\omega(L+M)}{Z_0} l(V_a - V_b) + \frac{1}{2I}\left[V_a(1+e^{-\gamma l}) + V_b(1+e^{\gamma l})\right]$$

$$= \frac{R+j\omega(L+M)}{Z_0} l \frac{Z_0 + V_b(e^{-\gamma l} - e^{\gamma l})/I}{1-e^{-\gamma l}} + \frac{Z_0(1+e^{-\gamma l})}{2(1-e^{-\gamma l})}$$

$$= \frac{R+j\omega(L+M)}{2} l \frac{2 + \dfrac{\dfrac{2Z_L}{Z_0}(1+e^{-\gamma l}) + 1 - e^{-\gamma l} + \dfrac{2[R+j\omega(L+M)]l}{Z_0}}{\dfrac{e^{\gamma l}-e^{-\gamma l}}{Z_0}\{[R+j\omega(L+M)]l + 2Z_L\} - 2 + e^{\gamma l} + e^{-\gamma l}}(e^{-\gamma l} - e^{\gamma l})}{1-e^{-\gamma l}} + \frac{Z_0(1+e^{-\gamma l})}{2(1-e^{-\gamma l})}$$

$$= \frac{R+j\omega(L+M)}{2} l \frac{2 + \dfrac{\dfrac{2Z_L}{Z_0}(1+e^{-\gamma l}) + 1 - e^{-\gamma l} + \dfrac{2[R+j\omega(L+M)]l}{Z_0}}{-\left[\dfrac{R+j\omega(L+M)}{Z_0}l + \dfrac{2Z_L}{Z_0}\right] + \dfrac{1}{\sinh(\gamma l)} - \dfrac{1}{\tanh(\gamma l)}}}{1-e^{-\gamma l}} + \frac{Z_0(1+e^{-\gamma l})}{2(1-e^{-\gamma l})} \tag{2-34}$$

For no load case, or $Z_L=\infty$, it can be obtained that

$$Z_{AD} = \frac{R+j\omega(L+M)}{2} l + \frac{Z_0}{2}\left[\frac{1}{\sinh(\gamma l)} + \frac{1}{\tanh(\gamma l)}\right] \tag{2-35}$$

which is the same as the Z_{AD} of a single generalized transmission line as given in (2-23).

When Z_L is a capacitive or inductive load, the typical impedance characteristics of Z_{AD} are plotted in Figure 2-18(a) and (b), respectively. The parameters assumed in these calculations are shown in Table 2-2. A capacitive load across A and C will result in a high frequency parallel resonant peak on the impedance curve, as demonstrated in Figure 2-18(a). This emulates the impedance of a series resonant transmission structure, taking the intra-winding capacitance into account.

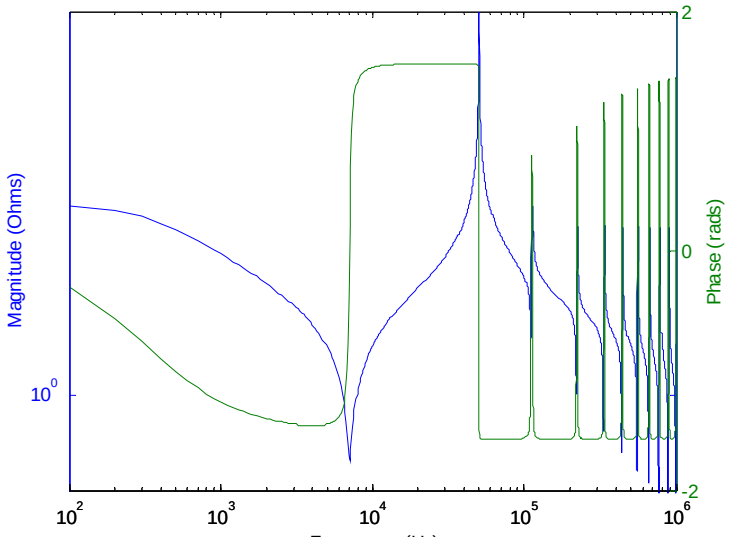

(a) Capacitive load Z_L=100nF

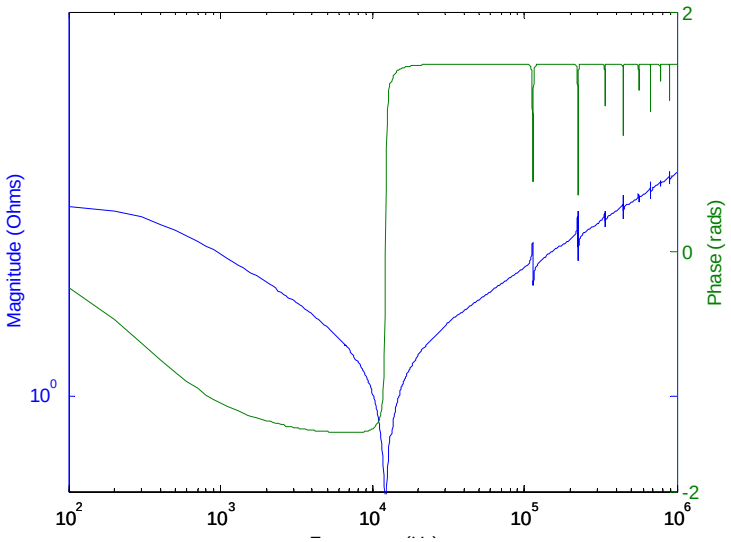

(b) Inductive load Z_L=50μH

Figure 2-18: Impedance of ZAD with various loads at AC.

Table 2-2: Technical parameters assumed for the calculation in Figure 2-18

L	100μH/m
M	98μH/m
C	5μF/m
R	0.01Ω/m
G	0.01Ω/m
l	1m

2.3.3. Impedance Z_{AC}

Z_{AC} is the impedance when applying a voltage across A and C and letting current I flow in at A and out at C, as shown in Figure 2-19.

Figure 2-19: Current flowing direction for impedance Z_{AC} calculation.

Assume that at each infinitesimal length,

$$I_1(x) + I_2(x) = I \tag{2-36}$$

From the boundary conditions

$$\begin{cases} I_{DM}(0) = \dfrac{I}{2} \\ I_{DM}(l) = \dfrac{I}{2} \end{cases} \tag{2-37}$$

or

$$\begin{cases} \dfrac{V_a}{Z_0} - \dfrac{V_b}{Z_0} = \dfrac{I}{2} \\ \dfrac{V_a}{Z_0} e^{-\gamma l} - \dfrac{V_b}{Z_0} e^{\gamma l} = \dfrac{I}{2} \end{cases} \tag{2-38}$$

Seeking solutions to (2-38), we obtain

$$\begin{cases} V_a = V_b + IZ_0 = \dfrac{IZ_0(e^{\gamma l} - 1)}{2(e^{\gamma l} - e^{-\gamma l})} \\ V_b = \dfrac{IZ_0(e^{-\gamma l} - 1)}{2(e^{\gamma l} - e^{-\gamma l})} \end{cases} \tag{2-39}$$

The voltage across A and C

$$V_{AC} = \frac{R + j\omega(L+M)}{2} I \cdot l + \frac{1}{2}[V_a(1 - e^{-\gamma l}) + V_b(1 - e^{\gamma l})] \tag{2-40}$$

The impedance Z_{AC} can be obtained by

$$Z_{AC} = \frac{V_{AC}}{I} = \frac{R + j\omega(L+M)}{2} l + \frac{Z_0}{2}\left[\frac{1}{\tanh(\gamma l)} - \frac{1}{\sinh(\gamma l)}\right] \tag{2-41}$$

The typical impedance of Z_{AC} is plotted in Figure 2-20.

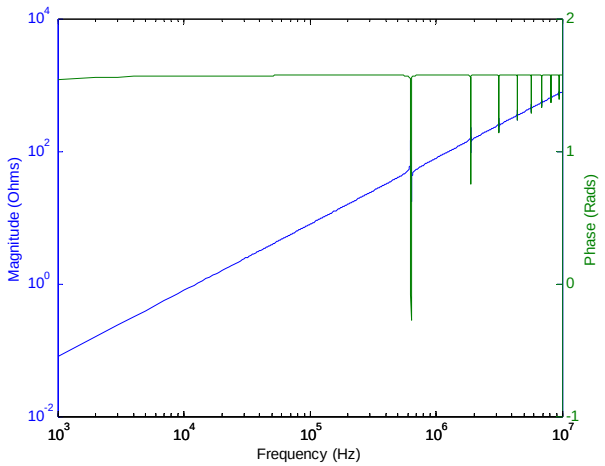

Figure 2-20: Typical impedance Z_{AC}.

2.3.4. Impedance Z_{AB}

Z_{AB} is the impedance when applying a voltage across A and B and letting current I flowing in from A and out from B, as shown in Figure 2-21.

Figure 2-21: Current flowing direction for impedance Z_{AB} calculation.

Assume that at each infinitesimal length,

$$I_1(x) = -I_2(x) \tag{2-42}$$

From the boundary conditions

$$\begin{cases} I_{DM}(0) = I \\ I_{DM}(l) = 0 \end{cases} \tag{2-43}$$

or

$$\begin{cases} \dfrac{V_a}{Z_0} - \dfrac{V_b}{Z_0} = I \\ \dfrac{V_a}{Z_0} e^{-\gamma l} - \dfrac{V_b}{Z_0} e^{\gamma l} = 0 \end{cases} \tag{2-44}$$

Seeking solutions to (2-44), we obtain

$$\begin{cases} V_a = V_b e^{2\gamma l} = \dfrac{IZ_0 e^{2\gamma l}}{e^{2\gamma l} - 1} \\ V_b = \dfrac{IZ_0}{e^{2\gamma l} - 1} \end{cases} \tag{2-45}$$

The impedance Z_{AB} can be obtained by

$$Z_{AB} = \frac{V_{AB}}{I} = \frac{V(0)}{I} = \frac{V_a + V_b}{I} = Z_0 \frac{1}{\tanh(\gamma l)} \tag{2-46}$$

It is evident that these are the same as the conventional transmission line input impedance equations. The typical impedance of Z_{AB} is plotted in Figure 2-22.

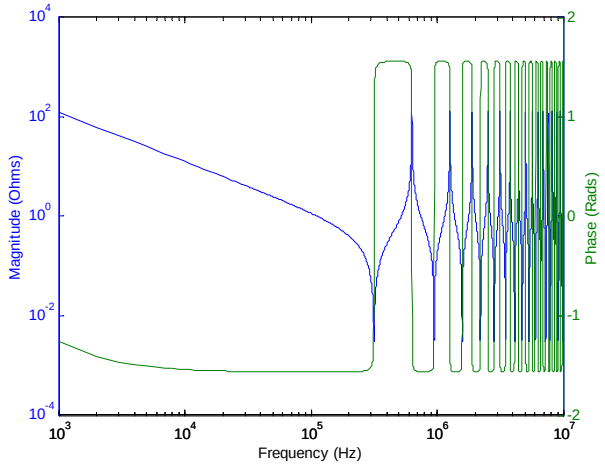

Figure 2-22: Typical impedance Z_{AB}.

2.4. Current and Voltage Distribution

The current and voltage distribution is another important issue for better understanding of the operation of a generalized transmission structure. It is also one of the essential basis for the relevant loss modeling [18]. However, the loss model in [18] is based on the assumption of linear current distribution. This may not be true at high frequency as being found for conventional transmission lines.

A generalized transmission structure with its parameters shown in Table 2-3 has the current and voltage distributions at various frequencies shown in Figure 2-23 and Figure 2-24, respectively. Figure 2-23(d) and Figure 2-24(d) shows the current and voltage distribution at 632kHz when the structure length equals the wavelength. The voltage and current

magnitudes become much higher under this frequency (or frequencies at which the structure length equals multiple integer wavelength) than those under other frequencies.

Table 2-3: PARAMETERS OF THE TRANSMISSION STRUCTURE

L	100μH/m
M	99μH/m
C	5μF/m
R	0.01Ω/m
G	0.01Ω/m
l	0.5m

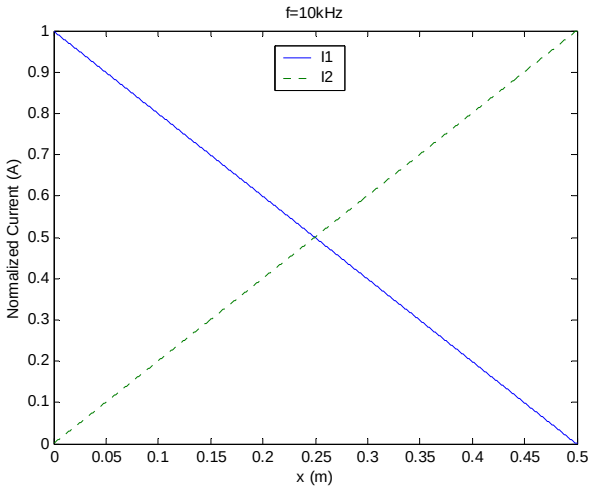

(a) f=10kHz

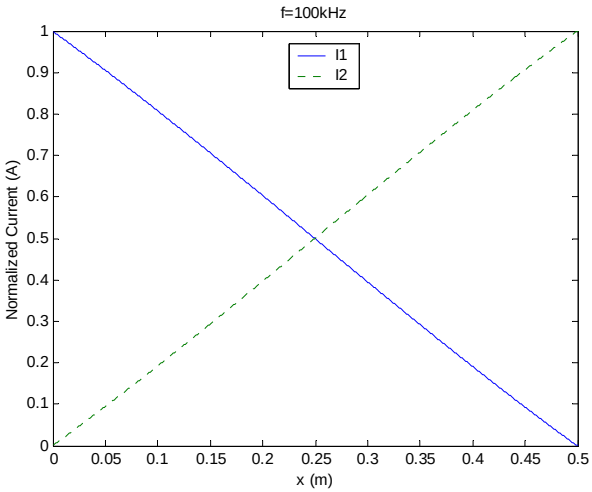

(b) f=100kHz

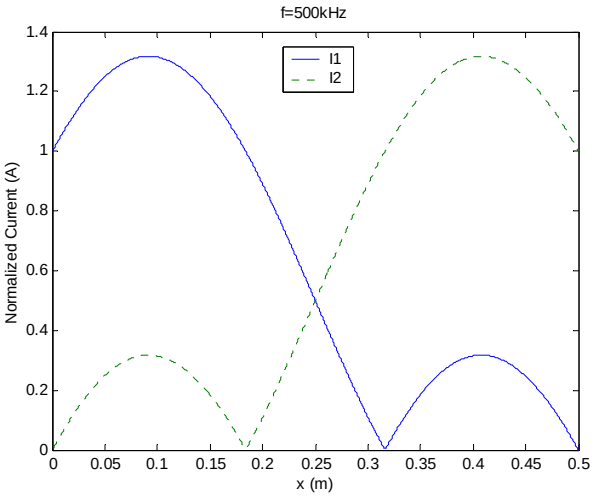

(c) f=500kHz

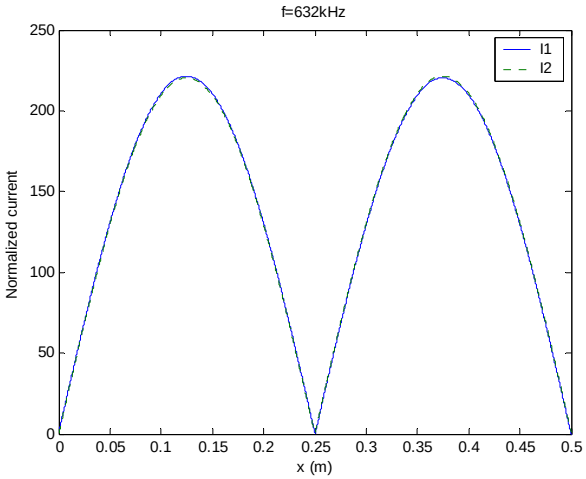

(d) f=632kHz

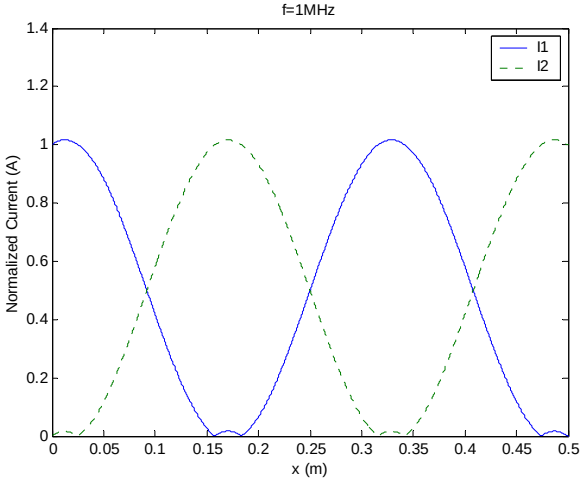

(e) f=1MHz

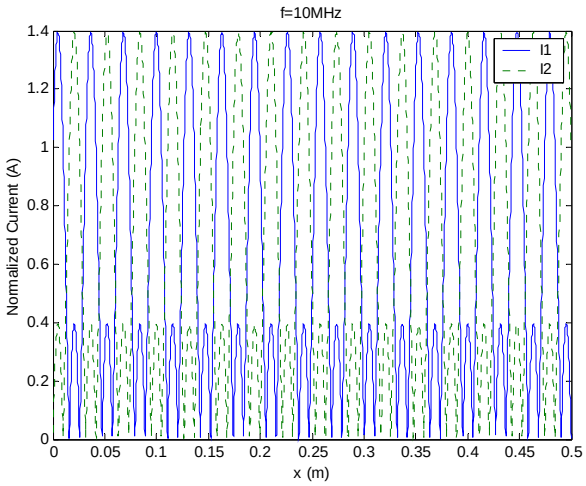

(f) f=10MHz

Figure 2-23: Normalized current (magnitude) distributions of the top and bottom conductors at various frequencies.

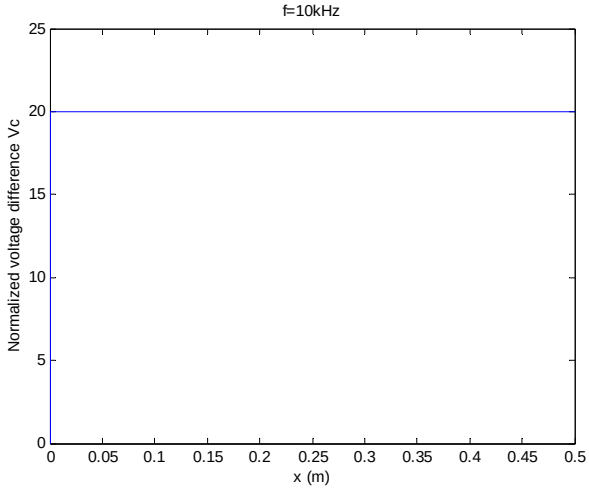

(a) f=10kHz

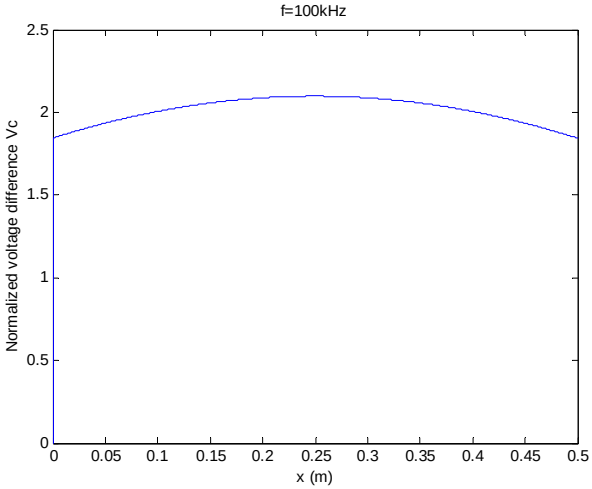

(b) f=100kHz

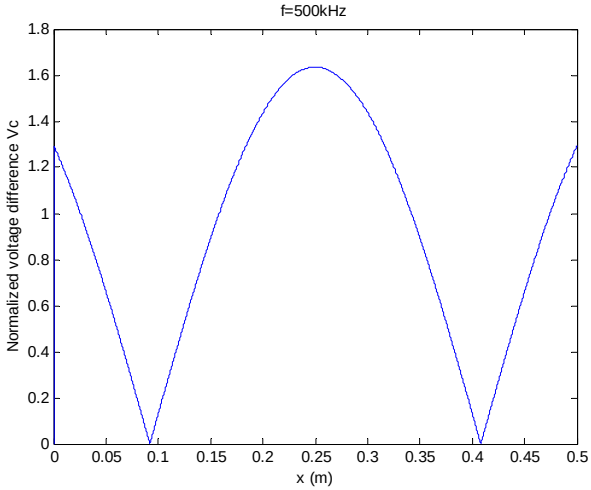

(c) f=500kHz

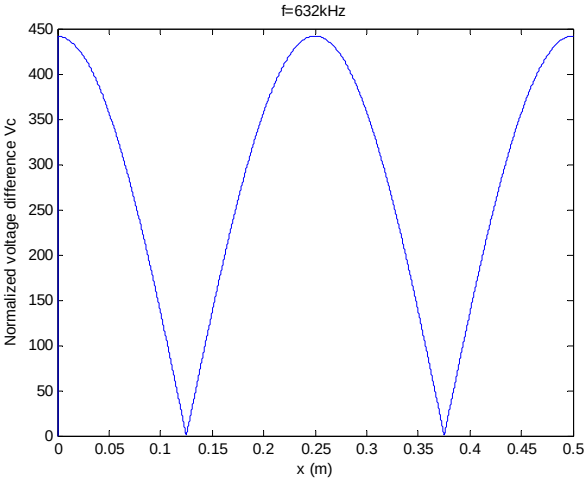

(d) f=632kHz

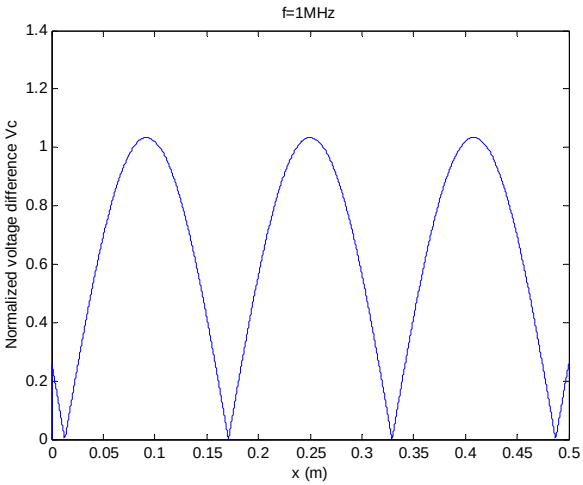

(e) f=1MHz

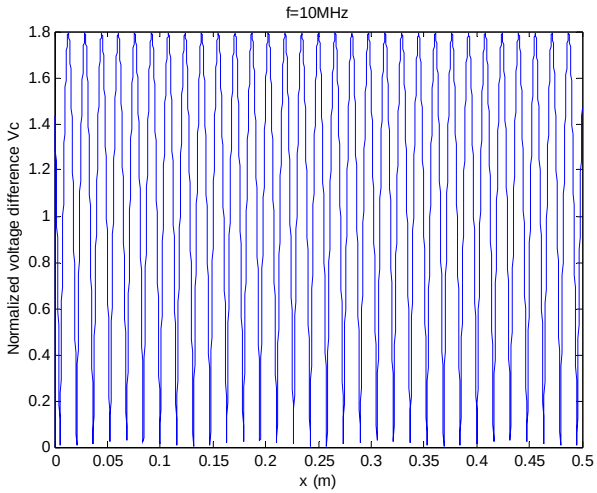

(f) f=10MHz

Figure 2-24: Normalized voltage (magnitude) distributions across the top and bottom conductors at various frequencies.

2.5. *Cascaded Transmission Line Model*

Generalized transmission structures are the basis for modeling integrated electromagnetic passives as developed [25]. However, a single transmission structure is not generally used in an integrated module in practice. As a practical structure, a spiral winding is normally used instead of a linear structure in passives integration [1][4][14][11][25]. Figure 2-25 shows the spiral winding transmission structure with each conductor labeled.

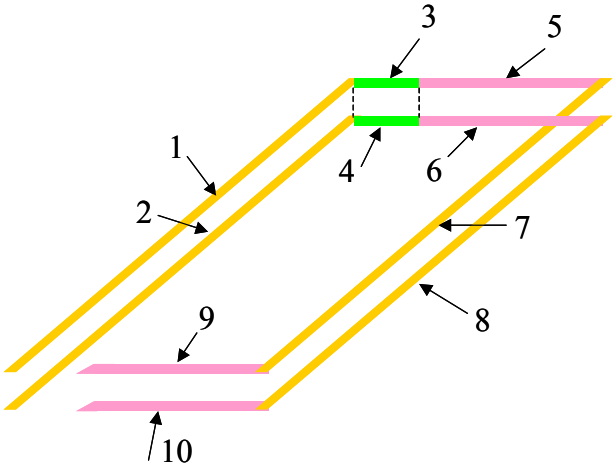

Figure 2-25: Spiral winding transmission structure.

The conductor voltages are given by

$$\begin{cases} -\frac{d}{dx}V_{1,2}(x) = (R_1 + j\omega L_1 - j\omega M_{2,1})I_1(x) + (j\omega M_{1,2} - R_2 - j\omega L_2)I_2(x) + (j\omega M_{1,7} - j\omega M_{2,7})I_7(x) + (j\omega M_{1,8} - j\omega M_{2,8})I_8(x) \\ -\frac{d}{dx}V_{3,4}(x) = (R_3 + j\omega L_3 - j\omega M_{4,3})I_3(x) + (j\omega M_{3,4} - R_4 - j\omega L_4)I_4(x) \\ -\frac{d}{dx}V_{5,6}(x) = (R_5 + j\omega L_5 - j\omega M_{6,5})I_5(x) + (j\omega M_{5,6} - R_6 - j\omega L_6)I_6(x) + (j\omega M_{5,9} - j\omega M_{6,9})I_9(x) + (j\omega M_{5,10} - j\omega M_{6,10})I_{10}(x) \\ -\frac{d}{dx}V_{7,8}(x) = (j\omega M_{7,1} - j\omega M_{8,1})I_1(x) + (j\omega M_{7,2} - j\omega M_{8,2})I_2(x) + (R_7 + j\omega L_7 - j\omega M_{8,7})I_7(x) + (j\omega M_{7,8} - R_8 - j\omega L_8)I_8(x) \\ -\frac{d}{dx}V_{9,10}(x) = (j\omega M_{9,5} - j\omega M_{10,5})I_5(x) + (j\omega M_{9,6} - j\omega M_{10,6})I_6(x) + (R_9 + j\omega L_9 - j\omega M_{10,9})I_9(x) + (j\omega M_{9,10} - R_{10} - j\omega L_{10})I_{10}(x) \end{cases} \quad (2\text{-}47)$$

When $M_{1,7} \cong M_{2,7}$, $M_{1,8} \cong M_{2,8}$, $M_{5,9} \cong M_{6,9}$, $M_{5,10} \cong M_{6,10}$, these equations are approximately the same as the equation (2-3). Then this structure can be unwound into an equivalent cascaded transmission structures.

The mutual inductances of four conductors in air are simulated in MAXWELL 2D field solver, as shown in Figure 2-26. Each conductor has a width of *w*, and a thickness of 5μm. There is a spacing *t* between 1and 2 as well as 3 and 4. *d* is the distance between 1and 3. Figure 2-27 shows the difference between $M_{1,3}$ and $M_{1,4}$ as a function of *t*, *d* and *w*. From the simulation results, the difference between $M_{1,3}$ and $M_{1,4}$ is normally below 1%, therefore can be neglected.

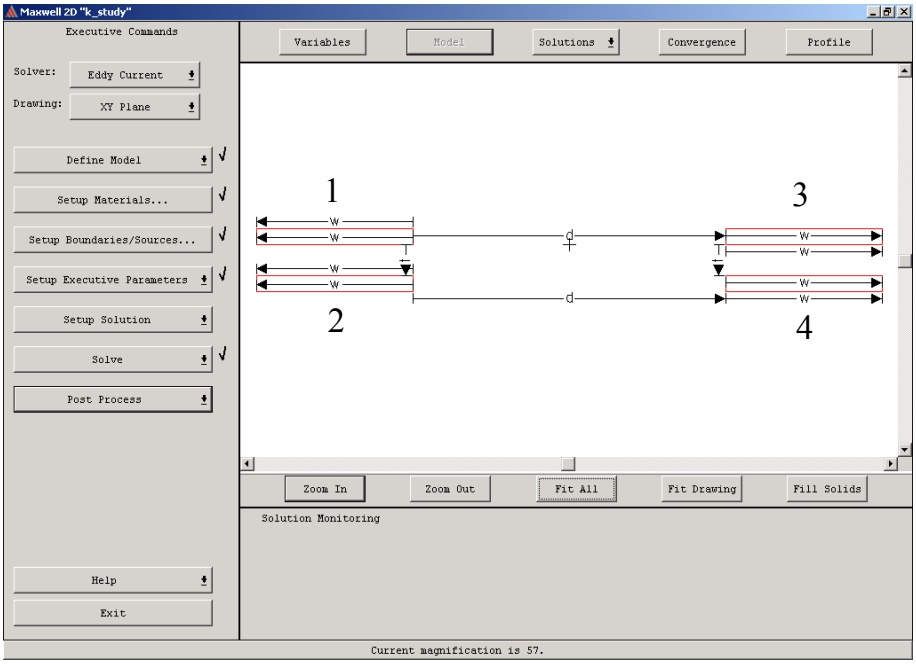

Figure 2-26: MAXWELL simulation model for the study of mutual inductance.

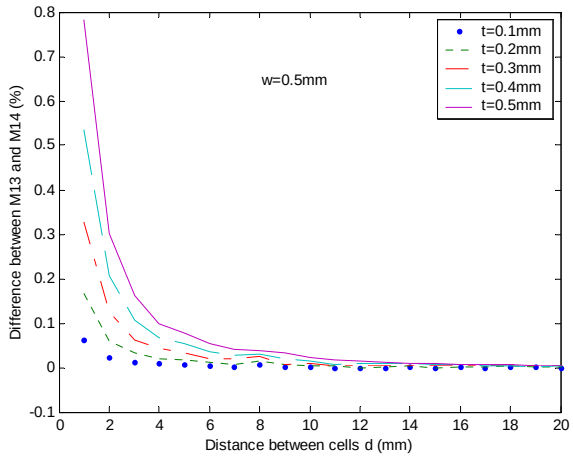

(a) Difference between $M_{1,3}$ and $M_{1,4}$ versus d with various t

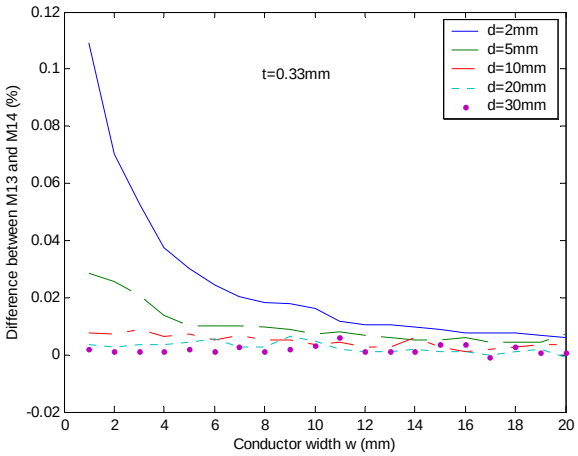

(b) Difference between $M_{1,3}$ and $M_{1,4}$ versus w with various d

Figure 2-27: Difference between $M_{1,3}$ and $M_{1,4}$ as a function of t, d and w.

This simulation actually covers the worst case because the difference should be even less if a magnetic core is used. This justifies the modeling of a spiral winding transmission line structure as a linear cascaded transmission structures. A practical integrated passive structure is shown in Figure 2-28(a), the equivalent unwound cascaded transmission structure is given in Figure 2-28(b).

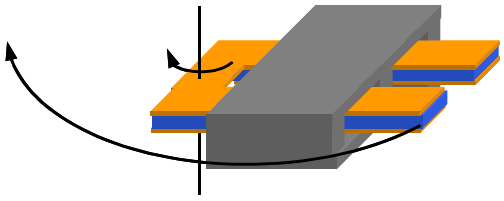

(a) A practical integrated passives structure

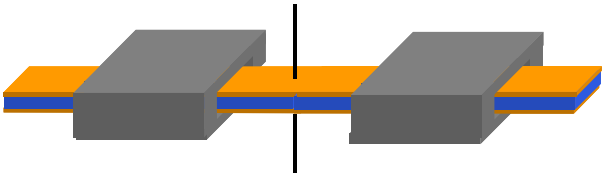

(b) The equivalent cascaded transmission line model

Figure 2-28: A spiral winding integrated passives module and its equivalent model.

Therefore, the investigation on some applicable structures such as cascaded generalized transmission structures becomes necessary. Figure 2-29 shows a series resonant cascaded generalized transmission structures with n sections and each section may have different parameters and length.

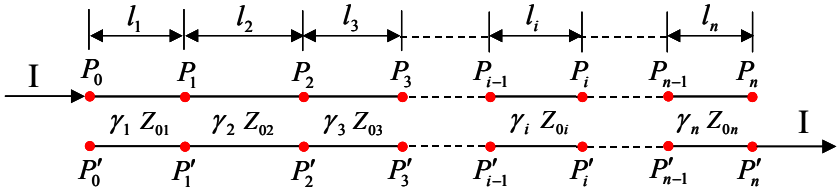

Figure 2-29: Cascaded generalized transmission lines.

The voltage and current at the boundary of each two cascaded transmission structures must be continuous. Therefore, we have

$$\begin{cases} V_{P_1P_1'} = V_{a1}e^{-\gamma_1 l_1} + V_{b1}e^{\gamma_1 l_1} = V_{a2} + V_{b2} \\ V_{P_2P_2'} = V_{a2}e^{-\gamma_2 l_2} + V_{b2}e^{\gamma_2 l_2} = V_{a3} + V_{b3} \\ \vdots \\ V_{P_{n-1}P_{n-1}'} = V_{a(n-1)}e^{-\gamma_{n-1} l_{n-1}} + V_{b(n-1)}e^{\gamma_{n-1} l_{n-1}} = V_{an} + V_{bn} \end{cases} \tag{2-48}$$

$$\begin{cases} I_{DM}(0) = \dfrac{V_{a1}}{Z_{01}} - \dfrac{V_{b1}}{Z_{01}} = \dfrac{I}{2} \\ I_{DM}(l_1) = \dfrac{V_{a1}}{Z_{01}}e^{-\gamma_1 l_1} - \dfrac{V_{b1}}{Z_{01}}e^{\gamma_1 l_1} = \dfrac{V_{a2}}{Z_{02}} - \dfrac{V_{b2}}{Z_{02}} \\ I_{DM}(l_1 + l_2) = \dfrac{V_{a2}}{Z_{02}}e^{-\gamma_2 l_2} - \dfrac{V_{b2}}{Z_{02}}e^{\gamma_2 l_2} = \dfrac{V_{a3}}{Z_{03}} - \dfrac{V_{b3}}{Z_{03}} \\ \vdots \\ I_{DM}(l_1 + l_2 + \cdots + l_{n-1}) = \dfrac{V_{a(n-1)}}{Z_{0(n-1)}}e^{-\gamma_{n-1} l_{n-1}} - \dfrac{V_{b(n-1)}}{Z_{0(n-1)}}e^{\gamma_{n-1} l_{n-1}} = \dfrac{V_{an}}{Z_{0n}} - \dfrac{V_{bn}}{Z_{0n}} \\ I_{DM}(l_1 + l_2 + \cdots + l_{n-1} + l_n) = \dfrac{V_{an}}{Z_{0n}}e^{-\gamma_n l_n} - \dfrac{V_{bn}}{Z_{0n}}e^{\gamma_n l_n} = \dfrac{-I}{2} \end{cases} \tag{2-49}$$

From the equations above, we obtain

$$\begin{cases} V_{a1} = F_{a1}V_{a1} + G_{a1}V_{b1} = F'_{a1}V_{a1} + G'_{a1}V_{b1} \\ V_{b1} = F_{b1}V_{a1} + G_{b1}V_{b1} = F'_{b1}V_{a1} + G'_{b1}V_{b1} \\ V_{a2} = F_{a2}V_{a1} + G_{a2}V_{b1} = F'_{a2}V_{a1} + G'_{a2}V_{b1} \\ V_{b2} = F_{b2}V_{a1} + G_{b2}V_{b1} = F'_{b2}V_{a1} + G'_{b2}V_{b1} \\ V_{a3} = F_{a3}V_{a2} + G_{a3}V_{b2} = F'_{a3}V_{a1} + G'_{a3}V_{b1} \\ V_{b3} = F_{b3}V_{a2} + G_{b3}V_{b2} = F'_{b3}V_{a1} + G'_{b3}V_{b1} \\ \qquad\qquad \vdots \\ V_{an} = F_{an}V_{a(n-1)} + G_{an}V_{b(n-1)} = F'_{an}V_{a1} + G'_{an}V_{b1} \\ V_{bn} = F_{bn}V_{a(n-1)} + G_{bn}V_{b(n-1)} = F'_{bn}V_{a1} + G'_{bn}V_{b1} \end{cases} \tag{2-50}$$

in which,

$$\begin{cases} F_{a1} = F'_{a1} = 1 \\ G_{a1} = G'_{a1} = 0 \\ F_{b1} = F'_{b1} = 0 \\ G_{b1} = G'_{b1} = 1 \end{cases} \tag{2-51}$$

$$\begin{cases} F'_{ai} = F'_{a(i-1)}F_{ai} + F'_{b(i-1)}G_{ai} \\ G'_{ai} = G'_{a(i-1)}F_{ai} + G'_{b(i-1)}G_{ai} \\ F'_{bi} = F'_{a(i-1)}F_{bi} + F'_{b(i-1)}G_{bi} \\ G'_{bi} = G'_{a(i-1)}F_{bi} + G'_{b(i-1)}G_{bi} \end{cases} \quad (i = 2,3,4\ldots n) \tag{2-52}$$

Thus all the equations can be presented as

$$\begin{cases} \dfrac{V_{a1}}{Z_{01}} - \dfrac{V_{b1}}{Z_{01}} = \dfrac{I}{2} \\ \dfrac{V_{an}}{Z_{0n}}e^{-\gamma_n l_n} - \dfrac{V_{bn}}{Z_{0n}}e^{\gamma_n l_n} = \dfrac{-I}{2} \\ V_{an} = F'_{an}V_{a1} + G'_{an}V_{b1} \\ V_{bn} = F'_{bn}V_{a1} + G'_{bn}V_{b1} \end{cases} \tag{2-53}$$

Seeking solutions to (2-53), we obtain

$$\begin{cases} V_{an} = V_{bn}e^{2\gamma_n l_n} - \dfrac{IZ_{0n}e^{\gamma_n l_n}}{2} \\ V_{bn} = \dfrac{I}{2}\dfrac{Z_{0n}(F'_{bn} + G'_{bn})e^{\gamma_n l_n} + Z_{01}(F'_{an}G'_{bn} - F'_{bn}G'_{an})}{(F'_{bn} + G'_{bn})e^{2\gamma_n l_n} - (F'_{an} + G'_{an})} = IZ_{bn} \end{cases} \tag{2-54}$$

Therefore,

$$\begin{aligned} V_{P_0P'_n} &= V_{P_0P_n} + V_{P_nP'_n} \\ &= I\left(\sum_{i=1}^{n}\frac{R_i + j\omega(L_i + M_i)}{2}l_i\right) + \sum_{i=1}^{n}\frac{1}{2}[V_{ai}(1 - e^{-\gamma_i l_i}) + V_{bi}(1 - e^{\gamma_i l_i})] + V_{an}e^{-\gamma_n l_n} + V_{bn}e^{\gamma_n l_n} \\ &= I\left(\sum_{i=1}^{n}\frac{R_i + j\omega(L_i + M_i)}{2}l_i\right) + \sum_{i=1}^{n}\frac{1}{2}[V_{ai}(1 - e^{-\gamma_i l_i}) + V_{bi}(1 - e^{\gamma_i l_i})] + 2V_{bn}e^{\gamma_n l_n} - \frac{IZ_{0n}}{2} \end{aligned} \tag{2-55}$$

The impedance across P_0 and P'_n

$$Z_{P_0P_n'} = \frac{V_{P_0P_n'}}{I} = \sum_{i=1}^{n} \frac{R_i + j\omega(L_i + M_i)}{2} l_i + \sum_{i=1}^{n} \frac{1}{2I}[V_{ai}(1 - e^{-\gamma_i l_i}) + V_{bi}(1 - e^{\gamma_i l_i})] + \frac{2V_{bn}}{I} e^{\gamma_n l_n} - \frac{Z_{0n}}{2} \quad (2\text{-}56)$$

As a series resonator with the same total inductance and capacitance, the impedances of a single generalized transmission structure and a cascaded generalized transmission structure are compared in Figure 2-30. The chief difference is the higher frequency characteristics which are not so critical provided a good magnetic coupling between top and bottom conductors is achieved.

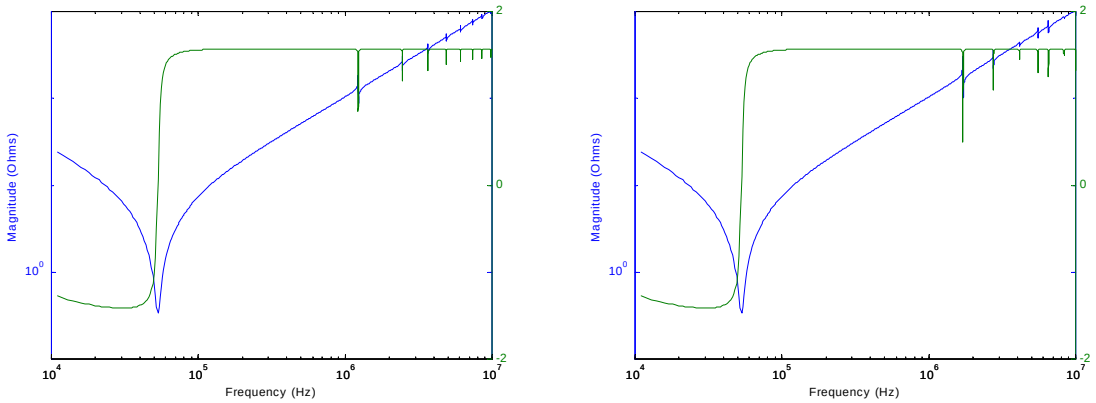

(a) A single generalized transmission line (b) Cascaded generalized transmission lines

Figure 2-30: Typical impedance characteristics of a series resonator.

2.6. Case Study

A transmission structure prototype has been constructed from copper plated ceramic dielectric substrate. In order not to import complex high frequency material characteristics, no magnetic core is used in this prototype and the dimension have been chosen to show resonance in the sub-MHz region. The picture of the prototype is shown in Figure 2-31. Some technical parameters are given in Table 2-4. It is realized that this experimental structure does not approach the high power density and other favorable practical characteristics of this class of integrated electromagnetic power passives as already illustrated [18].

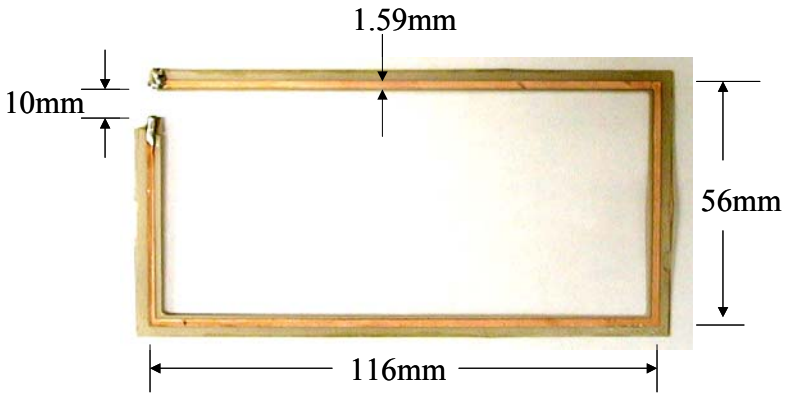

Figure 2-31: Picture and dimensions of the transmission line prototype.

Table 2-4: Technical parameters for the transmission structure prototype

Dielectric material	$BaTiO_3$ (Y5V)_
ε_r of the dielectric material	14000 (nominal)
Thickness of the ceramic tile	0.33mm
tanδ of the dielectric material	<1%
Copper thickness	≈2mil
Inductance per unit length L	879nH/m
Capacitance per unit length C	673nF/m
Mutual inductance per unit length M	782nH/m
Total length of the transmission line	328mm

The MATLAB calculation results and impedance analyzer measurement results of Z_{AD} without load are shown in Figure 2-32(a) and (b), respectively.

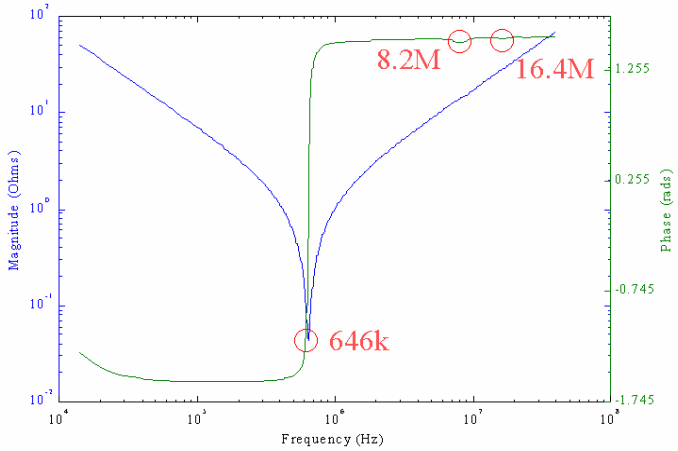

(a) Matlab calculation results

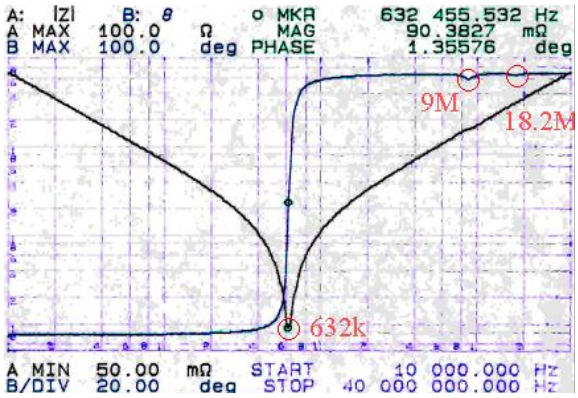

(b) Impedance analyzer measurement results

Figure 2-32: Calculation results and measurement results of Z_{AD} without load.

The Matlab calculation results and impedance analyzer measurement results of Z_{AC} are shown in Figure 2-33(a) and (b), respectively.

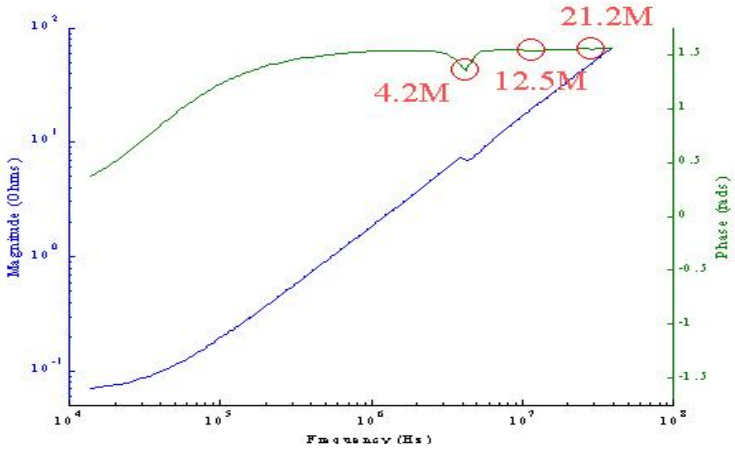

(a) MATLAB calculation results

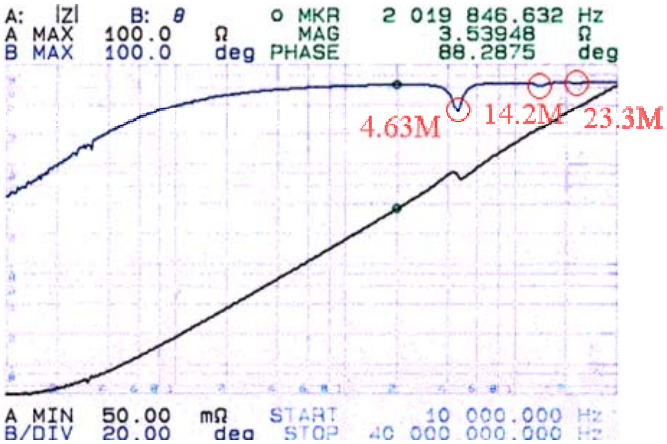

(b) Impedance analyzer measurement results

Figure 2-33: Calculation results and measurement results of Z_{AC}.

From Figure 2-32 and Figure 2-33, the calculation results correlate the measurement results well. The error is about 10%.

Figure 2-34(a) shows the measurement results of Z_{AB} without load. However, it looks different from the calculation results shown in Figure 2-34(b) since the lead inductance connected to the impedance analyzer has been neglected. Assuming a lead inductance of 20nH, the calculation results are shown in Figure 2-34(c) which correlates the measurement results well.

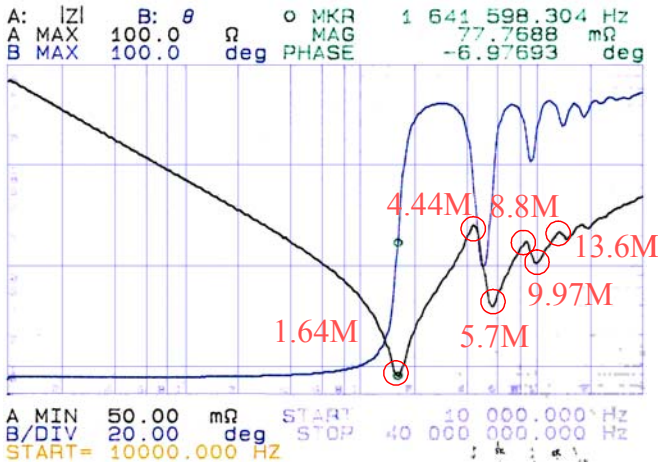

a) Impedance analyzer measurement results

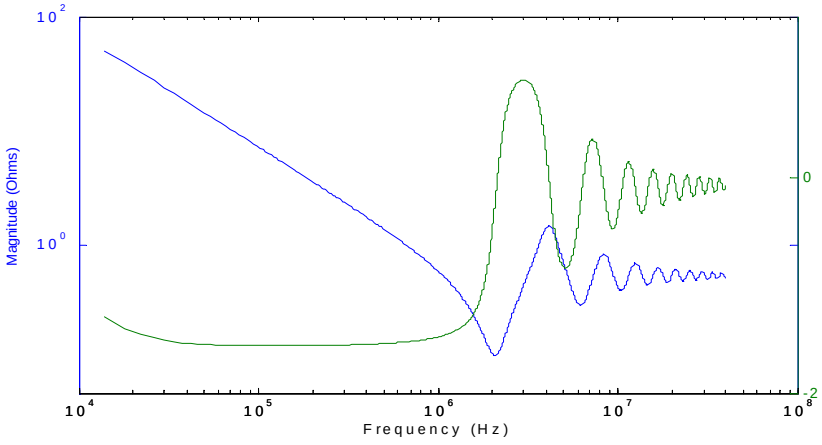

(b) MATLAB calculation results without considering lead inductance

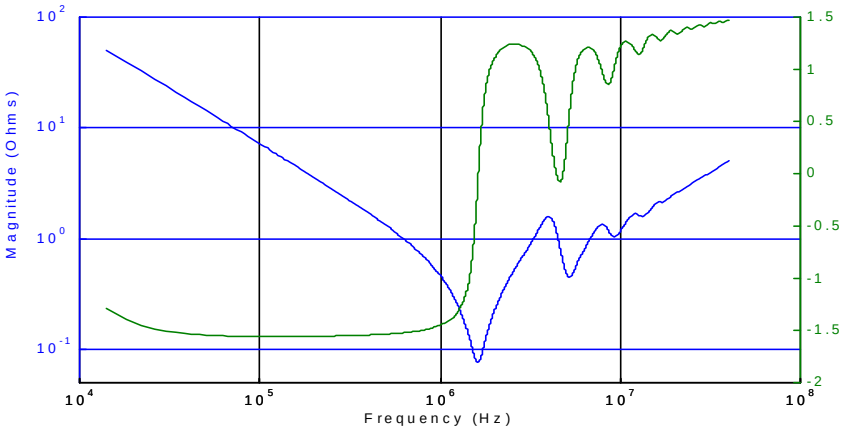

(c) MATLAB calculation results assuming 20nH lead inductance

Figure 2-34: Calculation results and measurement results of Z_{AB}.

2.7. *Discussion*

An interesting phenomenon of an inversely balanced series resonant transmission structure has been noticed: The high frequency resonant peaks occur when the structure length equals to i (i=1,2,3,…) times of the wavelength while the fundamental resonance has no obvious relationship with the wavelength, as shown in Figure 2-35. However, a typical impedance of a classical series resonant transmission line has repetitive valleys and peaks every λ/4, as shown in Figure 2-22.

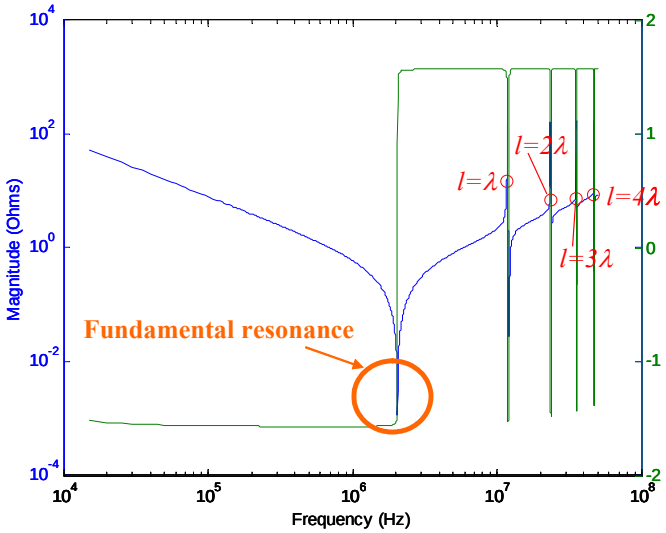

Figure 2-35: Typical impedance of an inversely balanced series resonant transmission structure.

To fully understand this difference, an insight to the current patterns is again the key. As discussed in section 2.1, the currents of a conventional transmission line are balanced. However, $I_1(x,t)$ may not equal $-I_2(x,t)$ in a generalized transmission structure. Instead, the currents on the top and bottom conductors can be obtained from (2-13) as

$$\begin{cases} I_1(x) = \dfrac{I + I_{ZL}}{2} + I_{DM}(x) = I_{CM}(x) + I_{DM}(x) = I_{1_CM}(x) + I_{1_DM}(x) \\ I_2(x) = \dfrac{I + I_{ZL}}{2} - I_{DM}(x) = I_{CM}(x) - I_{DM}(x) = I_{2_CM}(x) + I_{2_DM}(x) \end{cases} \tag{2-57}$$

The current on each conductor consists of two parts: common mode current I_{CM} and differential mode current I_{DM}. The common mode currents on the two conductors are exactly the same while the differential mode currents are same in magnitude but opposite in direction. For example, the current distributions of a series resonant transmission structure shown in Figure 2-13 at low frequency are shown in Figure 2-36. The common mode and differential mode equivalent circuits are shown in Figure 2-37(a) and (b), respectively.

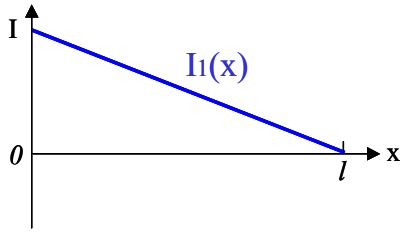

(a) The total current on the top conductor

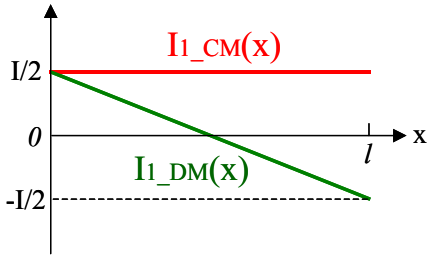

(b) The common mode and differential mode currents on the top conductor

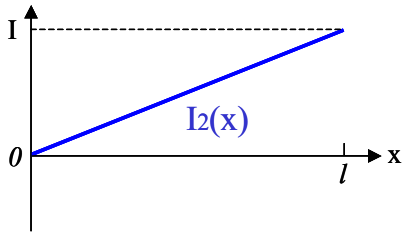

(c) The total current on the bottom conductor

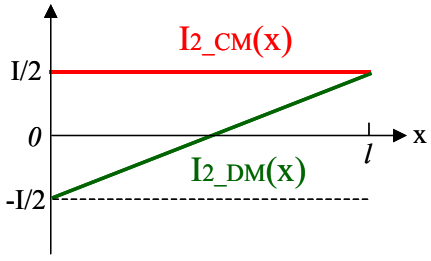

(d) The common mode and differential mode currents on the bottom conductor

Figure 2-36: Current distributions at low frequency.

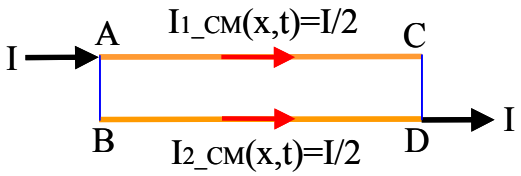

(a) The common mode currents

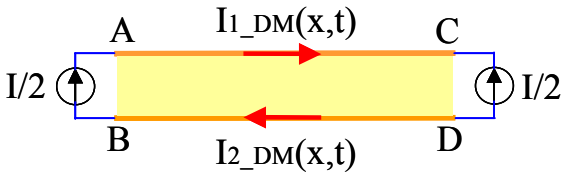

(b) The differential mode currents

Figure 2-37: The common mode and differential mode currents on the top and bottom conductors.

From Figure 2-37(a), the voltage generated by the common mode currents is given by

$$V_{AD_CM} = \frac{I}{2}[R + j\omega(L+M)]l \tag{2-58}$$

From Figure 2-37(b), the voltage generated by the differential mode currents is given by

$$V_{AD_DM} = \frac{I}{2}Z_0\left[\frac{1}{\sinh(\gamma l)} + \frac{1}{\tanh(\gamma l)}\right] \tag{2-59}$$

According to basic circuit theory, the total voltage across A and D equals the sum of the voltage generated by the common mode and differential mode currents separately, or

$$V_{AD} = V_{AD_CM} + V_{AD_DM} = \frac{I}{2}[R + j\omega(L+M)]l + \frac{I}{2}Z_0\left[\frac{1}{\sinh(\gamma l)} + \frac{1}{\tanh(\gamma l)}\right] \tag{2-60}$$

Therefore, the impedance of Z_{AD} is given by

$$Z_{AD} = \frac{V_{AD}}{I} = \frac{R + j\omega(L+M)}{2}l + \frac{Z_0}{2}\left[\frac{1}{\sinh(\gamma l)} + \frac{1}{\tanh(\gamma l)}\right] \tag{2-61}$$

It is evident that these are the same as equation (2-23).

The common mode currents are evenly distributed in the two conductors, each equals half of the total input current. The differential mode currents are actually internal balanced currents that cause the high frequency conventional transmission line effects. The fundamental series resonant frequency shows the resonance between the inductance

(L+M)l/2 which is seen by the common mode current and the capacitance which is seen by the differential mode current.

The wavelength, from (2-10), is given by

$$\lambda = \frac{1}{f\sqrt{2(L-M)C}} \tag{2-62}$$

From (2-24), the equivalent series resonant inductance is approximately

$$f_0 = \frac{1}{2\pi l\sqrt{(L+M)C/2}} \tag{2-63}$$

Provided the same series resonant frequency, the higher frequency peaks cannot be pushed up to a higher frequency by reducing C because the structure length has to be increased by the same value while the wavelength becomes larger. The only method may be reducing the value of (L-M), or making a better magnetic coupling between the conductors.

The input impedance of a conventional transmission line, as shown in Figure 2-22, also has series resonance characteristics. The key differences between these two methods are:

(1) The generalized transmission line as Figure 2-13 utilizes almost the total inductance of the structure as the resonant inductance while the conventional transmission structure just utilizes the leakage inductances. Because the leakage inductance is generally much lower than the self-inductances and it causes high frequency oscillations, the conventional transmission line structure may not be suitable for power integrated series resonators.

(2) The resonance of a conventional transmission line occur periodically when the structure length equals integer multiples of λ/4. Therefore, the distance from the first series resonant frequency and the first parallel resonant frequency is out of adjustment. In terms of a series resonant transmission structure shown in Figure 2-13, since the causes of the fundamental series resonance and the high frequency resonance are different, it is possible to minimize the high frequency resonance peaks while keeping the fundamental series resonant frequency fixed. This is another advantage over the conventional series resonant transmission line.

2.8. Conclusion

An L-C cell is a basic building block of integrated passives such as an integrated series resonator. However, the well-known conventional transmission line equivalent circuit as well as the equations are not applicable for the unbalanced current in an integrated passive module. This chapter presents a generalized transmission structure theory that applies to both balanced and unbalanced current. The conventional transmission line is just a special case when $I_1(x,t)=-I_2(x,t)$.

The impedances of a generalized transmission structure with various loads and interconnections have been studied. An open-circuited load and a short-circuited load lead to series resonance and parallel resonance, respectively. In addition, this theory has been extended to cascaded structure. The equations are substantiated with experimental results. Some preliminary study indicates the advantages of this unbalanced current passives integration technique. Since the existing integrated passive components are no other than some combination of this generalized transmission line primitive, the theoretical analysis may be applied to the further modeling of all integrated passive components.

Chapter 3: Multi-conductor Generalized Transmission Structure

3.1. Introduction

A realistic integrated passive module is far from a simple two-conductor transmission structure due to the magnetic and capacitive coupling between sections of the windings, as illustrated in Figure 3-1. Therefore, the model presented in Chapter 2 is not sufficient to model a practical integrated passives structure which can be clearly seen from the significant difference between the model and the measurement results, as shown in Figure 3-2.

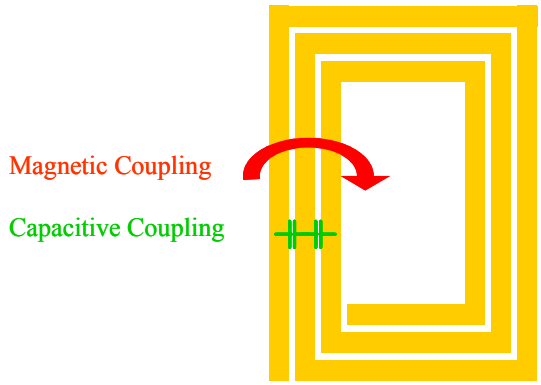

Figure 3-1: Magnetic and capacitive coupling between sections of windings (top view, spiral winding structure)

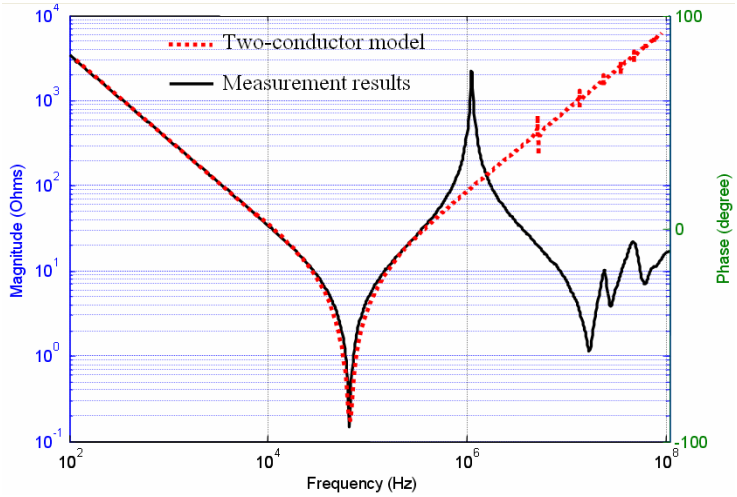

Figure 3-2: Discrepancies between the two-conductor model and the measurement results of an integrated series resonator.

A typical ISRM structure is shown in Figure 3-3(a). With high permittivity dielectric ceramic substrate in between, the top conductor is in solid line and the bottom conductor is in dashed line. Taking a cross-sectional view into the structure, a building block with coplanar conductor on both sides of a dielectric substrate can be obtained, as shown in Figure 3-3(b). As a further step to model any practical integrated passive components, this chapter presents the extension of the generalized transmission structure theory developed for the two-conductor approach. The developed multi-conductor transmission structure theory will be applied to the modeling of integrated power passives with various structures.

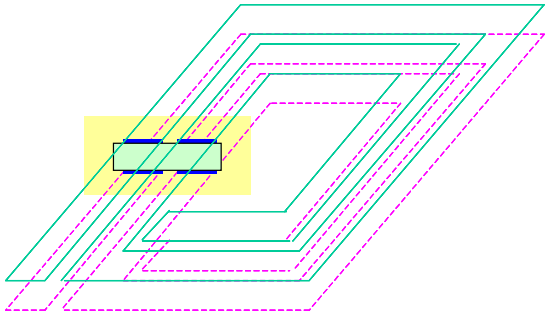

(a) A building block of an ISRM structure

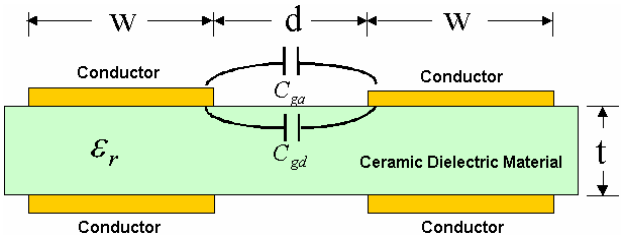

(b) The cross-sectional view

Figure 3-3: The cross-sectional view of a building block of an ISRM structure.

3.2. Coplanar Structure Capacitance Calculation

In the modeling of the basic building block structure shown in Figure 3-3(b), the determination of the capacitive coupling between conductors is one of the key issues. The capacitance per unit length between a top conductor and its corresponding bottom conductor can be easily obtained using equation $C=\varepsilon_0\varepsilon_r w/t$. However, the capacitance

between two adjacent conductors on the same side of a dielectric substrate is still to be calculated.

The total inter-electrode capacitance per unit length is considered as the sum of the capacitance in the upper region (air) C_{ga} and the capacitance in the lower region (dielectric) C_{gd}, as shown in Figure 3-3(b). Since the relative dielectric constant of the substrate is assumed very large (typically >80) compared to that of the surrounding medium, all of the flux is considered confined to the dielectric while the fringing capacitance can be neglected [28]. A Schwarz-Christoffel transformation is used to map the Z plane of Figure 3-4(a) onto the ω plane of Figure 3-4(b). An inverse Schwarz-Christoffel transformation is then used to map the ω plane of Figure 3-4(b) onto the ζ plane of Figure 3-4(c). The dielectric region shown shaded in the Z plane maps onto the shaded regions in the ω and ζ planes. Thus, the capacitance calculation is reduced to the elementary calculation of the capacitance of parallel plates.

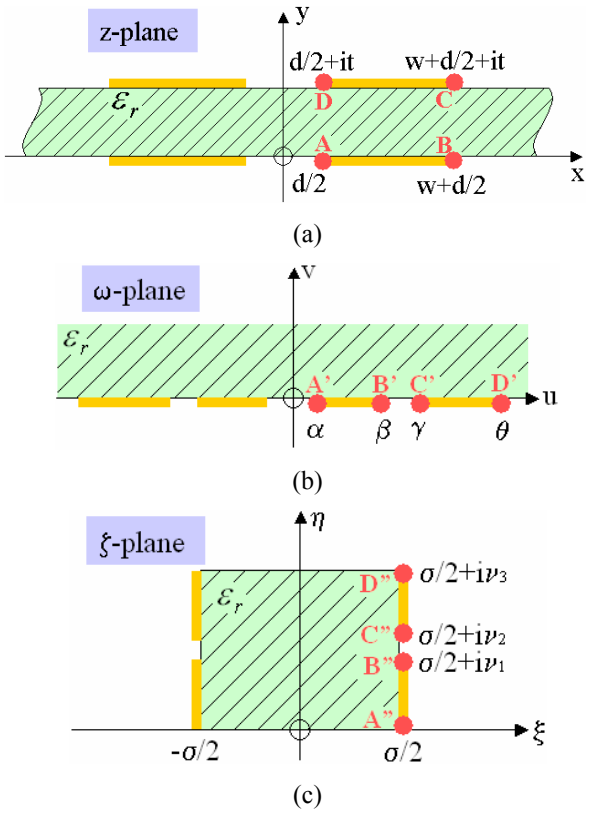

Figure 3-4: Schwarz-Christoffel transformation.

The mapping relating the Z and ω planes is readily obtained by the method of Schwarz-Christoffel as

$$\omega = \frac{\pi}{2t}\tanh\frac{\pi z}{2t} \tag{3-1}$$

so that,

$$\alpha = \frac{\pi}{2t}\tanh\frac{\pi d}{4t} \tag{3-2}$$

$$\beta = \frac{\pi}{2t}\tanh\frac{\pi(w+d/2)}{2t} \tag{3-3}$$

$$\gamma = \frac{\pi}{2t}\frac{1}{\tanh\frac{\pi(w+d/2)}{2t}} \tag{3-4}$$

$$\theta = \frac{\pi}{2t}\frac{1}{\tanh\frac{\pi d}{4t}} \tag{3-5}$$

Similarly, the transformation relating the ζ and ω planes is

$$\zeta = \int_0^{\omega}\frac{d\omega}{\sqrt{(\omega^2-\alpha^2)(\omega^2-\theta^2)}} \tag{3-6}$$

According to [29][30][31], it is obtained that

$$\nu_1 = \nu_3 - \nu_2 = \int_{\gamma}^{\theta}\frac{d\omega}{\sqrt{(\omega^2-\alpha^2)(\theta^2-\omega^2)}} = \frac{1}{\theta}dn^{-1}\left(\frac{\gamma}{\theta},k_2'\right) = \frac{1}{\theta}F\left(\sin^{-1}\sqrt{\frac{\theta^2-\gamma^2}{\theta^2-\alpha^2}},k_2'\right) \tag{3-7}$$

$$\sigma = \int_0^{\alpha}\frac{2d\omega}{\sqrt{(\omega^2-\alpha^2)(\omega^2-\theta^2)}} = \frac{2}{\theta}K(k_2) \tag{3-8}$$

in which,

$F(\phi,k_2)$ = the incomplete elliptic integral of the first kind for the argument ϕ and modulus k_2.

$F(\phi,k_2')$ = complement of $F(\phi,k_2)$

$$k_2 = \frac{\alpha}{\theta} \tag{3-9}$$

$$k_2' = \sqrt{1-k_2^2} \tag{3-10}$$

$K(k_2)$ = the complete elliptic integral of the first kind

From above equations and Figure 3-4(c), it is obtained that

$$C_{gd} = \varepsilon_0 \varepsilon_r \frac{v_1}{\sigma} \text{ (F/m)} \tag{3-11}$$

Table 3-1 demonstrates three prototypes of this symmetric coplanar structure, each with different parameters. The calculation results correlate well with the measured results, with only less than 3% error.

Table 3-1: Inter-electrode capacitance calculation examples

Pictures	Parameters	Calculation results	Measured results
	w=100mil d=20mil l=27.8mm t=0.33mm ε_r=14000	C=881pF	C=860pF
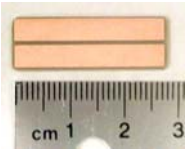	w=156mil d=30mil l=27.8mm t=0.33mm ε_r=14000	C=627PF	C=610pF
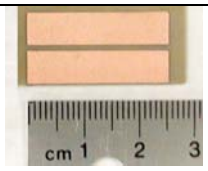	w=225mil d=39.5mil l=25.8mm t=0.33mm ε_r=14000	C=461pF	C=468pF

The normalized capacitance per unit length of the structure shown in Figure 3-3(b) is plotted as a function of d, w and t in Figure 3-5. From Figure 3-5, C_{gd} drops dramatically with an increasing d and increases with t. However, the value of C_{gd} is not sensitive to the variation of the conductor width w, as illustrated in Figure 3-5(a). Therefore, a large spacing between winding turns rather than a smaller conductor width can really help to reduce the inter-winding capacitance.

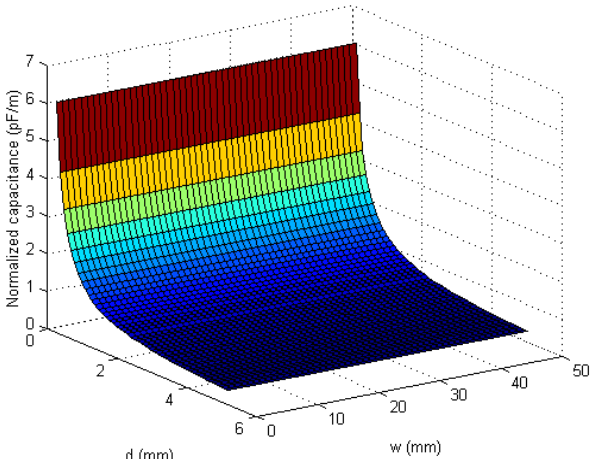

(a) Normalized capacitance versus d and w when t=0.33mm.

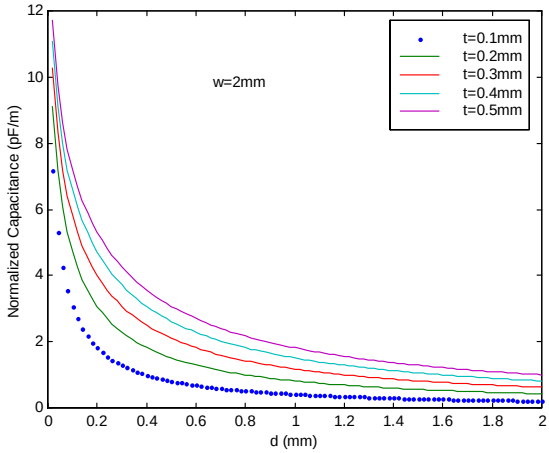

(b) Normalized capacitance versus d with various t when w=2mm

Figure 3-5: Normalized C_{gd} as a function of d, w and t.

3.3. Formulation of Generalized Multi-conductor Transmission Structure

Let us consider the n-cell integrated passives structure depicted in Figure 3-6, comprising 2n parallel conductors. The whole structure with a length *l* is supposed to be uniform along the longitudinal x axis.

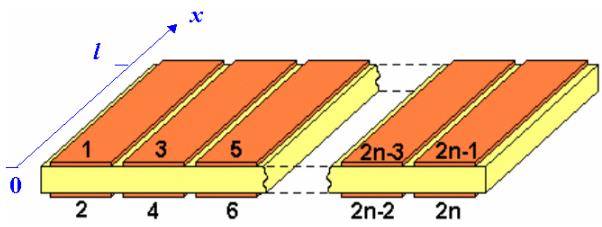

Figure 3-6: An n-cell integrated passives structure.

Neglecting the losses for clarity of presentation, the equivalent circuit of the structure is shown in Figure 3-7.

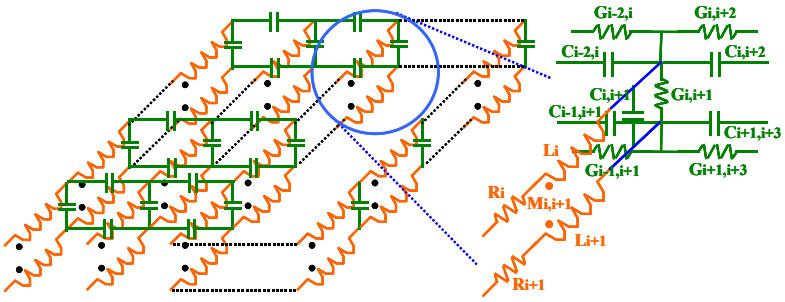

Figure 3-7: The lossless distributed equivalent circuit of the structure in Figure 3-4.

Apparently, the modeling should be based on matrix representation due to the magnetic and capacitive coupling between more than two conductors. Taking the basic circuit equations and using the phasor representation, the basic voltage and current equations can be obtained. $V_i(x)$ and $I_i(x)$ (i=1,2,3,…,2n) represent the voltage and current on the i^{th} conductor, respectively.

The conductor voltages

$$\begin{cases} -\dfrac{d}{dx}V_1(x) = (R_1 + j\omega L_1)I_1(x) + \sum_{i=2}^{2n} j\omega M_{1,i} I_i(x) \\ -\dfrac{d}{dx}V_2(x) = j\omega M_{2,1} I_1(x) + (R_2 + j\omega L_2)I_2(x) + \sum_{i=3}^{2n} j\omega M_{2,i} I_i(x) \\ -\dfrac{d}{dx}V_3(x) = \sum_{i=1}^{2} j\omega M_{3,i} I_i(x) + (R_3 + j\omega L_3)I_3(x) + \sum_{i=4}^{2n} j\omega M_{3,i} I_i(x) \\ -\dfrac{d}{dx}V_4(x) = \sum_{i=1}^{3} j\omega M_{4,i} I_i(x) + (R_4 + j\omega L_4)I_4(x) + \sum_{i=5}^{2n} j\omega M_{4,i} I_i(x) \\ \vdots \\ -\dfrac{d}{dx}V_{2n}(x) = \sum_{i=1}^{2n-1} j\omega M_{2n,i} I_i(x) + (R_{2n} + j\omega L_{2n})I_{2n}(x) \end{cases} \tag{3-12}$$

The current flowing through each conductor

$$\begin{cases} -\dfrac{d}{dx}I_1(x) = (G_{1,2} + j\omega C_{1,2} + G_{1,3} + j\omega C_{1,3})V_1(x) - (G_{1,2} + j\omega C_{1,2})V_2(x) - (G_{1,3} + j\omega C_{1,3})V_3(x) \\ -\dfrac{d}{dx}I_2(x) = -(G_{1,2} + j\omega C_{1,2})V_1(x) + (G_{1,2} + j\omega C_{1,2} + G_{2,4} + j\omega C_{2,4})V_2(x) - (G_{2,4} + j\omega C_{2,4})V_4(x) \\ -\dfrac{d}{dx}I_3(x) = -(G_{1,3} + j\omega C_{1,3})V_1(x) + (G_{1,3} + j\omega C_{1,3} + G_{3,4} + j\omega C_{3,4} + G_{3,5} + j\omega C_{3,5})V_3(x) - (G_{3,4} + j\omega C_{3,4})V_4(x) - (G_{3,5} + j\omega C_{3,5})V_5(x) \\ -\dfrac{d}{dx}I_4(x) = -(G_{2,4} + j\omega C_{2,4})V_2(x) - (G_{3,4} + j\omega C_{3,4})V_3(x) + (G_{2,4} + j\omega C_{2,4} + G_{3,4} + j\omega C_{3,4} + G_{4,6} + j\omega C_{4,6})V_4(x) - (G_{4,6} + j\omega C_{4,6})V_6(x) \\ \vdots \\ -\dfrac{d}{dx}I_{2n-1}(x) = -(G_{2n-3,2n-1} + j\omega C_{2n-3,2n-1})V_{2n-3}(x) + (G_{2n-3,2n-1} + j\omega C_{2n-3,2n-1} + G_{2n-1,2n} + j\omega C_{2n-1,2n})V_{2n-1}(x) - (G_{2n-1,2n} + j\omega C_{2n-1,2n})V_{2n}(x) \\ -\dfrac{d}{dx}I_{2n}(x) = -(G_{2n-2,2n} + j\omega C_{2n-2,2n})V_{2n-2}(x) - (G_{2n-1,2n} + j\omega C_{2n-1,2n})V_{2n-1}(x) + (G_{2n-2,2n} + j\omega C_{2n-2,2n} + G_{2n-1,2n} + j\omega C_{2n-1,2n})V_{2n}(x) \end{cases} \tag{3-13}$$

in which the calculation of the co-planar inter-electrode capacitance $C_{i,i+2}$ (i=1,2,3,…,2n-2) has been given in section 3.2.

Presenting in a matrix form, we have

$$\begin{cases} -\dfrac{d}{dx}\mathbf{V} = \mathbf{ZI} \\ -\dfrac{d}{dx}\mathbf{I} = \mathbf{YV} \end{cases} \tag{3-14}$$

in which,

$$\mathbf{Z} = \begin{bmatrix} R_1 + j\omega L_1 & j\omega M_{1,2} & j\omega M_{1,3} & j\omega M_{1,4} & \cdots & j\omega M_{1,2n-1} & j\omega M_{1,2n} \\ j\omega M_{2,1} & R_2 + j\omega L_2 & j\omega M_{2,3} & j\omega M_{2,4} & \cdots & j\omega M_{2,2n-1} & j\omega M_{2,2n} \\ j\omega M_{3,1} & j\omega M_{3,2} & R_3 + j\omega L_3 & j\omega M_{3,4} & \cdots & j\omega M_{3,2n-1} & j\omega M_{3,2n} \\ j\omega M_{4,1} & j\omega M_{4,2} & j\omega M_{4,3} & R_4 + j\omega L_4 & \cdots & j\omega M_{4,2n-1} & j\omega M_{4,2n} \\ \vdots & \vdots & \vdots & \vdots & \ddots & \vdots & \vdots \\ j\omega M_{2n-1,1} & j\omega M_{2n-1,2} & j\omega M_{2n-1,3} & j\omega M_{2n-1,4} & \cdots & R_{2n-1} + j\omega L_{2n-1} & j\omega M_{2n-1,2n} \\ j\omega M_{2n,1} & j\omega M_{2n,2} & j\omega M_{2n,3} & j\omega M_{2n,4} & \cdots & j\omega M_{2n,2n-1} & R_{2n} + j\omega L_{2n} \end{bmatrix} \tag{3-15}$$

$$Y = \begin{bmatrix} G_{1,2} + j\omega C_{1,2} + G_{1,3} + j\omega C_{1,3} & -(G_{1,2} + j\omega C_{1,2}) & -(G_{1,3} + j\omega C_{1,3}) & 0 & \cdots & 0 \\ -(G_{1,2} + j\omega C_{1,2}) & G_{1,2} + j\omega C_{1,2} + G_{2,4} + j\omega C_{2,4} & 0 & -(G_{2,4} + j\omega C_{2,4}) & \cdots & 0 \\ -(G_{1,3} + j\omega C_{1,3}) & 0 & G_{1,3} + j\omega C_{1,3} + G_{3,4} + j\omega C_{3,4} + G_{3,5} + j\omega C_{3,5} & -(G_{3,4} + j\omega C_{3,4}) & \cdots & 0 \\ 0 & -(G_{2,4} + j\omega C_{2,4}) & -(G_{3,4} + j\omega C_{3,4}) & G_{2,4} + j\omega C_{2,4} + G_{3,4} + j\omega C_{3,4} + G_{4,6} + j\omega C_{4,6} & \cdots & 0 \\ \vdots & \vdots & \vdots & \vdots & \ddots & \vdots \\ 0 & 0 & 0 & 0 & \cdots & G_{2n-2,2n} + j\omega C_{2n-2,2n} + G_{2n-1,2n} + j\omega C_{2n-1,2n} \end{bmatrix} \tag{3-16}$$

$$\mathbf{V} = \begin{bmatrix} V_1 & V_2 & V_3 & V_4 & \cdots & V_{2n-1} & V_{2n} \end{bmatrix}^T \tag{3-17}$$

$$\mathbf{I} = \begin{bmatrix} I_1 & I_2 & I_3 & I_4 & \cdots & I_{2n-1} & I_{2n} \end{bmatrix}^T \tag{3-18}$$

Two sets of coupled wave equations can be obtained from (3-14) by variables elimination.

$$\begin{cases} -\dfrac{d^2}{dx^2}\mathbf{V} = \mathbf{ZYV} \\ -\dfrac{d^2}{dx^2}\mathbf{I} = \mathbf{YZI} \end{cases} \tag{3-19}$$

For the purpose of decoupling the equations, a transformation matrix **T** is introduced relating real voltage **V** to modal voltage $\hat{\mathbf{V}}$ [32] such that

$$\mathbf{V} = \mathbf{T}\hat{\mathbf{V}} \tag{3-20}$$

Similarly,

$$\mathbf{I} = \mathbf{W}\hat{\mathbf{I}} \tag{3-21}$$

Substituting (3-20)(3-21) into (3-19), it yields

$$\begin{cases} \dfrac{d^2}{dx^2}\hat{\mathbf{V}} = (\mathbf{T}^{-1}\mathbf{ZYT})\hat{\mathbf{V}} \\ \dfrac{d^2}{dx^2}\hat{\mathbf{I}} = (\mathbf{W}^{-1}\mathbf{YZW})\hat{\mathbf{I}} \end{cases} \tag{3-22}$$

We must find that

$$\mathbf{T}^{-1}\mathbf{ZYT} = \mathbf{W}^{-1}\mathbf{YZW} = \gamma^2 = diag\{\gamma_1^2, \gamma_2^2, \gamma_3^2, \gamma_4^2, \cdots, \gamma_{2n}^2\} \tag{3-23}$$

T is composed of 2n linearly independent eigenvectors of **ZY** and **W** is composed of 2n linearly independent eigenvectors of **YZ**.

After decoupling, each row of (3-22) is in the standard form of a transmission line equation. Seeking solutions to (3-22), it can be found out that

$$\begin{cases} \hat{V}_1(x) = \hat{V}_{1(a)}e^{-\gamma_1 x} + \hat{V}_{1(b)}e^{\gamma_1 x} \\ \hat{V}_2(x) = \hat{V}_{2(a)}e^{-\gamma_2 x} + \hat{V}_{2(b)}e^{\gamma_2 x} \\ \hat{V}_3(x) = \hat{V}_{3(a)}e^{-\gamma_3 x} + \hat{V}_{3(b)}e^{\gamma_3 x} \\ \hat{V}_4(x) = \hat{V}_{4(a)}e^{-\gamma_4 x} + \hat{V}_{4(b)}e^{\gamma_4 x} \\ \quad\vdots \\ \hat{V}_{2n}(x) = \hat{V}_{2n(a)}e^{-\gamma_{2n} x} + \hat{V}_{2n(b)}e^{\gamma_{2n} x} \end{cases} \tag{3-24}$$

$$\begin{cases} \hat{I}_1(x) = \hat{I}_{1(a)}e^{-\gamma_1 x} + \hat{I}_{1(b)}e^{\gamma_1 x} \\ \hat{I}_2(x) = \hat{I}_{2(a)}e^{-\gamma_2 x} + \hat{I}_{2(b)}e^{\gamma_2 x} \\ \hat{I}_3(x) = \hat{I}_{3(a)}e^{-\gamma_3 x} + \hat{I}_{3(b)}e^{\gamma_3 x} \\ \hat{I}_4(x) = \hat{I}_{4(a)}e^{-\gamma_4 x} + \hat{I}_{4(b)}e^{\gamma_4 x} \\ \quad\vdots \\ \hat{I}_{2n}(x) = \hat{I}_{2n(a)}e^{-\gamma_{2n} x} + \hat{I}_{2n(b)}e^{\gamma_{2n} x} \end{cases} \tag{3-25}$$

To establish a link between modal voltages and modal currents such that

$$\hat{I}_i(x) = \hat{Y}_{wi}(\hat{V}_{i(a)}e^{-\gamma_i x} + \hat{V}_{i(b)}e^{\gamma_i x}) \quad \text{(i=1,2,3,4,…,2n)} \tag{3-26}$$

the characteristic wave modal admittances

$$\hat{\mathbf{Y}}_{\mathbf{w}} = diag\{\hat{Y}_{w1}, \hat{Y}_{w2}, \hat{Y}_{w3}, \hat{Y}_{w4}, \cdots, \hat{Y}_{w2n}\} \tag{3-27}$$

need to be obtained so that

$$\begin{cases} \hat{\mathbf{I}}_{\mathbf{(a)}} = +\hat{\mathbf{Y}}_{\mathbf{w}}\hat{\mathbf{V}}_{\mathbf{(a)}} \\ \hat{\mathbf{I}}_{\mathbf{(b)}} = -\hat{\mathbf{Y}}_{\mathbf{w}}\hat{\mathbf{V}}_{\mathbf{(b)}} \end{cases} \tag{3-28}$$

$\hat{\mathbf{V}}_{\mathbf{(a)}}$, $\hat{\mathbf{I}}_{\mathbf{(a)}}$ and $\hat{\mathbf{V}}_{\mathbf{(b)}}$, $\hat{\mathbf{I}}_{\mathbf{(b)}}$ represent the incident wave and reflected wave, respectively.

Considering one of the equations in (3-14), and replacing natural quantities by modal ones, we have

$$\hat{\mathbf{Y}}_{\mathbf{w}} = (\mathbf{T}^{\mathrm{T}}\mathbf{Z}^{-1}\mathbf{T})\boldsymbol{\gamma} \tag{3-29}$$

The characteristic modal impedance

$$\hat{\mathbf{Z}}_{\mathbf{w}} = \hat{\mathbf{Y}}_{\mathbf{w}}^{-1} = diag\{\hat{Z}_{w1}, \hat{Z}_{w2}, \hat{Z}_{w3}, \hat{Z}_{w4}, \cdots, \hat{Z}_{w2n}\} \tag{3-30}$$

From (3-20)(3-21)(3-24)(3-25)(3-26), we get the modal solution of the multi-conductor transmission line equations as

$$\begin{cases} \mathbf{V(x)} = \mathbf{T}\hat{\mathbf{V}}\mathbf{(x)} = \sum_{i=1}^{2n} \mathbf{t_i} (\hat{V}_{i(a)} e^{-\gamma_i x} + \hat{V}_{i(b)} e^{\gamma_i x}) \\ \mathbf{I(x)} = \mathbf{W}\hat{\mathbf{I}}\mathbf{(x)} = \sum_{i=1}^{2n} \mathbf{w_i} \hat{Y}_{wi} (\hat{V}_{i(a)} e^{-\gamma_i x} - \hat{V}_{i(b)} e^{\gamma_i x}) \end{cases} \tag{3-31}$$

or

$$\begin{cases} \mathbf{V} = \mathbf{T}e^{-\gamma x}\mathbf{T}^{-1}\mathbf{T}\hat{\mathbf{V}}_{\mathbf{(a)}} + \mathbf{T}e^{\gamma x}\mathbf{T}^{-1}\mathbf{T}\hat{\mathbf{V}}_{\mathbf{(b)}} \\ \mathbf{I} = \mathbf{W}\hat{\mathbf{Y}}_{\mathbf{w}}\mathbf{T}^{-1}(\mathbf{T}e^{-\gamma x}\mathbf{T}^{-1}\mathbf{T}\hat{\mathbf{V}}_{\mathbf{(a)}} - \mathbf{T}e^{\gamma x}\mathbf{T}^{-1}\mathbf{T}\hat{\mathbf{V}}_{\mathbf{(b)}}) \end{cases} \tag{3-32}$$

where $e^{-\gamma x}$ and $e^{\gamma x}$ are diagonal matrices

$$\begin{cases} e^{-\gamma x} = diag\{e^{-\gamma_1 x}, e^{-\gamma_2 x}, e^{-\gamma_3 x}, e^{-\gamma_4 x}, \cdots, e^{-\gamma_{2n} x}\} \\ e^{\gamma x} = diag\{e^{\gamma_1 x}, e^{\gamma_2 x}, e^{\gamma_3 x}, e^{\gamma_4 x}, \cdots, e^{\gamma_{2n} x}\} \end{cases} \tag{3-33}$$

and $\hat{\mathbf{V}}_{\mathbf{(a)}}$ and $\hat{\mathbf{V}}_{\mathbf{(b)}}$ are column matrices collecting the amplitudes of the incident and reflected waves of the modal voltages at x=0, respectively.

$$\hat{\mathbf{V}}_{\mathbf{(a)}} = \begin{bmatrix} \hat{V}_{1(a)} \\ \hat{V}_{2(a)} \\ \hat{V}_{3(a)} \\ \hat{V}_{4(a)} \\ \vdots \\ \hat{V}_{2n(a)} \end{bmatrix}, \quad \hat{\mathbf{V}}_{\mathbf{(b)}} = \begin{bmatrix} \hat{V}_{1(b)} \\ \hat{V}_{2(b)} \\ \hat{V}_{3(b)} \\ \hat{V}_{4(b)} \\ \vdots \\ \hat{V}_{2n(b)} \end{bmatrix} \tag{3-34}$$

Referring to (3-32), we introduce the following quantities:

incident wave amplitudes of real voltages:

$$\mathbf{V}_{\mathbf{(a)}} = \mathbf{T}\hat{\mathbf{V}}_{\mathbf{(a)}} \tag{3-35}$$

reflected wave amplitudes of real voltages:

$$\mathbf{V}_{\mathbf{(b)}} = \mathbf{T}\hat{\mathbf{V}}_{\mathbf{(b)}} \tag{3-36}$$

incident wave amplitudes of real currents:

$$\mathbf{I}_{\mathbf{(a)}} = \mathbf{Y}_{\mathbf{w}}\mathbf{V}_{\mathbf{(a)}} \tag{3-37}$$

reflected wave amplitudes of real currents:

$$\mathbf{I}_{\mathbf{(b)}} = -\mathbf{Y}_{\mathbf{w}}\mathbf{V}_{\mathbf{(b)}} \tag{3-38}$$

characteristic wave admittance matrix in natural coordinates:

$$\mathbf{Y}_{\mathbf{w}} = \mathbf{W}\hat{\mathbf{Y}}_{\mathbf{w}}\mathbf{T}^{-1} = \mathbf{Z}^{-1}\boldsymbol{\Gamma} = \mathbf{Y}\boldsymbol{\Gamma}^{-1} \tag{3-39}$$

characteristic wave impedance matrix in natural coordinates:

$$\mathbf{Z}_{\mathrm{w}} = \mathbf{Y}_{\mathrm{w}}^{-1} = \boldsymbol{\Gamma}^{-1}\mathbf{Z} = \boldsymbol{\Gamma}\mathbf{Y}^{-1} \tag{3-40}$$

in which,

$$\boldsymbol{\Gamma} = \mathbf{T}\boldsymbol{\gamma}\,\mathrm{T}^{-1} \tag{3-41}$$

Denoting that

$$\mathrm{EXP}(\pm\boldsymbol{\Gamma}x) = \mathbf{T}e^{\pm\gamma x}\mathbf{T}^{-1} \tag{3-42}$$

$$\mathrm{COSH}(\boldsymbol{\Gamma}x) = \frac{1}{2}\left[\mathrm{EXP}(+\boldsymbol{\Gamma}x) + \mathrm{EXP}(-\boldsymbol{\Gamma}x)\right] \tag{3-43}$$

$$\mathrm{SINH}(\boldsymbol{\Gamma}x) = \frac{1}{2}\left[\mathrm{EXP}(+\boldsymbol{\Gamma}x) - \mathrm{EXP}(-\boldsymbol{\Gamma}x)\right] \tag{3-44}$$

Equation (3-32) can be rewritten as

$$\begin{cases} \mathbf{V}(x) = \dfrac{1}{2}\left[\mathrm{EXP}(+\boldsymbol{\Gamma}x) + \mathrm{EXP}(-\boldsymbol{\Gamma}x)\right]\mathbf{V}(0) - \dfrac{1}{2}\left[\mathrm{EXP}(+\boldsymbol{\Gamma}x) - \mathrm{EXP}(-\boldsymbol{\Gamma}x)\right]\mathbf{Z}_{\mathrm{w}}\mathbf{I}(0) \\ \mathbf{I}(x) = -\mathbf{Y}_{\mathrm{w}}\dfrac{1}{2}\left[\mathrm{EXP}(+\boldsymbol{\Gamma}x) - \mathrm{EXP}(-\boldsymbol{\Gamma}x)\right]\mathbf{V}(0) + \mathbf{Y}_{\mathrm{w}}\dfrac{1}{2}\left[\mathrm{EXP}(+\boldsymbol{\Gamma}x) + \mathrm{EXP}(-\boldsymbol{\Gamma}x)\right]\mathbf{Z}_{\mathrm{w}}\mathbf{I}(0) \end{cases} \tag{3-45}$$

in which,

$$\mathbf{V}(0) = \begin{bmatrix} V_1(0) \\ V_2(0) \\ V_3(0) \\ \vdots \\ V_{2n}(0) \end{bmatrix} \tag{3-46}$$

$$\mathbf{I}(0) = \begin{bmatrix} I_1(0) \\ I_2(0) \\ I_3(0) \\ \vdots \\ I_{2n}(0) \end{bmatrix} \tag{3-47}$$

$$\mathbf{V}(x) = \begin{bmatrix} V_1(x) \\ V_2(x) \\ V_3(x) \\ \vdots \\ V_{2n}(x) \end{bmatrix} \tag{3-48}$$

$$\mathbf{I}(x) = \begin{bmatrix} I_1(x) \\ I_2(x) \\ I_3(x) \\ \vdots \\ I_{2n}(x) \end{bmatrix} \tag{3-49}$$

Equation (3-45) can be presented as

$$\begin{cases} \mathbf{V}(x) = \mathbf{F}_{\mathrm{V}}\mathbf{V}(0) + \mathbf{G}_{\mathrm{V}}\mathbf{I}(0) \\ \mathbf{I}(x) = \mathbf{F}_{\mathrm{I}}\mathbf{V}(0) + \mathbf{G}_{\mathrm{I}}\mathbf{I}(0) \end{cases} \tag{3-50}$$

in which,

$$\mathbf{F}_{\mathrm{V}}(x)=\frac{1}{2}\left[\mathrm{EXP}(+\boldsymbol{\Gamma}x)+\mathrm{EXP}(-\boldsymbol{\Gamma}x)\right]=\mathrm{COSH}(\boldsymbol{\Gamma}x) \tag{3-51}$$

$$\mathbf{G}_{\mathrm{V}}(x)=-\frac{1}{2}\left[\mathrm{EXP}(+\boldsymbol{\Gamma}x)-\mathrm{EXP}(-\boldsymbol{\Gamma}x)\right]\mathbf{Z}_{\mathrm{w}}=-\mathrm{SINH}(\boldsymbol{\Gamma}x)\cdot\mathbf{Z}_{\mathrm{w}} \tag{3-52}$$

$$\mathbf{F}_{\mathrm{I}}(x)=-\mathbf{Y}_{\mathrm{w}}\frac{1}{2}\left[\mathrm{EXP}(+\boldsymbol{\Gamma}x)-\mathrm{EXP}(-\boldsymbol{\Gamma}x)\right]=-\mathbf{Y}_{\mathrm{w}}\cdot\mathrm{SINH}(\boldsymbol{\Gamma}x) \tag{3-53}$$

$$\mathbf{G}_{\mathrm{I}}(x)=\mathbf{Y}_{\mathrm{w}}\frac{1}{2}\left[\mathrm{EXP}(+\boldsymbol{\Gamma}x)+\mathrm{EXP}(-\boldsymbol{\Gamma}x)\right]\mathbf{Z}_{\mathrm{w}}=\mathbf{Y}_{\mathrm{w}}\cdot\mathrm{COSH}(\boldsymbol{\Gamma}x)\cdot\mathbf{Z}_{\mathrm{w}} \tag{3-54}$$

These allow us to determine **V**(x) and **I**(x) in terms of **V**(0) and **I**(0),

$$\begin{bmatrix}\mathbf{V}(x)\\ \mathbf{I}(x)\end{bmatrix}=\begin{bmatrix}\mathbf{F}_{\mathrm{V}}(x) & \mathbf{G}_{\mathrm{V}}(x)\\ \mathbf{F}_{\mathrm{I}}(x) & \mathbf{G}_{\mathrm{I}}(x)\end{bmatrix}\begin{bmatrix}\mathbf{V}(0)\\ \mathbf{I}(0)\end{bmatrix}=\mathbf{FG}(x)\cdot\begin{bmatrix}\mathbf{V}(0)\\ \mathbf{I}(0)\end{bmatrix} \tag{3-55}$$

3.4. Application of Multi-conductor Transmission Structure to Integrated Passives

Excited by the idea of cascaded transmission structure discussed in section 2.5, the L-C cells in a multi-conductor structure can also be connected in a similar method. Figure 3-8 shows the interconnections between L-C cells as a series resonator and a parallel resonator. A typical impedance of a 3-cell series resonator shown in Figure 3-8(a) is illustrated in Figure 3-9 while that of a parallel resonator shown in Figure 3-8(b) is illustrated in Figure 3-10. The details of calculation will be presented in Chapter 5.

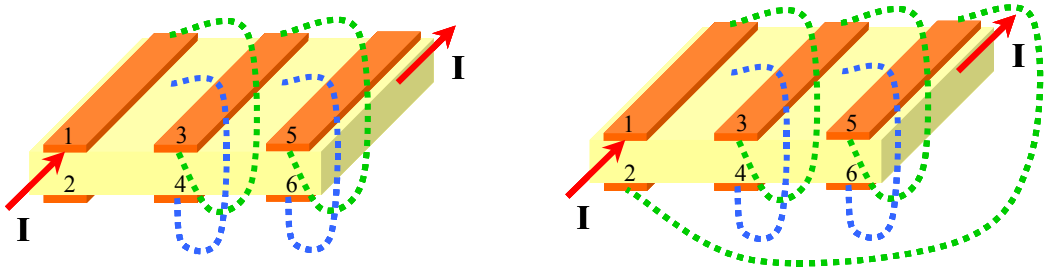

(a) Series resonator (b) Parallel resonator

Figure 3-8: Interconnections for series resonator and parallel resonator.

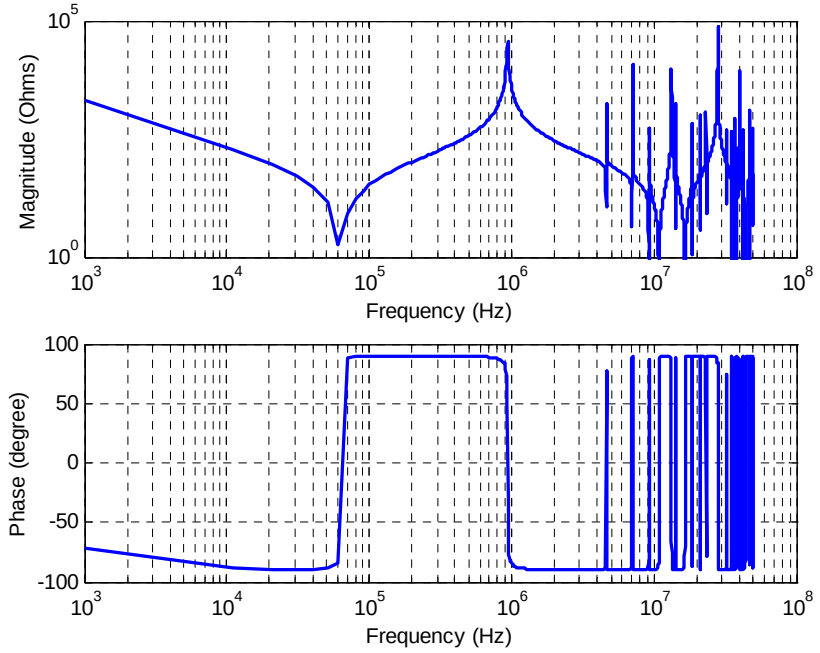

Figure 3-9: Typical impedance of the series resonant structure shown in Figure 3-8(a).

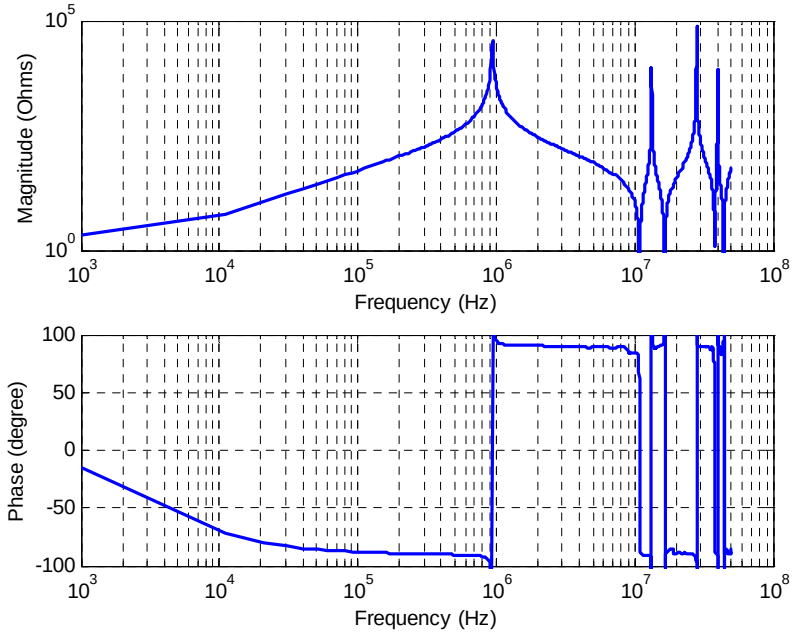

Figure 3-10: Typical impedance of the series resonant structure shown in Figure 3-8(b).

3.5. Conclusion

As a more generalized study of distributed passive structures, two-conductor transmission structure model presented in Chapter 2 has been extended to the modeling of multiple conductors. As multiple two-conductor structures are putting together in parallel, both magnetic and capacitive coupling between cells need to be considered as well. To determine the capacitance between two adjacent conductors on top of the same dielectric substrate, Schwarz-Christoffel transformation and its inverse have been applied with the calculation results verified by measurement. Based on the original voltage and current equations written in matrix form, state space transformation has been conducted to decouple the voltages and currents so that the equations can be solved easily. Through modal analysis and matrix manipulations, the relationship between voltage and current at one point and those at another can be determined. All these provide the basis for any further modeling of an integrated passive structure. The possible applications to integrated resonators have also been discussed.

Chapter 4: Case Study: The Frequency Plane Modeling of the Conventional Spiral Winding Structure Integrated Power Passives

4.1. Introduction

In Chapter 2 and Chapter 3, two-conductor and multi-conductor generalized transmission structures and their formulations have been introduced, respectively. In this chapter, these generalized transmission structure equations will be extended and applied to the modeling of the conventional spiral winding structure integrated passives (see Figure 1-12).

4.2. Modeling of a Conventional Structure Integrated Passives

An integrated L-C module can be divided into 5 sections, from A to E, as shown in Figure 4-1. Of the 5 sections, B and D are already perfect parallel multi-conductor transmission structures. However, equations in Chapter 3 cannot be applied to section A, C and E unless appropriate transformations can be conducted.

From the two-conductor transmission structure equations, it is noted that the characteristics would not change as long as the product of γ (propagation coefficient) and l (structure length) does not change. From equation **(2-8)**, same γl leads to same Rl, Gl, Ll, Ml and Cl, or same total impedance. Therefore, theoretically, the impedance per unit length can be changed to suit the normalized length of a section while keeping the characteristics of that section still the same. As a result, all conductors in the same section can be normalized to the same length. The numbering of the conductors of a 3-turn integrated passives structure is shown in Figure 4-2(a). The entire module can be treated as 5 sections of multi-conductor transmission structures with their interconnections shown in Figure 4-2(b).

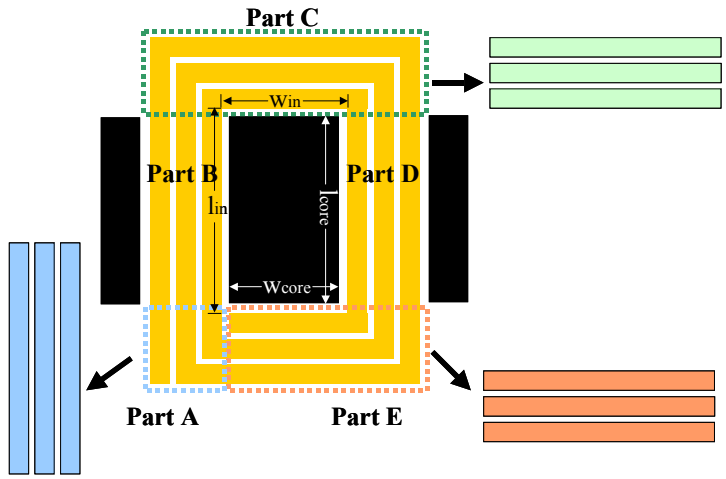

Figure 4-1: 5 sections of a conventional structure integrated passives (top internal view).

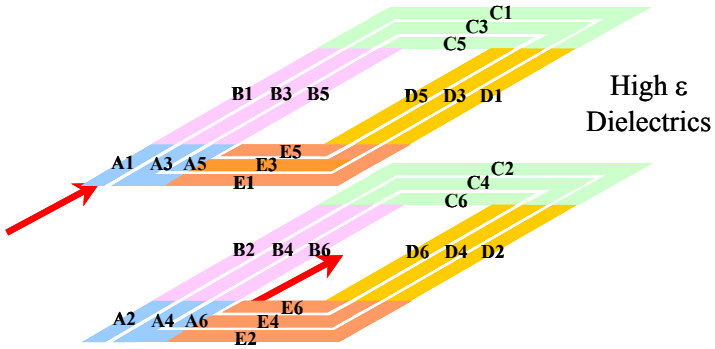

(a) Conductor numbering

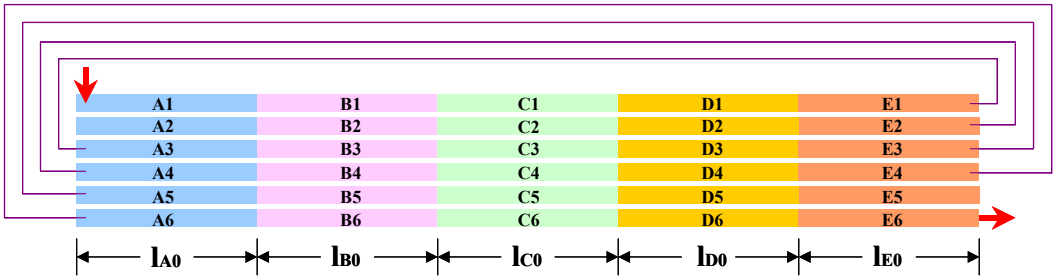

(b) Equivalent cascaded multi-conductor transmission structures.

Figure 4-2: Conductor numbering of a 3-turn structure and its equivalent cascaded multi-conductor transmission structures.

The normalized length of each section

$$l_{A0}=(l_{in}-l_{core})/2+n(w+d)-d \quad (4\text{-}1)$$

$$l_{B0}=l_{D0}=l_{core} \quad (4\text{-}2)$$

$$l_{C0}=w_{in}+2w+l_{in}-l_{core} \quad (4\text{-}3)$$

$$l_{E0}=w_{in}+w-d+(l_{in}-l_{core})/2 \quad (4\text{-}4)$$

in which n is the number of turns and l_{in}, w_{in}, l_{core}, w_{core} have been given in Figure 4-1.

The real length of each conductor track

$$l_{A1}=l_{A2}=l_{A0} \quad (4\text{-}5)$$

$$l_{A3}=l_{A4}=l_{A0}+(n-2)(w+d)+d \quad (4\text{-}6)$$

$$l_{A2i-1}=l_{A2i}=l_{A0}+[n-2(i-1)](w+d)+d \quad (i=2,3,\ldots n) \quad (4\text{-}7)$$

$$l_B=l_{B0} \quad (4\text{-}8)$$

$$l_{C2i-1}=l_{C2i}=l_{C0}+4(n-i)(w+d) \quad (i=1,2,\ldots n) \quad (4\text{-}9)$$

$$l_D=l_{D0} \quad (4\text{-}10)$$

$$l_{E2i-1}=l_{E2i}=l_{E0}+2(n-i)(w+d) \quad (i=1,2,\ldots n) \quad (4\text{-}11)$$

The real length of an inter-winding gap with which two adjacent conductors are involved

$$l_{A1,3}=l_{A2,4}=l_{A0} \quad (4\text{-}12)$$

$$l_{Ai,i+2}= l_{Ai+2}+w \quad (i=3,4,5,\ldots 2n-2) \quad (4\text{-}13)$$

$$l_{Bi,i+2}= l_{B0} \quad (i=1,2,3,\ldots 2n-2) \quad (4\text{-}14)$$

$$l_{Ci,i+2}=l_{Ci+2}+2w \quad (i=1,2,3,\ldots 2n-2) \quad (4\text{-}15)$$

$$l_{Di,i+2}= l_{D0} \quad (i=1,2,3,\ldots 2n-2) \quad (4\text{-}16)$$

$$l_{Ei,i+2}=l_{Ei+2}+w \quad (i=1,2,3,\ldots 2n-2) \quad (4\text{-}17)$$

In the capacitance matrix $\mathbf{C_X}$ of each section (X=A,B,C,D,E),

$$C_{X2i-1,2i}=C_{X2i,2i-1}=C_u l_{X2i-1,2i}/l_{X0}\,(\text{F/m}) \quad (i=1,2,3,\ldots n) \quad (4\text{-}18)$$

$$C_{X2i-1,2i+1}=C_{X2i,2i+2}=C_g l_{X2i-1,2i+1}/l_{X0}\,(\text{F/m}) \quad (i=1,2,3,\ldots n\text{-}1) \quad (4\text{-}19)$$

while all the other elements in matrix $\mathbf{C_X}$ are 0.

in which,

$$C_u=\varepsilon_0\varepsilon_r w/t\ (\text{F/m}) \quad (4\text{-}20)$$

$$C_g=\varepsilon_0\varepsilon_r\frac{\nu_1}{\sigma}\,(\text{F/m}) \quad \text{(see Chapter 3)} \quad (4\text{-}21)$$

Since the structure-based inductance calculation is not the main focus of this modeling work, the lumped inductance matrix of the conductors of each section $\mathbf{L_{X0}}$ (X=A,B,C,D,E)

can be obtained by FEM simulation. The matrix of inductance per unit length $\mathbf{L_X}$ of each section (X=A,B,C,D,E) can be obtained by

$$\mathbf{L_X} = \mathbf{L_{X0}}/l_{X0} \quad (X=A,B,C,D,E) \tag{4-22}$$

Thus each section in a spiral winding structure integrated passives can be transformed into an equivalent standard multi-conductor transmission structures while keeping the total inductance and capacitance associated with each conductor still constant after the transformation.

Equations (3-12)-(3-55) can be applied to each section after transformation. These allow us to determine $\mathbf{V}(x)$ and $\mathbf{I}(x)$ in terms of $\mathbf{V}(0)$ and $\mathbf{I}(0)$ of each section.

$$\begin{bmatrix} \mathbf{V_A}(x_A) \\ \mathbf{I_A}(x_A) \end{bmatrix} = \begin{bmatrix} \mathbf{F_{VA}}(x_A) & \mathbf{G_{VA}}(x_A) \\ \mathbf{F_{IA}}(x_A) & \mathbf{G_{IA}}(x_A) \end{bmatrix} \begin{bmatrix} \mathbf{V_A}(0) \\ \mathbf{I_A}(0) \end{bmatrix} = \mathbf{FGA}(x_A) \cdot \begin{bmatrix} \mathbf{V_A}(0) \\ \mathbf{I_A}(0) \end{bmatrix} \tag{4-23}$$

$$\begin{bmatrix} \mathbf{V_B}(x_B) \\ \mathbf{I_B}(x_B) \end{bmatrix} = \begin{bmatrix} \mathbf{F_{VB}}(x_B) & \mathbf{G_{VB}}(x_B) \\ \mathbf{F_{IB}}(x_B) & \mathbf{G_{IB}}(x_B) \end{bmatrix} \begin{bmatrix} \mathbf{V_B}(0) \\ \mathbf{I_B}(0) \end{bmatrix} = \mathbf{FGB}(x_B) \cdot \begin{bmatrix} \mathbf{V_B}(0) \\ \mathbf{I_B}(0) \end{bmatrix} \tag{4-24}$$

$$\begin{bmatrix} \mathbf{V_C}(x_C) \\ \mathbf{I_C}(x_C) \end{bmatrix} = \begin{bmatrix} \mathbf{F_{VC}}(x_C) & \mathbf{G_{VC}}(x_C) \\ \mathbf{F_{IC}}(x_C) & \mathbf{G_{IC}}(x_C) \end{bmatrix} \begin{bmatrix} \mathbf{V_C}(0) \\ \mathbf{I_C}(0) \end{bmatrix} = \mathbf{FGC}(x_C) \cdot \begin{bmatrix} \mathbf{V_C}(0) \\ \mathbf{I_C}(0) \end{bmatrix} \tag{4-25}$$

$$\begin{bmatrix} \mathbf{V_D}(x_D) \\ \mathbf{I_D}(x_D) \end{bmatrix} = \begin{bmatrix} \mathbf{F_{VD}}(x_D) & \mathbf{G_{VD}}(x_D) \\ \mathbf{F_{ID}}(x_D) & \mathbf{G_{ID}}(x_D) \end{bmatrix} \begin{bmatrix} \mathbf{V_D}(0) \\ \mathbf{I_D}(0) \end{bmatrix} = \mathbf{FGD}(x_D) \cdot \begin{bmatrix} \mathbf{V_D}(0) \\ \mathbf{I_D}(0) \end{bmatrix} \tag{4-26}$$

$$\begin{bmatrix} \mathbf{V_E}(x_E) \\ \mathbf{I_E}(x_E) \end{bmatrix} = \begin{bmatrix} \mathbf{F_{VE}}(x_E) & \mathbf{G_{VE}}(x_E) \\ \mathbf{F_{IE}}(x_E) & \mathbf{G_{IE}}(x_E) \end{bmatrix} \begin{bmatrix} \mathbf{V_E}(0) \\ \mathbf{I_E}(0) \end{bmatrix} = \mathbf{FGE}(x_E) \cdot \begin{bmatrix} \mathbf{V_E}(0) \\ \mathbf{I_E}(0) \end{bmatrix} \tag{4-27}$$

For a conventional spiral-winding structure integrated series resonant module, the voltage boundary conditions are given by

$$
\begin{cases}
V_{A1}(l_{A0}) = V_{B1}(0) \\
V_{A2}(l_{A0}) = V_{B2}(0) \\
\quad\vdots \\
V_{A2n}(l_{A0}) = V_{B2n}(0) \\
V_{B1}(l_{B0}) = V_{C1}(0) \\
V_{B2}(l_{B0}) = V_{C2}(0) \\
\quad\vdots \\
V_{B2n}(l_{B0}) = V_{C2n}(0) \\
V_{C1}(l_{C0}) = V_{D1}(0) \\
V_{C2}(l_{C0}) = V_{D2}(0) \\
\quad\vdots \\
V_{C2n}(l_{C0}) = V_{D2n}(0) \\
V_{D1}(l_{D0}) = V_{E1}(0) \\
V_{D2}(l_{D0}) = V_{E2}(0) \\
\quad\vdots \\
V_{D2n}(l_{D0}) = V_{E2n}(0) \\
V_{E1}(l_{E0}) = V_{A3}(0) \\
V_{E2}(l_{E0}) = V_{A4}(0) \\
V_{E3}(l_{E0}) = V_{A5}(0) \\
V_{E4}(l_{E0}) = V_{A6}(0) \\
\quad\vdots \\
V_{E2n-3}(l_{E0}) = V_{A2n-1}(0) \\
V_{E2n-2}(l_{E0}) = V_{A2n}(0)
\end{cases}
\tag{4-28}
$$

The current boundary conditions are given by

$$
\begin{cases}
I_{A1}(0) = I \\
I_{A2}(0) = 0 \\
I_{A1}(l_{A0}) = I_{B1}(0) \\
I_{A2}(l_{A0}) = I_{B2}(0) \\
\quad\vdots \\
I_{A2n}(l_{A0}) = I_{B2n}(0) \\
I_{B1}(l_{B0}) = I_{C1}(0) \\
I_{B2}(l_{B0}) = I_{C2}(0) \\
\quad\vdots \\
I_{B2n}(l_{B0}) = I_{C2n}(0) \\
I_{C1}(l_{C0}) = I_{D1}(0) \\
I_{C2}(l_{C0}) = I_{D2}(0) \\
\quad\vdots \\
I_{C2n}(l_{C0}) = I_{D2n}(0) \\
I_{D1}(l_{D0}) = I_{E1}(0) \\
I_{D2}(l_{D0}) = I_{E2}(0) \\
\quad\vdots \\
I_{D2n}(l_{D0}) = I_{E2n}(0) \\
I_{E1}(l_{E0}) = I_{A3}(0) \\
I_{E2}(l_{E0}) = I_{A4}(0) \\
I_{E3}(l_{E0}) = I_{A5}(0) \\
I_{E4}(l_{E0}) = I_{A6}(0) \\
\quad\vdots \\
I_{E2n-3}(l_{E0}) = I_{A2n-1}(0) \\
I_{E2n-2}(l_{E0}) = I_{A2n}(0) \\
I_{E2n-1}(l_{E0}) = 0 \\
I_{E2n}(l_{E0}) = I
\end{cases}
\tag{4-29}
$$

From the boundary conditions above, we have

$$
\mathbf{P} \cdot \mathbf{VI}(0) = \mathbf{Q}
\tag{4-30}
$$

in which,

$$
\mathbf{P} = \begin{array}{c}
\begin{matrix} 1\sim 4n & 1\sim 4n & 1\sim 4n & 1\sim 4n & 1\sim 4n \end{matrix} \\
\begin{bmatrix}
\mathbf{FGA} & -\mathbf{E} & \mathbf{O} & \mathbf{O} & \mathbf{O} \\
\mathbf{O} & \mathbf{FGB} & -\mathbf{E} & \mathbf{O} & \mathbf{O} \\
\mathbf{O} & \mathbf{O} & \mathbf{FGC} & -\mathbf{E} & \mathbf{O} \\
\mathbf{O} & \mathbf{O} & \mathbf{O} & \mathbf{FGD} & -\mathbf{E} \\
\mathbf{E1} & \mathbf{O} & \mathbf{O} & \mathbf{O} & \mathbf{FGE1} \\
\mathbf{E2} & \mathbf{O} & \mathbf{O} & \mathbf{O} & \mathbf{O}
\end{bmatrix}
\begin{matrix} \}1\sim 4n \\ \}1\sim 4n \\ \}1\sim 4n \\ \}1\sim 4n \\ \}1\sim 4n-2 \\ \}1\sim 2 \end{matrix}
\end{array}
\tag{4-31}
$$

$$\mathbf{VI}(0)=\begin{bmatrix}\mathbf{V_A}(0)\\ \mathbf{I_A}(0)\\ \mathbf{V_B}(0)\\ \mathbf{I_B}(0)\\ \mathbf{V_C}(0)\\ \mathbf{I_C}(0)\\ \mathbf{V_D}(0)\\ \mathbf{I_D}(0)\\ \mathbf{V_E}(0)\\ \mathbf{I_E}(0)\end{bmatrix} \tag{4-32}$$

$$\mathbf{Q}=\begin{bmatrix}0 & 0 & \cdots & 0 & I & I & 0\end{bmatrix}^T \tag{4-33}$$

$$\mathbf{E}=\begin{matrix}\\ \\ \\ \\ \\ \\ \\ \end{matrix}\overset{1\sim 4n}{\begin{bmatrix}1 & 0 & \cdots & 0 & 0 & 0 & \cdots & 0\\ 0 & 1 & \cdots & 0 & 0 & 0 & \cdots & 0\\ \vdots & \vdots & \ddots & \vdots & \vdots & \vdots & \ddots & \vdots\\ 0 & 0 & \cdots & 1 & 0 & 0 & \cdots & 0\\ 0 & 0 & \cdots & 0 & 1 & 0 & \cdots & 0\\ 0 & 0 & \cdots & 0 & 0 & 1 & \cdots & 0\\ \vdots & \vdots & \ddots & \vdots & \vdots & \vdots & \ddots & \vdots\\ 0 & 0 & \cdots & 0 & 0 & 0 & \cdots & 1\end{bmatrix}}\begin{matrix}\\ \\ \\ \\ \\ \\ \\ \end{matrix}\overset{}{\left.\begin{matrix}\\ \\ \\ \\ \\ \\ \\ \end{matrix}\right\}1\sim 4n} \tag{4-34}$$

$$\mathbf{E1}=\begin{matrix}\\ \\ \\ \\ \\ \\ \\ \\ \\ \\ \end{matrix}\overset{1\sim 2n \quad \cdots \quad 1\sim 2n}{\begin{bmatrix}0 & 0 & -1 & 0 & \cdots & 0 & 0 & 0 & 0 & 0 & \cdots & 0\\ 0 & 0 & 0 & -1 & \cdots & 0 & 0 & 0 & 0 & 0 & \cdots & 0\\ \vdots & \vdots & \vdots & \vdots & \ddots & \vdots & \vdots & \vdots & \vdots & \vdots & \ddots & \vdots\\ 0 & 0 & 0 & 0 & \cdots & -1 & 0 & 0 & 0 & 0 & \cdots & 0\\ 0 & 0 & 0 & 0 & \cdots & 0 & 0 & 0 & -1 & 0 & \cdots & 0\\ 0 & 0 & 0 & 0 & \cdots & 0 & 0 & 0 & 0 & -1 & \cdots & 0\\ \vdots & \vdots & \vdots & \vdots & \ddots & \vdots & \vdots & \vdots & \vdots & \vdots & \ddots & \vdots\\ 0 & 0 & 0 & 0 & \cdots & 0 & 0 & 0 & 0 & 0 & \cdots & -1\\ 0 & 0 & 0 & 0 & \cdots & 0 & 0 & 0 & 0 & 0 & \cdots & 0\\ 0 & 0 & 0 & 0 & \cdots & 0 & 0 & 0 & 0 & 0 & \cdots & 0\end{bmatrix}}\begin{matrix}\\ \\ \\ \\ \\ \\ \\ \\ \\ \\ \end{matrix}\overset{}{\begin{matrix}\left.\begin{matrix}\\ \\ \\ \\ \end{matrix}\right\}1\sim 2n-2\\ \left.\begin{matrix}\\ \\ \\ \\ \\ \\ \end{matrix}\right\}1\sim 2n\end{matrix}} \tag{4-35}$$

$$\mathbf{E2}=\begin{matrix}\\ \\ \end{matrix}\overset{1\sim 2n \quad \cdots \quad 1\sim 2n}{\begin{bmatrix}0 & 0 & \cdots & 0 & 1 & 0 & 0 & \cdots & 0\\ 0 & 0 & \cdots & 0 & 0 & 1 & 0 & \cdots & 0\end{bmatrix}} \tag{4-36}$$

$$\mathbf{FGE1} = \begin{bmatrix} \mathbf{FGE}_{1,:}(l) \\ \mathbf{FGE}_{2,:}(l) \\ \vdots \\ \mathbf{FGE}_{2n-2,:}(l) \\ \mathbf{FGE}_{2n+1,:}(l) \\ \mathbf{FGE}_{2n+2,:}(l) \\ \vdots \\ \mathbf{FGE}_{4n,:}(l) \end{bmatrix} \tag{4-37}$$

in which $\mathbf{FGE}_{i,:}(l)$ (i=1,2,…2n-2,2n+1,2n+2,…4n) represents the i[th] row of $\mathbf{FGE}(l)$.

Thus, $\mathbf{VI}(0)$ can be obtained from) by (4-30)

$$\mathbf{VI}(0) = \mathbf{P}^{-1}\mathbf{Q} \tag{4-38}$$

When a total current I flows through the module, the voltage across A and B is given by

$$V_{AB} = V_{A1}(0) - V_{E2n}(l_{E0}) \tag{4-39}$$

Therefore, the total impedance Z_{AB} can be simply obtained as

$$Z_{AB} = V_{AB} / I \tag{4-40}$$

4.3. Case Study

4.3.1. A Prototype and The Technical Parameters

A 3-turn integrated series resonant module prototype has been constructed with its pictures and parameters shown in Figure 4-3 and Table 4-1, respectively.

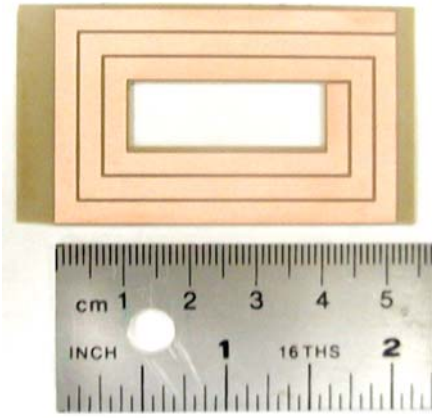

(a) The winding pattern

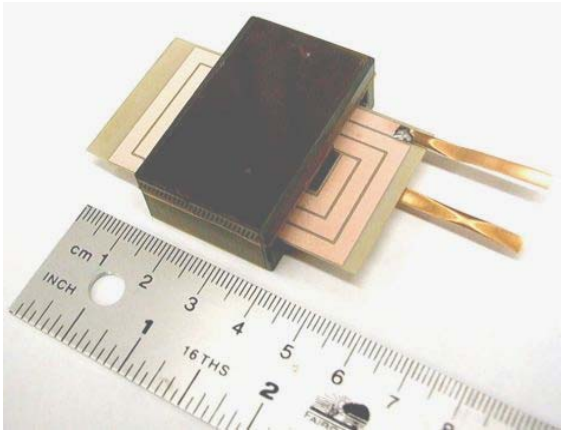

(b) The module

Figure 4-3: The pictures of the prototype.

Table 4-1: Parameters and dimensions

w	3mm
d	26.5mil
t	0.33mm
w_m	11.2mm
l_m	30.2mm
N	3
ε_r	14000
Magnetic core	Philips E43/10/28-3F3 and PLT43/28/4-3F3

4.3.2. Parameters Extraction

To obtain the inductance of section A, C, E and B, D, MAXWELL Q3D and 2D simulations have been done, respectively. The schematics are shown in Figure 4-4.

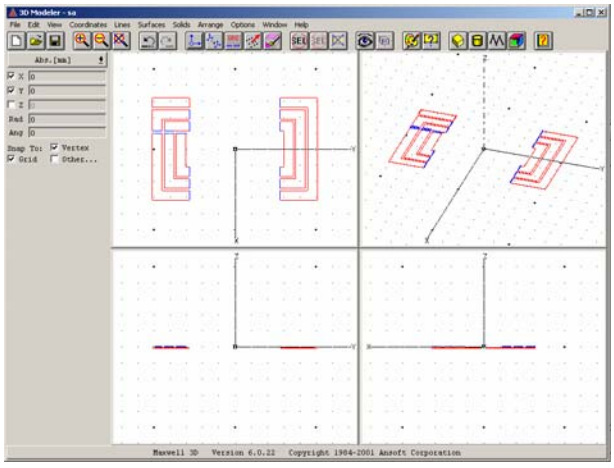

(a) Schematics for section A, C and E

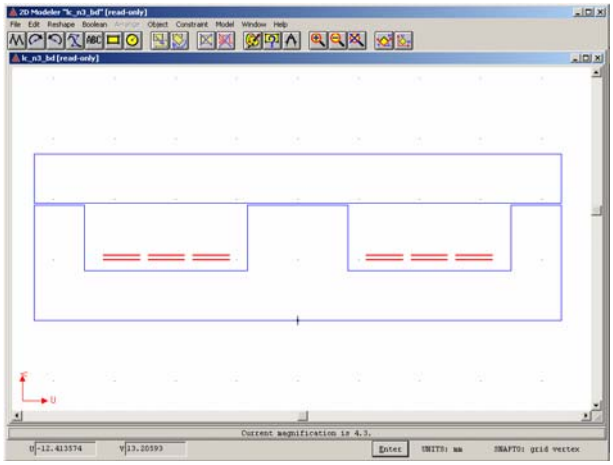

(b) Schematics for section B and D

Figure 4-4: MAXWELL simulation schematics for different sections.

The inductance matrices of the 5 sections obtained from MAXWELL simulation are given below:

L_{A0}=

[5.6291e-009 4.986e-009 2.2958e-009 2.2699e-009 8.5282e-010 8.5406e-010
4.986e-009 5.583e-009 2.2763e-009 2.2714e-009 8.4834e-010 8.5126e-010
2.2958e-009 2.2763e-009 5.9963e-009 5.235e-009 1.4406e-009 1.4342e-009
2.2699e-009 2.2714e-009 5.235e-009 5.9533e-009 1.4227e-009 1.4305e-009
8.5282e-010 8.4834e-010 1.4406e-009 1.4227e-009 2.2447e-009 1.9367e-009
8.5406e-010 8.5126e-010 1.4342e-009 1.4305e-009 1.9367e-009 2.2557e-009]

L_{B0}=

[7.1837E-007 7.174E-007 7.1143E-007 7.116E-007 7.0776E-007 7.0793E-007
7.174E-007 7.1999E-007 7.1188E-007 7.1215E-007 7.0816E-007 7.0835E-007
7.1143E-007 7.1188E-007 7.2119E-007 7.1995E-007 7.1576E-007 7.1599E-007
7.116E-007 7.1215E-007 7.1995E-007 7.2226E-007 7.1598E-007 7.163E-007

7.0776E-007 7.0816E-007 7.1576E-007 7.1598E-007 7.2744E-007 7.2623E-007
7.0793E-007 7.0835E-007 7.1599E-007 7.163E-007 7.2623E-007 7.2859E-007]

L_{C0}=
[2.5638e-008 2.3222e-008 9.2204e-009 9.2949e-009 3.3056e-009 3.3134e-009
2.3222e-008 2.5431e-008 9.1429e-009 9.3006e-009 3.2781e-009 3.2902e-009
9.2204e-009 9.1429e-009 1.4226e-008 1.2807e-008 4.3601e-009 4.3566e-009
9.2949e-009 9.3006e-009 1.2807e-008 1.4496e-008 4.3505e-009 4.3886e-009
3.3056e-009 3.2781e-009 4.3601e-009 4.3505e-009 7.1952e-009 6.4201e-009
3.3134e-009 3.2902e-009 4.3566e-009 4.3886e-009 6.4201e-009 7.2168e-009]

L_{D0}=
[7.1682E-007 7.1585E-007 7.0989E-007 7.1006E-007 7.0624E-007 7.0642E-007
7.1585E-007 7.1844E-007 7.1034E-007 7.1061E-007 7.0664E-007 7.0683E-007
7.0989E-007 7.1034E-007 7.1967E-007 7.1843E-007 7.1426E-007 7.1449E-007
7.1006E-007 7.1061E-007 7.1843E-007 7.2074E-007 7.1448E-007 7.148E-007
7.0624E-007 7.0664E-007 7.1426E-007 7.1448E-007 7.2593E-007 7.247E-007
7.0642E-007 7.0683E-007 7.1449E-007 7.148E-007 7.247E-007 7.2704E-007]

L_{E0}=
[1.586e-008 1.4265e-008 6.6234e-009 6.5818e-009 3.0758e-009 3.0667e-009
1.4265e-0081.5745e-008 6.5687e-009 6.5801e-009 3.0607e-009 3.0569e-009
6.6234e-0096.5687e-009 1.0597e-008 9.4594e-009 3.9364e-009 3.9041e-009
6.5818e-0096.5801e-009 9.4594e-009 1.0591e-008 3.9091e-009 3.9106e-009
3.0758e-0093.0607e-009 3.9364e-009 3.9091e-009 6.3442e-009 5.6219e-009
3.0667e-0093.0569e-009 3.9041e-009 3.9106e-009 5.6219e-009 6.3342e-009]

4.3.3. Calculation Results and Small-Signal Measurement Results

In practice, an integrated passive module is always used with input leads, connecting to either a circuit or a measurement setup. Therefore, the measured impedance also includes the impedance of input leads that may not be negligible at high frequency. In this calculation, the inductance of each lead is assumed to be L_w=15nH.

The calculation and measurement results are compared in Figure 4-5. They correlate well with error within 10%.

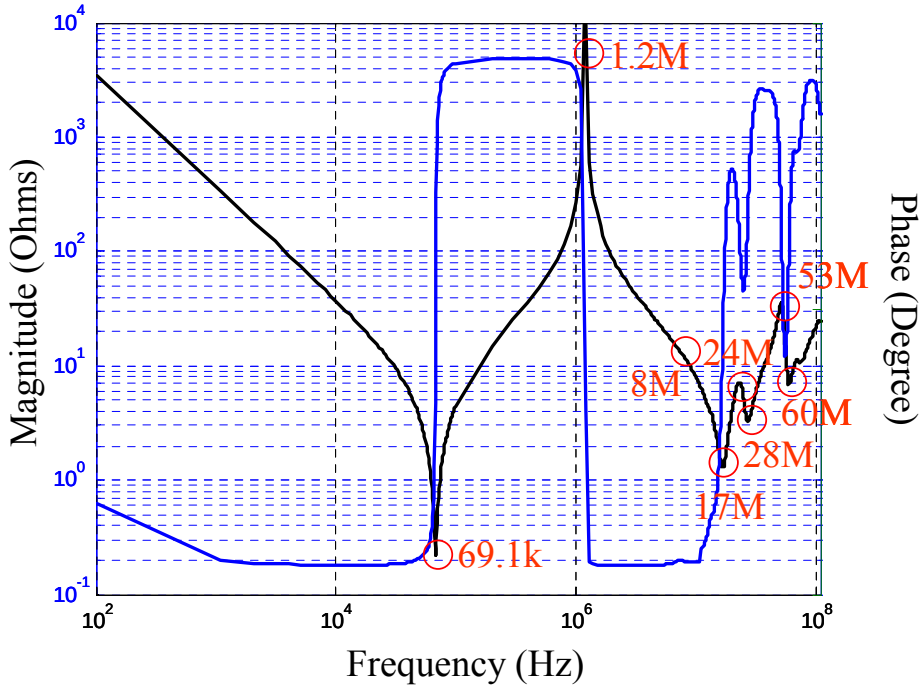

(a) Calculation results

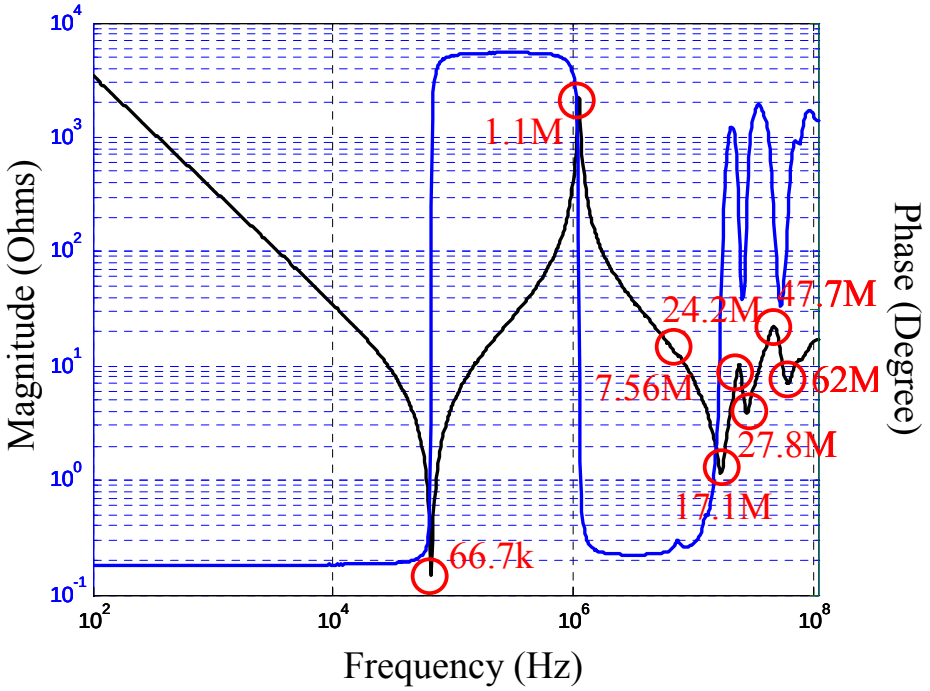

(b) Measurement results

Figure 4-5: Calculation results and measurement results.

4.3.4. Large Signal Measurement Results

To verify the accuracy of the proposed model at large signal, a large-signal measurement setup shown in Figure 4-6 has been developed. The LC module under test is the one shown in Figure 4-3. A 0.0974Ω precision shunt is used to measure the current. Varying the frequency of the sinusoidal output voltage of the power amplifier, the impedance of the integrated LC module at each frequency can be obtained by dividing V_2 by $V_1/0.0974$. The peak-to-peak magnitude of the input current is kept as 2A.

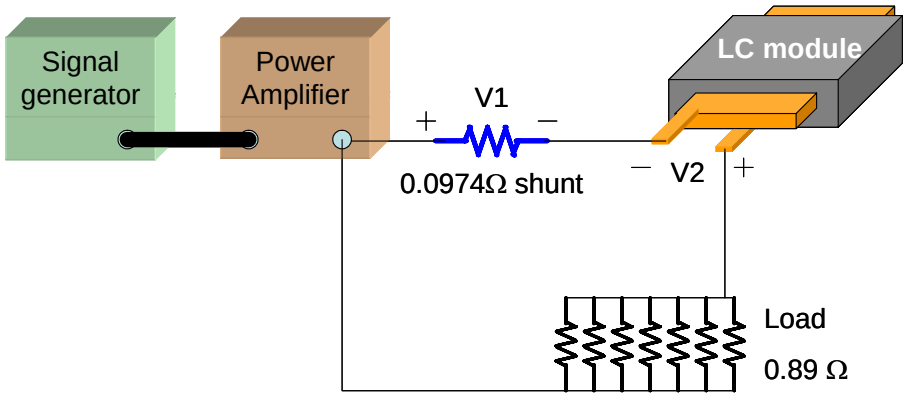

Figure 4-6: Large-signal measurement setup.

The small-signal and large-signal impedance measurement results are compared in Figure 4-7. There is a good correlation between them. The significant discrepancy between large-signal and small-signal measurement results around resonant frequency is due to the waveform distortion introduced by the power amplifier. This can be seen from the difference between the waveforms at resonant frequency as shown in Figure 4-8(b) and those at other frequencies as shown in Figure 4-8.

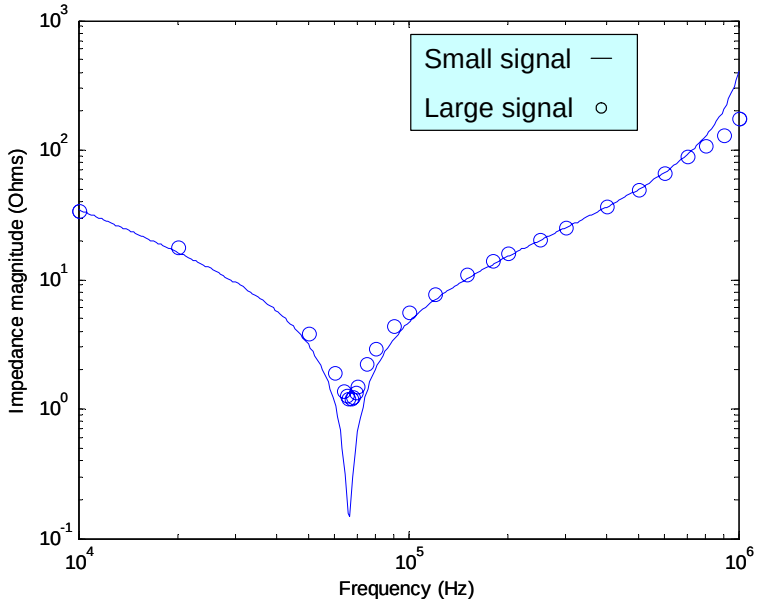

Figure 4-7: Comparison between small-signal and large-signal measurement results

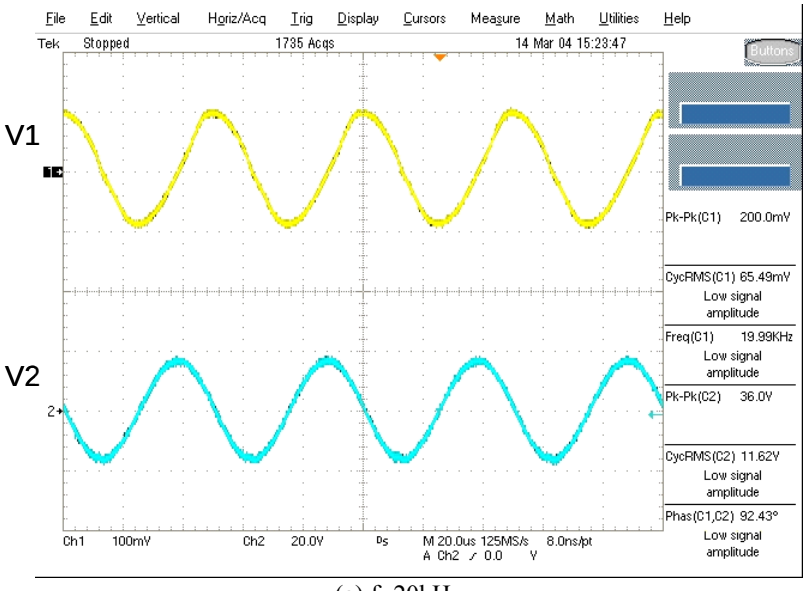

(a) f=20kHz

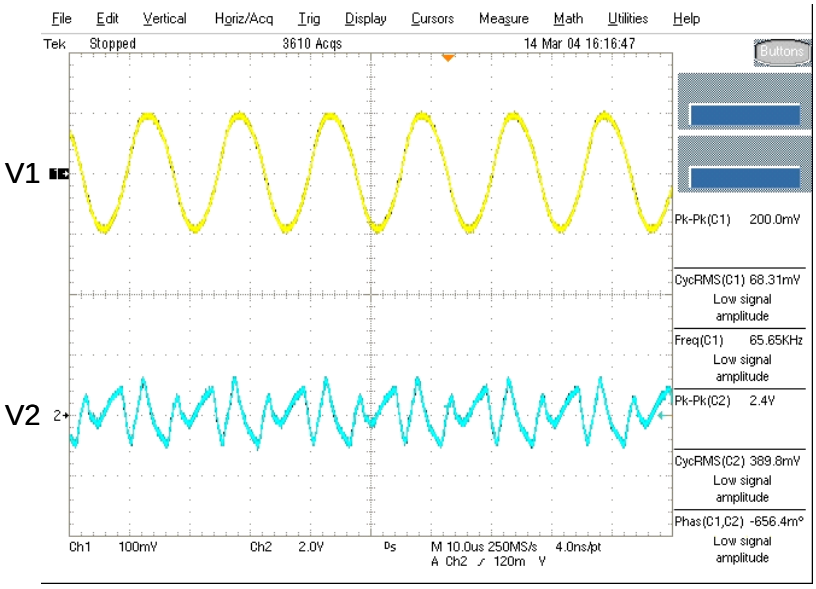

(b) 66kHz

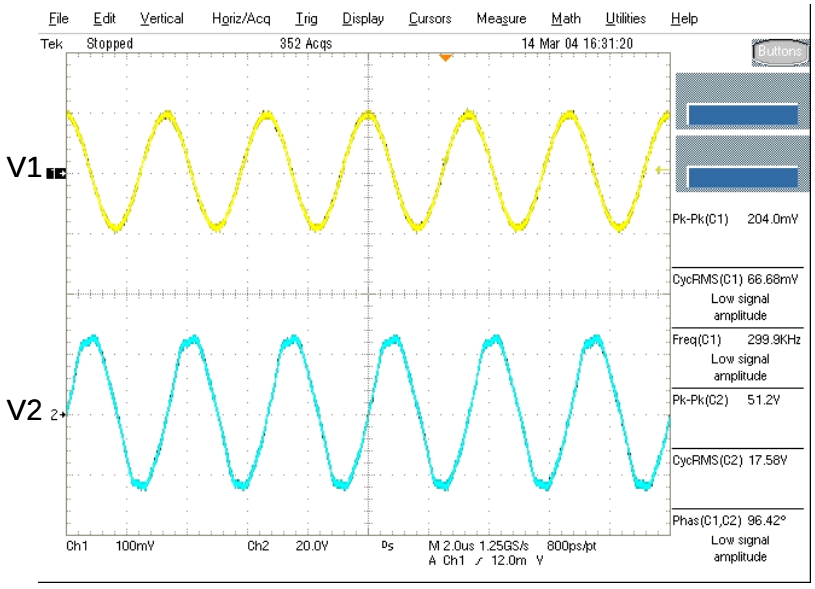

(c) 300kHz

Figure 4-8: Waveforms of V1 and V2 at various frequencies.

4.4. Discussion

Previous sections demonstrate the modeling process and calculation results of a spiral winding structure integrated passive module. However, the causes of the high frequency resonance are still to be identified.

Firstly, overhang section A, C and E are outside the magnetic core and may have a much lower coupling between conductors. Removing the inductance of section A, C and E by letting inductance matrix $\mathbf{L_A=L_C=L_E=0}$, the calculated impedance is shown in Figure 4-9(a). Compared with Figure 4-5, it can be seen that only the characteristics at very high frequency range has changed a bit. The removal of $\mathbf{L_A}$, $\mathbf{L_C}$ and $\mathbf{L_E}$ has little effect on the 1st, 2nd and 3rd resonant frequencies.

Let us continue to study the influence of the leakage inductance of section B and D. Assuming a perfect coupling at the in-core sections B and D, or $\mathbf{K_B=K_D=I}$, the impedance versus frequency characteristics are shown in Figure 4-9(b). $\mathbf{K_B}$ and $\mathbf{K_D}$ represent the coupling coefficient matrix of section B and D, respectively. **I** is a matrix in which every element is 1. From Figure 4-9(b), the high frequency resonance above the 3rd resonant frequency disappears with a perfect coupling in section B and D while still having little effect on the 1st, 2nd and 3rd resonant frequencies.

With the other parameters same as those in Figure 4-9(b), Figure 4-9(c) shows the characteristics without taking lead inductance into account. Obviously, the 3rd resonance is gone when $L_w=0$. Then its cause can be identified as the series resonance between the lead inductance L_w and the inter-winding capacitance C_p.

From Figure 4-9(c) to (d), the spacing between turns d (see Figure 3-3) has been increased to 3mm instead of 0.67mm. As a result, the 2nd resonant peak moves to higher frequency. From section 3.2, the inter-winding capacitance decreases when increasing d. Therefore, the 2nd resonant peak of an integrated passives may be ascribed to the parallel resonance between the winding inductance and the inter-winding capacitance. This can be verified by the impedance test results of the module at the terminal AD and BD, as shown in Figure 4-10. As a series resonance interconnection, external terminals are connected to A and D, as shown in Figure 4-10(a). The winding impedance at one side of the substrate can be observed at the terminal BD shown in Figure 4-10(c). It is very interesting that the impedance curve around the parallel resonant frequency in Figure 4-10(b) is almost the same as that of Figure 4-10(d). Thus, the high frequency 2nd resonant peak can be modeled as a parallel resonance between the winding inductance and the inter-winding capacitance.

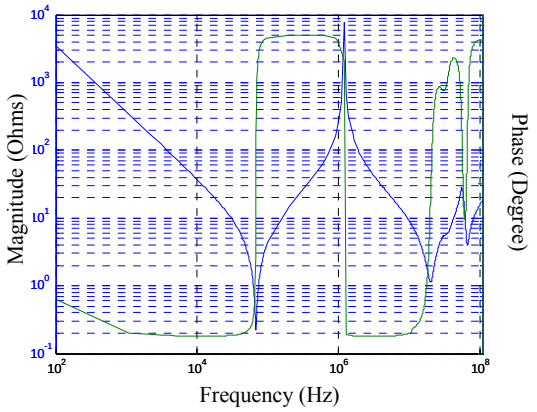

(a) $\mathbf{L_A=L_C=L_E=0}$

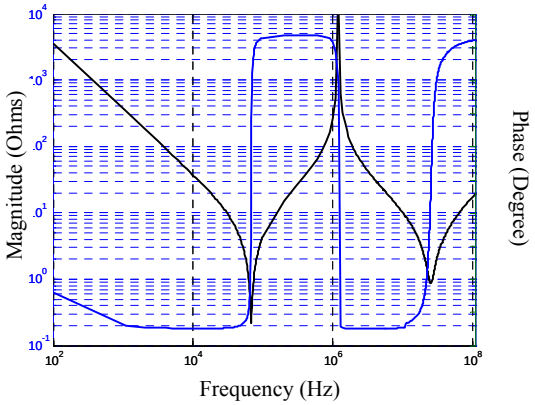

(b) $\mathbf{L_A=L_C=L_E=0}$ and $\mathbf{K_B=K_D=I}$

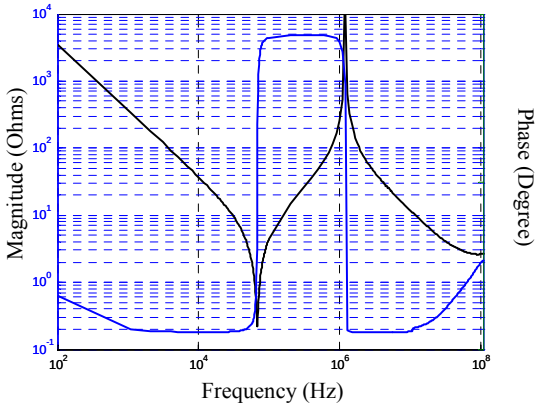

(c) $\mathbf{L_A=L_C=L_E=0}$, $\mathbf{K_B=K_D=I}$ and L_w=0

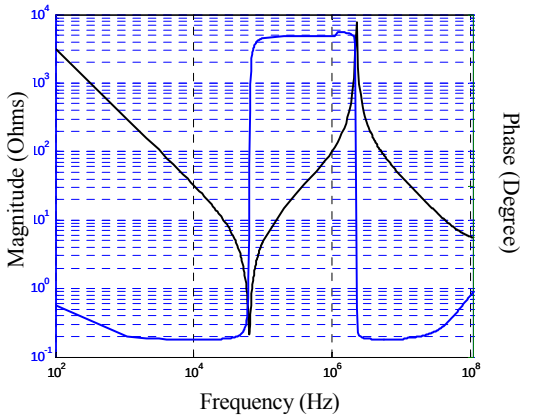

(d) $\mathbf{L_A=L_C=L_E=0}$, $\mathbf{K_B=K_D=I}$, L_w=0 and d=3mm

Figure 4-9: Changing trends of the impedance when varying parameters.

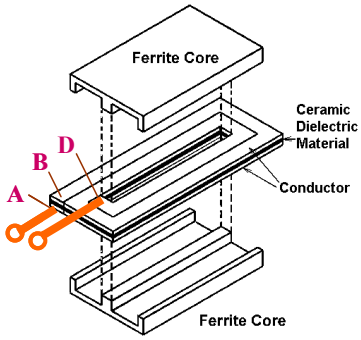

(a) External connection at the terminal AD

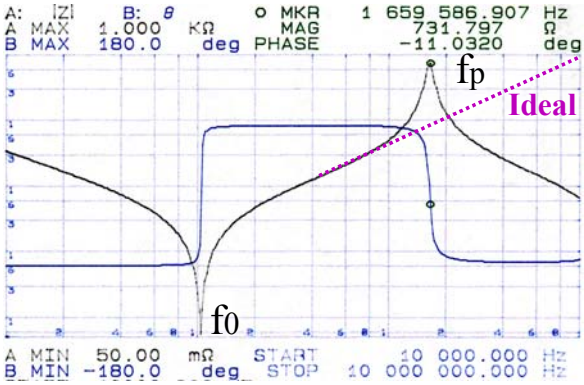

(b) Impedance test results at the terminal AD

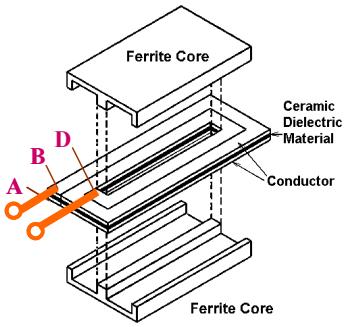

(c) External connection at the terminal BD

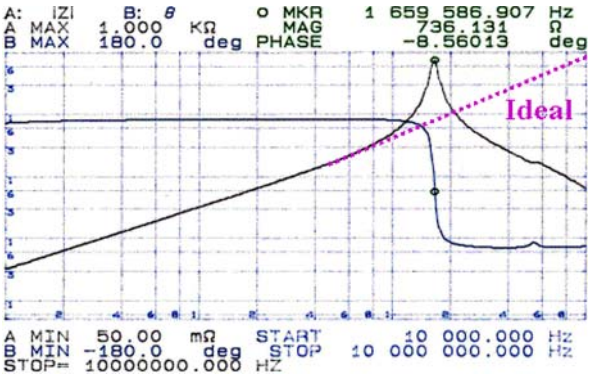

(d) Impedance test results at the terminal BD

Figure 4-10: Impedance tests across terminal AD and BD.

4.5. Conclusion

Based on the modeling of multi-conductor transmission structures in Chapter 3, this chapter presents the modeling of the conventional structure integrated series resonant module. The spiral winding of an integrated SR module can be divided into 5 sections in which only section B and D are standard multi-conductor transmission structures while the other three sections are not. An impedance transformation has been conducted to map section A, C and E into the corresponding equivalent multi-conductor transmission structures in which all the conductors in each section are in the same length. Impedance of the structure can be obtained by applying the voltage and current boundary conditions to the transmission structure equations. The calculation has been verified by small-signal measurement results. The causes of the resonance at different frequency range have been identified.

Chapter 5: Case Study: The Modeling of an Alternative Multi-cell Structure Integrated Reactive Components

5.1. Introduction

A typical structure of an integrated series resonant module based on the spiral winding technology [5][6] is shown in Figure 1-12. However, in this structure, part of the winding is outside the core leading to ineffective utilization of volume. Additionally, the spiral form copper winding on the ceramic dielectric material results in more mechanical stress concentration due to the CTE mismatch between copper and dielectric material in comparison to a linear structure. Since the ceramic substrates in an integrated resonant module are generally very thin and fragile, the mechanical stress --especially in medium and high power applications --and the insufficient mechanical protection of the overhang outside the core results in a fragile construction.

Based on the basic L-C cell (see Chapter 2), this chapter presents an alternative approach to the integration of reactive components and establishes the principles for its design and operation. A PCB-mount chip-like structure which may have the potential to be more manufacturable, modularizable and mechanically robust is proposed. Different functional equivalents can be obtained by different PCB interconnections. The experimental results confirm the functionality as integrated reactive components for applications such as high frequency resonators.

In terms of the modeling of a multi-cell structure integrated passive module, the theoretical analysis of the multi-conductor transmission structures (see Chapter 3) can be easily applied to this structure. Interconnections between cells determine the voltage and current boundary conditions with which the equations can be solved. The calculation results are verified by small-signal measurement. The influences of the stray inductance of interconnects and input leads are also discussed.

5.2. *Proposed Structure*

To overcome the disadvantages of the structure shown in Figure 1-12, an alternative structure is proposed. Development of the new structure can be explained by visualizing the evolution of an L-C cell with a magnetic core, referring to Figure 5-1(a). Through a different construction arrangement, the structure shown in Figure 5-1(b) avoids having an undesirable overhang outside the core. The evolution from Figure 5-1(c) to (d) may utilize the copper on a PCB as the interconnection. Figure 5-1(d) can be easily extended to a multi-cell structure as shown in Figure 5-1(e). The dashed lines represent the interconnections between cells. Consequently, it offers the opportunity to integrate the reactive components as a PCB-mounted, user-programmable, chip-like module. The detail of the proposed structure of the integrated module is shown in Figure 5-2.

The proposed structure has a copper-plated ceramic substrate enclosed in a planar ferrite magnetic core with interconnections essentially in the third dimension by side-straps in a dual-in-line fashion. Figure 5-2(b) shows the top view of the part inside the magnetic core. Straight copper strips are plated on both sides of a high permittivity ceramic in parallel with each other. Each pair of copper strips with the dielectric material in between form an L-C cell. Four pins are connected to each cell with two on the top copper layer and another two on the bottom copper layer. Each L-C cell is actually based on the structure shown in Figure 5-1(d) with two more pins connected to top and bottom copper layers respectively for the possible interconnections among the cells.

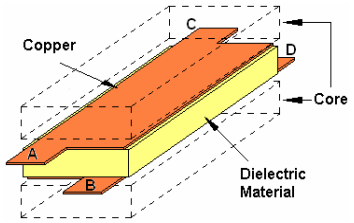

(a) An L-C cell

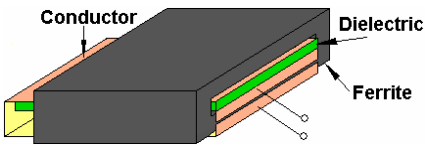

(b) Conductor folded underneath the core

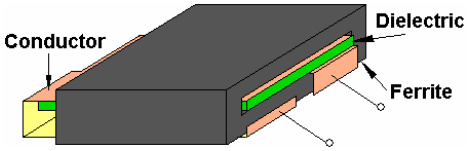

(c) Interconnections rearrangement

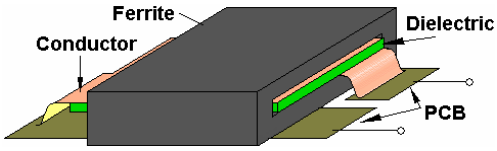

(d) Using PCB as the interconnection

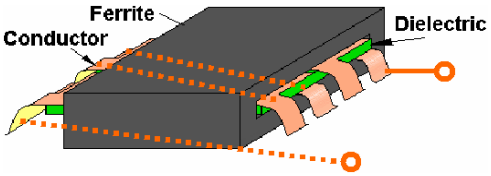

(e) Proposed structure

Figure 5-1: Conceptual evolution from an L-C cell to a new planar integrated reactive module.

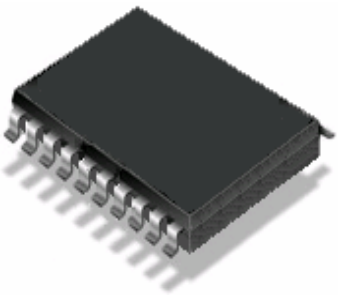

(a) External view

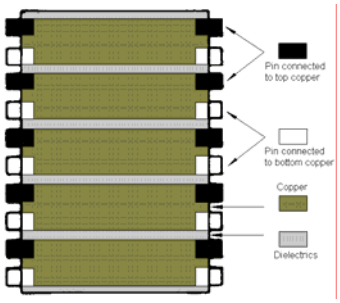

(b) Internal top view

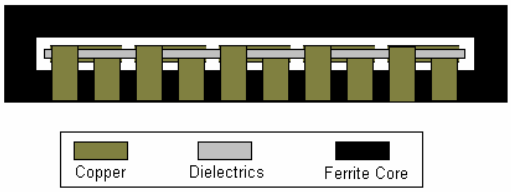

(c) Front view

Figure 5-2: Proposed structure for integrated reactive components.

5.3. *The First Order Models for Various Interconnections*

A proposed lumped equivalent circuit model for one L-C cell is shown in Figure 5-3.

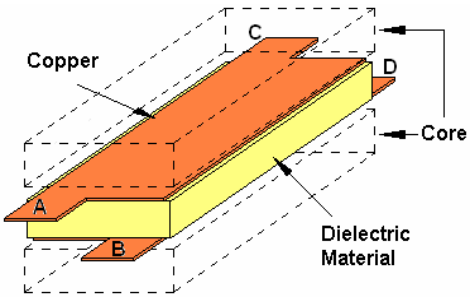

(a) An L-C cell

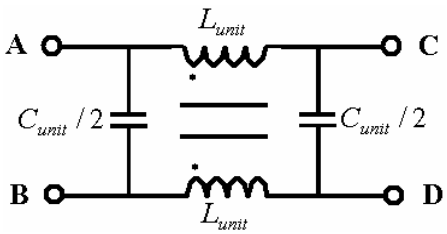

(b) The lumped model

Figure 5-3: An L-C cell and its lumped equivalent circuit model.

The inductance for an L-C cell

$$L_{unit} = \frac{\mu_0 A_e}{l_g + \frac{l_e - l_g}{\mu_r}} \text{ (H)} \tag{5-1}$$

in which, A_e= effective core area (m^2)

l_e= effective window perimeter (m)

l_g= air gap distance (m)

μ_0= permeability of vacuum ($4\pi \times 10^{-7} N/A^2$)

μ_r= relative permeability of the magnetic core

The capacitance for an L-C cell

$$C_{unit} = \frac{\varepsilon_0 \varepsilon_r A_{unit}}{h_D} \text{ (F)} \tag{5-2}$$

in which, A_{unit}= copper area for one L-C cell (m^2)

h_D= thickness of the ceramic tile (m)

ε_0= permittivity of vacuum ($8.854 \times 10^{-12} F/m$)

ε_r= relative permittivity of the dielectrics

Figure 5-4 shows some examples of the various interconnections and their equivalent circuits. The dotted lines and dashed lines represent the copper strip on the PCB completing the bottom part of the module. With different interconnections, we may achieve integrated series and parallel resonators, a low-pass filter, a resonator-transformer and an EMI filter as shown in Figure 5-4. The first approximation models and their parameter calculations are shown in Figure 5-4 as well, in which N represents the number of L-C cells in the connection.

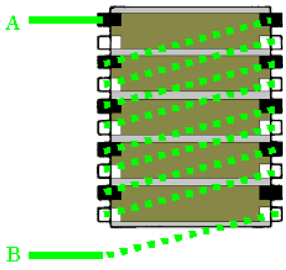

$L = N^2 L_{unit}$

$C = NC_{unit}$

(Large L, large C)

(a)

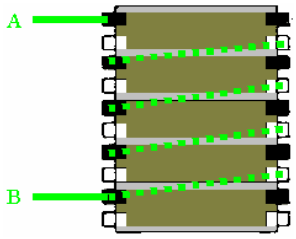

$$L = N^2 L_{unit}$$

$$C = C_{unit} / N$$

(Large L, small C)

(b)

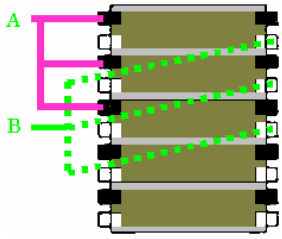

$$L = L_{unit}$$

$$C = NC_{unit}$$

(Small L, large C)

(c)

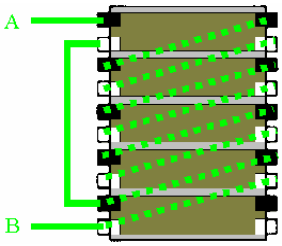

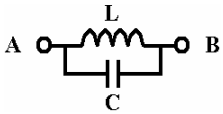

$$L = (2N)^2 L_{unit}$$

$$C = NC_{unit} / 4$$

(Large L, large C)

(d)

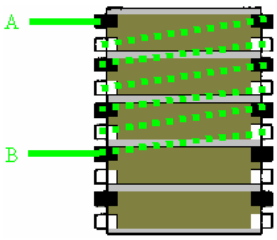

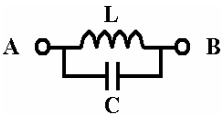

$$L = (2N)^2 L_{unit}$$

$$C = C_{unit} / 4N$$

(Large L, small C)

(e)

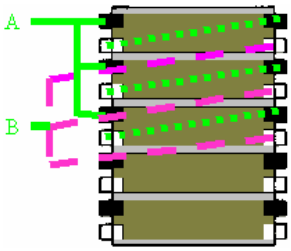

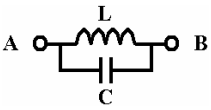

$$L = L_{unit}$$

$$C = NC_{unit} / 4$$

(Small L, large C)

(f)

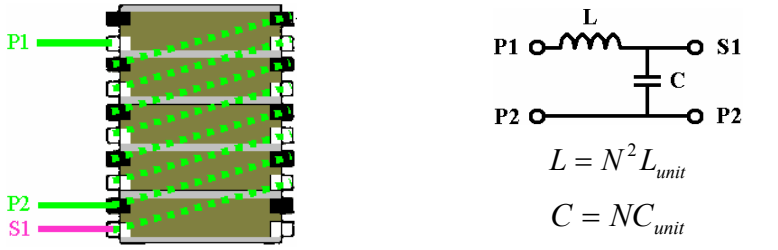

(g) Low pass filter

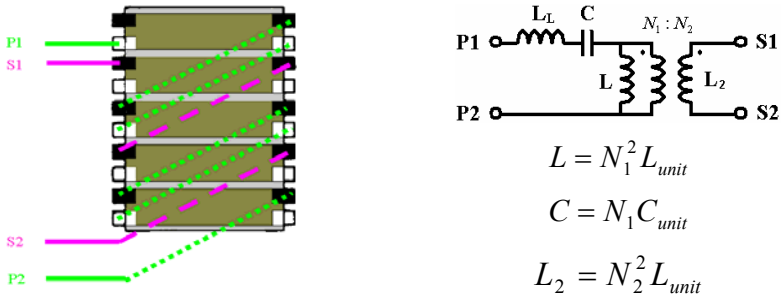

(h) Resonator-transformer

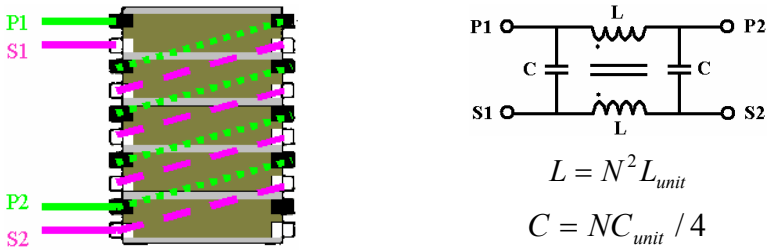

(i) EMI filter

Figure 5-4: Various interconnections with their equivalent circuits.

5.4. Design Issues

The following presents only a first order approximation in modeling the structure for an initial design. The following simplifying assumptions are made:

1). Fringing capacitance is negligible.

2). The current flow across the two skin depths of conductor is uniform.

5.4.1. Conductor Design

As a typical example, the design of a series resonant module is discussed in this section.

The resonant frequency of an LC resonant module is given by

$$f_0 = \frac{1}{2\pi\sqrt{LC}} \tag{5-3}$$

The definitions of the module dimensions are given in Figure 5-5. Taking into account the skin effect, the conductor thickness h_c is generally set to less than 2 times skin depth at resonant frequency.

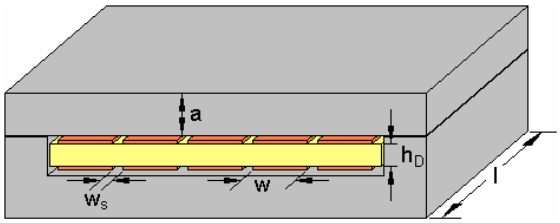

Figure 5-5: Definitions of the dimensions.

With the current density *J* fixed, the conductor width follows as

$$w = \frac{I_{rms}}{h_c J} \tag{5-4}$$

5.4.2. Dielectric Material Selection

Using dielectric material with relative permittivity ε_{rD} and thickness h_D, the conductor area needed to form the capacitance C is

$$A_D = \frac{C \cdot h_D}{\varepsilon_0 \varepsilon_{rD}} \tag{5-5}$$

5.4.3. Magnetic Core Selection

With known h_D, w, w_s and number of turns N, the minimum size core in which the windings can fit is determined. The core window width w_w should be a little larger than the width of the ceramic tile

$$w_D \approx N(w + w_s) + w_s \tag{5-6}$$

The core window height w_h must be a little higher than $2h_c+h_D$, in which h_D is the thickness of ceramic material.

From given I_{pk}, L and B_{max}, the core middle leg cross-section area

$$A_{core} = \frac{I_{pk} L}{B_{\max} N} = a \cdot l \tag{5-7}$$

in which *l* is the length of the core, *a* is the thickness of the core, as shown in Figure 5-5.

The total length of magnetic path

$$l_e = 2(w_w + w_h) + 4a \tag{5-8}$$

The air gap length

$$l_g = \frac{\frac{\mu_0 \mu_r N^2 A_{core}}{L} - l_e}{\mu_r - 1} \tag{5-9}$$

Though an air gap is currently being used in the integrated resonant module design, it should be noted that an air gap can adversely affect the field distribution, causing eddy currents, particularly with planar conductors and multi-turn windings. The solutions to the gap problem may be the use of a low-permeability magnetic material to act as a distributed gap across the top and/or the bottom of the conductors [33][34] or the so-called "quasi-distributed gap" technique [33][35].

If a design is achievable mathematically, the equation

$$A_D = N \cdot l \cdot w \tag{5-10}$$

must be satisfied. If it does not, we may vary B_{max} and J until it does.

5.5. Design Examples and Experimental Results

5.5.1. The Design Specifications

The design specifications for a series resonant module are shown in Table 5-1.

Table 5-1: Design specifications for a series resonant module

L	Inductance	30μH
C	Capacitance	77nF
I_{rms}	RMS current	2A
I_{pk}	Peak current	2.8A
f_0	Resonant frequency	104*kHz*
B_{max}	Maximum flux density	≈150mT

5.5.2. Technical Aspects of the Prototype

Based on the design equations in section 4.4, a prototype has been constructed with planar core and ceramic dielectrics. The ceramic is directly metalized by RF sputtering and subsequent electroplating the bulk of the copper layer on the ceramic. It is then

patterned and chemically etched. Its dimensions and some technical parameters are shown in Table 5-2. Figure 5-6 shows the photographs of the module.

Table 5-2: Technical parameters for the module

Magnetic core	Philips E43/10/28-3F3 and PLT43/28/4-3F3
Air gap	≈80μm
Dielectric material	Y5V
ε_r of the dielectric material	4400 (nominal)
Dimensions of the ceramic substrate	28mm×33mm×0.41mm
tanδ of the dielectric material	2% at 1MHz
Width of the copper strips	≈6mm
Copper thickness	≈50μm
Dimensions of the module	28mm×43mm×12mm

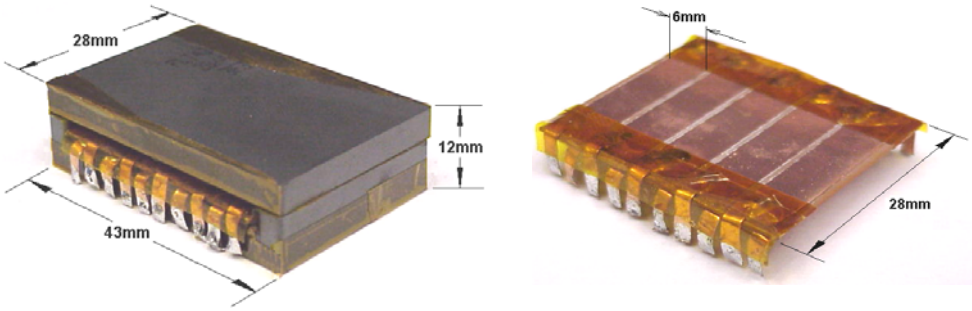

(a) External view (b) Internal view

Figure 5-6: Photographs of the prototype.

5.5.3. Test Results

5.5.3.1. Series resonance test

In order to test the series resonant characteristics, a PCB shown in Figure 5-7 is made with the interconnections given in Figure 5-4(a). The magnitude and phase characteristics with frequency are plotted in Figure 5-8, measured with an impedance analyzer HP4194A. The series resonance occurs at around 104kHz and the first parallel resonance at more than 10 times higher. The inductance and capacitance for the equivalent circuit are 30.5μH and 77.4nF that fit our calculation (30μH and 77nF) well.

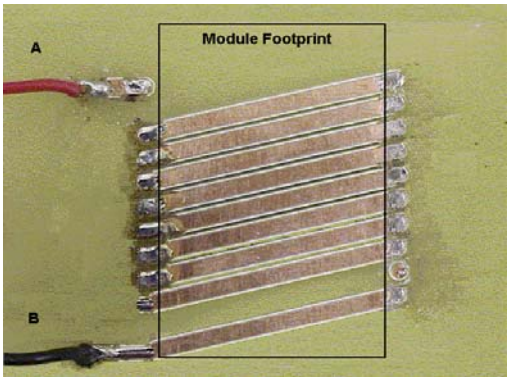

Figure 5-7: PCB for series resonance test. Input terminals AB (see Figure 5-4(a)).

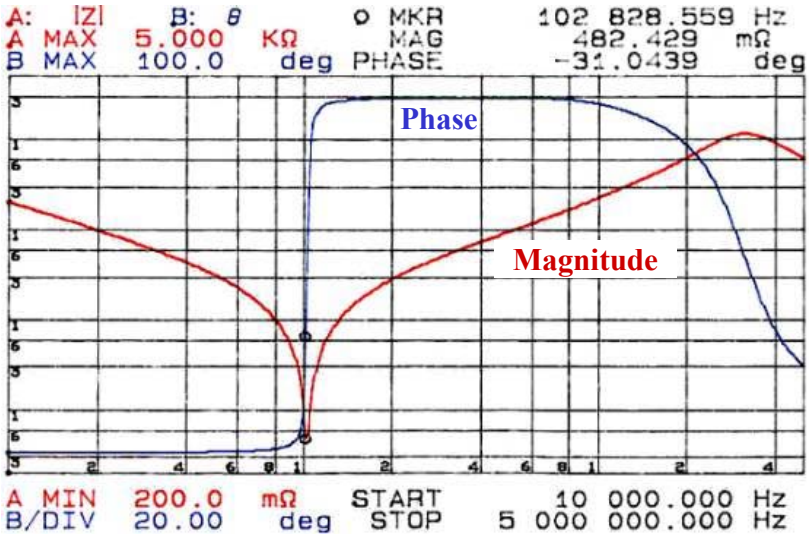

Figure 5-8: Impedance analyzer test results for series resonance.

As a power test, the module is connected as part of a half-bridge converter, as shown in Figure 5-9. The module is connected to the terminals A and B with C and D shorted. In our test, Vg is fixed at 48V.

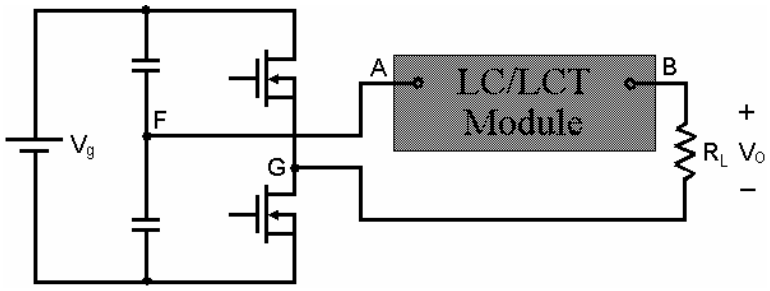

Figure 5-9: The topology of test circuit.

The voltage gain versus frequency characteristics with various load resistance RL are shown in Figure 5-10. The analytical results which are shown in solid lines are compared

with experimental results. The analytical equation is given below which is based on the first harmonic assumption [36].

$$M_n = \frac{\frac{R_L}{2(R_L + r)}}{\sqrt{1 + Q^2 (\frac{\omega}{\omega_0} + \frac{\omega_0}{\omega})^2}} \tag{5-11}$$

in which,

M_n = the normalized output voltage gain

R_L = the load resistance

r = the equivalent resistance of the total power loss in series with the module

ω = the switching frequency

ω_0 = the resonant frequency

Q = quality factor = $\omega_0 L/(R_L+r)$

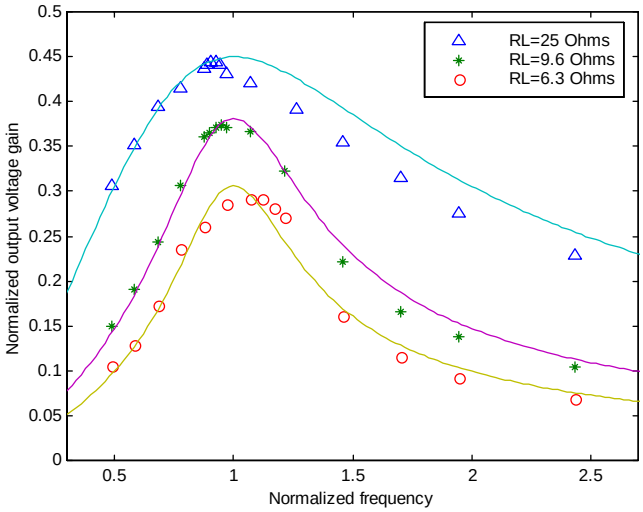

Figure 5-10: The voltage gain versus frequency characteristics with various load resistance R_L.

Figure 5-11 compares the PSPICE simulation waveforms and the experimental waveforms at RL=9.6Ω and f=100kHz. The experimental results agree well with both the analytical and simulation results. The maximum RMS and peak current flowing through the module is about 2.2A and 3.1A respectively. It can be seen that the module functions effectively as a high frequency series power resonator.

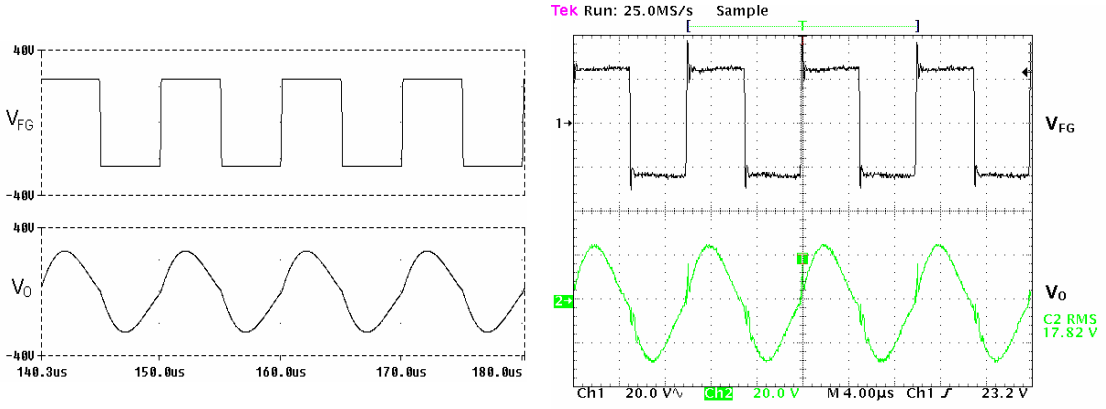

(a) PSPICE simulation waveforms (b) Experimental waveforms

Figure 5-11: V_{FG} and V_O waveforms at R_L=9.6Ω and f=100kHz.

5.5.3.2. Parallel Resonance Test

The design specifications for a parallel resonant module are given in Table 5-3.

Table 5-3: Design specifications for a parallel resonant module

L	Inductance	75µH
C	Capacitance	15nF
V_{rms}	RMS voltage	28V
V_{pk}	Peak voltage	40V
f_L	Lowest operating frequency	10kHz
f_h	Highest operating frequency	300kHz
f_0	Resonant frequency	150*kHz*
B_{max}	Maximum flux density	≈150mT

The PCB for the parallel resonance test is shown in Figure 5-12, implementing the interconnections as in Figure 5-4(d). The impedance test results are given in Figure 5-13. The inductance and capacitance for the equivalent circuit are 72µH and 15.1nF which fit our calculation (76µH and 15.4nF) well. It has a parallel resonant frequency about 150kHz with the first series resonant frequency more than 10 times higher.

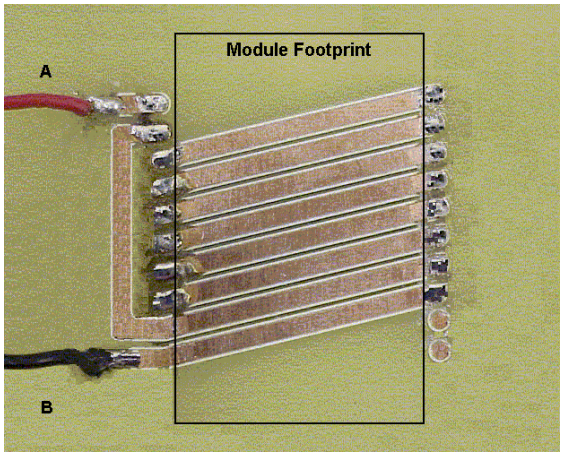

Figure 5-12: PCB for parallel resonance test. Input terminals AB (see Figure 5-4(d)).

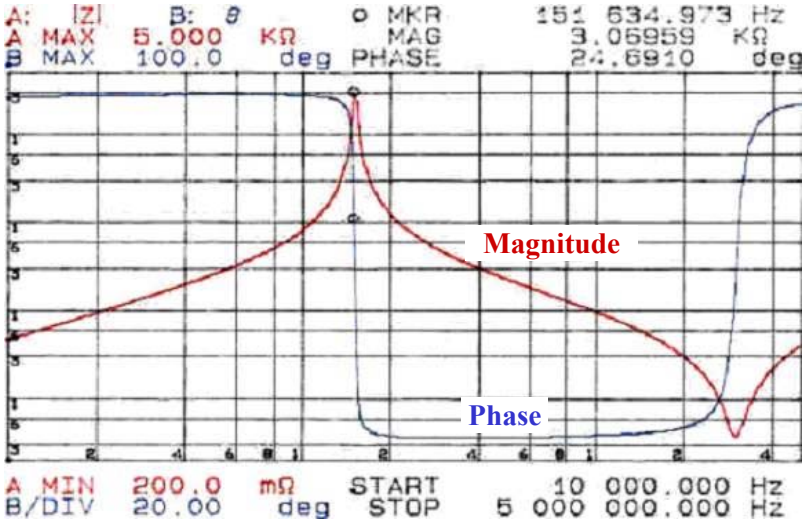

Figure 5-13: Impedance analyzer test results for parallel resonance.

Connecting the module to the terminals A and B in the test circuit with C and D shorted, the voltage gain versus frequency is shown in Figure 5-14. The experimental results are compared with PSPICE simulation results at RL=80Ω in Figure 5-15. The experimental results agree well enough with the simulation results as shown in Figure 5-14, confirming together with Figure 5-13 that the structure functions effectively as a parallel power resonator.

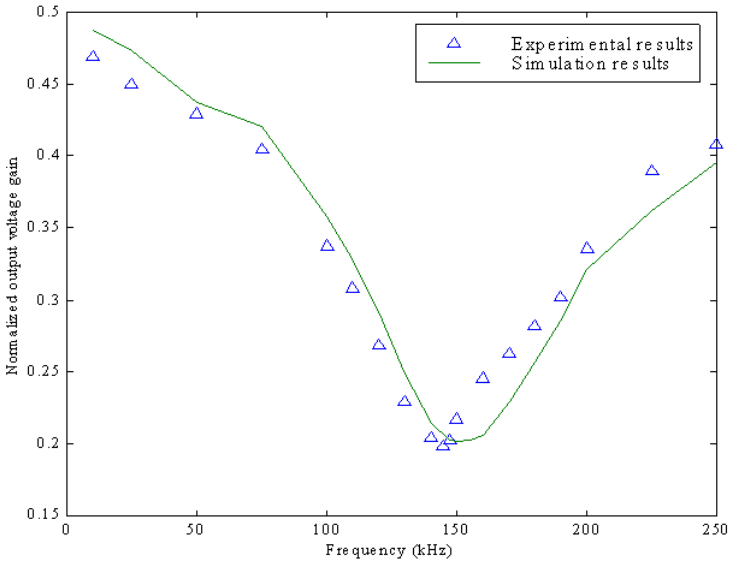

Figure 5-14: PSPICE simulation results and experimental results at R_L=80Ω..

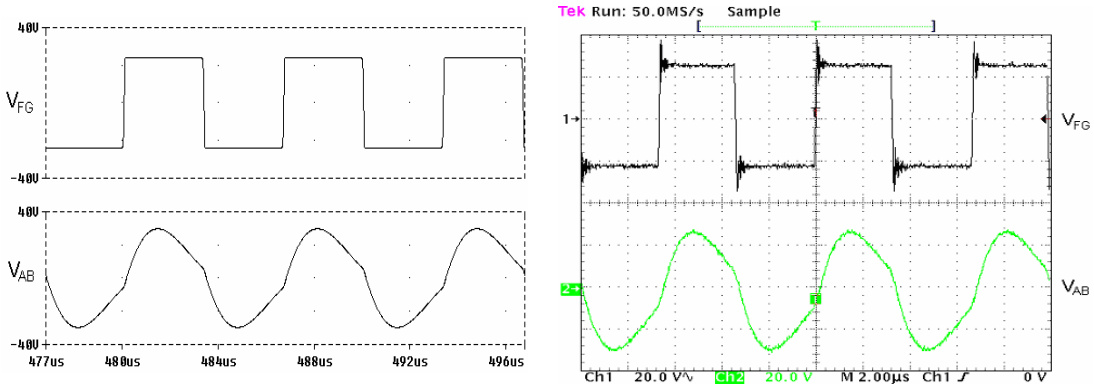

(a) PSPICE simulation waveforms. (b) Experimental waveforms.

Figure 5-15: V_{FG} and V_{AB} waveforms at R_L=9.6Ω and f=150kHz.

5.6. Generalized Modeling of a Multi-cell Integrated Series Resonator

As discussed in previous sections, various circuit functions can be obtained by different interconnections between the cells of the module. Figure 5-16 shows a typical series resonant interconnection with each conductor numbered. Normally, the interconnections are realized by copper tracks on PCB underneath the module which are represented by dotted lines in Figure 5-16. From a modeling point of view, different interconnections

just lead to different boundary conditions on which the solutions of the equations are based.

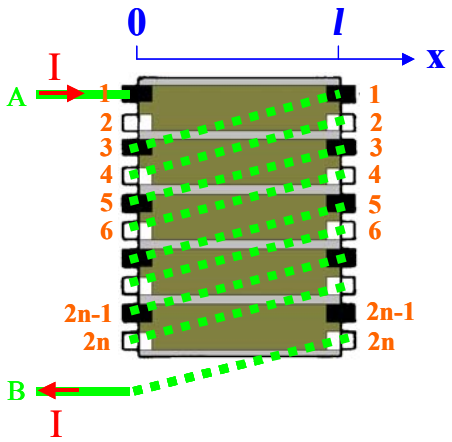

Figure 5-16: A typical series resonant interconnections.

R_{ci} and L_{ci} (i=1,2,3,4,…,2n-2) represent the resistance and inductance of each interconnection copper strip. Considering the voltage drop on the interconnections between cells, the voltage boundary conditions are given by

$$\begin{cases} V_1(l) = V_3(0) + I_3(0)(R_{c1} + j\omega L_{c1}) \\ V_2(l) = V_4(0) + I_4(0)(R_{c2} + j\omega L_{c2}) \\ V_3(l) = V_5(0) + I_5(0)(R_{c3} + j\omega L_{c3}) \\ \quad \vdots \\ V_{2n-2}(l) = V_{2n}(0) + I_{2n}(0)(R_{c2n-2} + j\omega L_{c2n-2}) \end{cases} \tag{5-12}$$

The current boundary conditions are given by

$$\begin{cases} I_1(0) = I \\ I_2(0) = 0 \\ I_1(l) = I_3(0) \\ I_2(l) = I_4(0) \\ I_3(l) = I_5(0) \\ I_4(l) = I_6(0) \\ \quad \vdots \\ I_{2n-3}(l) = I_{2n-1}(0) \\ I_{2n-2}(l) = I_{2n}(0) \\ I_{2n-1}(l) = 0 \\ I_{2n}(l) = I \end{cases} \tag{5-13}$$

From equation (3-55) and the boundary conditions given in (5-12)(5-13), it can be obtained that

$$\mathbf{D}\begin{bmatrix}\mathbf{V}(0)\\ \mathbf{I}(0)\end{bmatrix}=\mathbf{E} \tag{5-14}$$

in which,

$$\mathbf{D}=\begin{bmatrix}
\mathbf{FG}_{1,1}(l) & \mathbf{FG}_{1,2}(l) & \mathbf{FG}_{1,3}(l)-1 & \cdots & \mathbf{FG}_{1,2n}(l) & \mathbf{FG}_{1,2n+1}(l) & \mathbf{FG}_{1,2n+2}(l) & \mathbf{FG}_{1,2n+3}(l)-(R_{c1}+j\omega L_{c1}) & \cdots & \mathbf{FG}_{1,4n}(l)\\
\vdots & \vdots & \vdots & \ddots & \vdots & \vdots & \vdots & \vdots & \ddots & \vdots\\
\mathbf{FG}_{2n-2,1}(l) & \mathbf{FG}_{2n-2,2}(l) & \mathbf{FG}_{2n-2,3}(l) & \cdots & \mathbf{FG}_{2n-2,2n}(l)-1 & \mathbf{FG}_{2n-2,2n+1}(l) & \mathbf{FG}_{2n-2,2n+2}(l) & \mathbf{FG}_{2n-2,2n+3}(l) & \cdots & \mathbf{FG}_{2n-2,4n}(l)-(R_{c2n-2}+j\omega L_{c2n-2})\\
0 & 0 & 0 & \cdots & 0 & 1 & 0 & 0 & \cdots & 0\\
0 & 0 & 0 & \cdots & 0 & 0 & 1 & 0 & \cdots & 0\\
\mathbf{FG}_{2n+1,1}(l) & \mathbf{FG}_{2n+1,2}(l) & \mathbf{FG}_{2n+1,3}(l) & \cdots & \mathbf{FG}_{2n+1,2n}(l) & \mathbf{FG}_{2n+1,2n+1}(l) & \mathbf{FG}_{2n+1,2n+2}(l) & \mathbf{FG}_{2n+1,2n+3}(l)-1 & \cdots & \mathbf{FG}_{2n+1,4n}(l)\\
\vdots & \vdots & \vdots & \ddots & \vdots & \vdots & \vdots & \vdots & \ddots & \vdots\\
\mathbf{FG}_{4n-2,1}(l) & \mathbf{FG}_{4n-2,2}(l) & \mathbf{FG}_{4n-2,3}(l) & \cdots & \mathbf{FG}_{4n-2,2n}(l) & \mathbf{FG}_{4n-2,2n+1}(l) & \mathbf{FG}_{4n-2,2n+2}(l) & \mathbf{FG}_{4n-2,2n+3}(l) & \cdots & \mathbf{FG}_{4n-2,4n}(l)-1\\
\mathbf{FG}_{4n-1,1}(l) & \mathbf{FG}_{4n-1,2}(l) & \mathbf{FG}_{4n-1,3}(l) & \cdots & \mathbf{FG}_{4n-1,2n}(l) & \mathbf{FG}_{4n-1,2n+1}(l) & \mathbf{FG}_{4n-1,2n+2}(l) & \mathbf{FG}_{4n-1,2n+3}(l) & \cdots & \mathbf{FG}_{4n-1,4n}(l)\\
\mathbf{FG}_{4n,1}(l) & \mathbf{FG}_{4n,2}(l) & \mathbf{FG}_{4n,3}(l) & \cdots & \mathbf{FG}_{4n,2n}(l) & \mathbf{FG}_{4n,2n+1}(l) & \mathbf{FG}_{4n,2n+2}(l) & \mathbf{FG}_{4n,2n+3}(l) & \cdots & \mathbf{FG}_{4n,4n}(l)
\end{bmatrix} \tag{5-15}$$

$$\mathbf{E}=\begin{bmatrix}0 & \cdots & 0 & I & 0 & 0 & \cdots & 0 & 0 & I\end{bmatrix}^T \tag{5-16}$$

Thus, $\mathbf{V}(0)$ and $\mathbf{I}(0)$ can be obtained from (5-14) by

$$\begin{bmatrix}\mathbf{V}(0)\\ \mathbf{I}(0)\end{bmatrix}=\mathbf{D}^{-1}\mathbf{E} \tag{5-17}$$

When a total current I flows through the module, the voltage across A and B is given by

$$V_{AB}=\sum_{i=1}^{n}[V_{2i-1}(0)-V_{2i-1}(l)]+\sum_{i=1}^{n-1}I_{2i-1}(l)(R_{c2i-1}+j\omega L_{c2i-1})+V_{2n-1}(l)-V_{2n}(l) \tag{5-18}$$

Therefore, the total impedance Z_{AB} can be obtained as

$$Z_{AB}=V_{AB}/I \tag{5-19}$$

5.7. Case Study

A prototype of multi-cell structure integrated passive has been implemented, as shown in Figure 5-6. Its dimensions and some technical parameters are shown in Table 5-2. 3 L-C cells are involved in the test and the interconnections are illustrated in Figure 5-17.

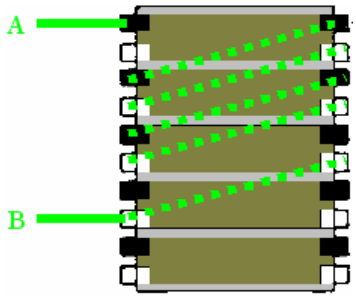

Figure 5-17: interconnections the prototype.

The determination of impedance matrix **Z** and admittance matrix **Y** are based on the inductance matrix **L** and capacitance matrix **C** which represent the magnetic and capacitive coupling between conductors, respectively. The inductance matrix is obtained from measurement while the capacitance matrix is obtained from calculation. They are given by

$$L=\begin{bmatrix} 25.3571 & 24.7500 & 21.2679 & 20.8036 & 20.1429 & 19.9821 \\ 24.7500 & 25.3571 & 20.8036 & 21.2679 & 19.9821 & 20.1429 \\ 21.2679 & 20.8036 & 25.3571 & 24.7500 & 21.2679 & 20.8036 \\ 20.8036 & 21.2679 & 24.7500 & 25.3571 & 20.8036 & 21.2679 \\ 20.1429 & 19.9821 & 21.2679 & 20.8036 & 25.3571 & 24.7500 \\ 19.9821 & 20.1429 & 20.8036 & 21.2679 & 24.7500 & 25.3571 \end{bmatrix} \mu H$$

$$C=\begin{bmatrix} 0 & 0.5000 & 0.0150 & 0 & 0 & 0 \\ 0.5000 & 0 & 0 & 0.0150 & 0 & 0 \\ 0.0150 & 0 & 0 & 0.5000 & 0.0150 & 0 \\ 0 & 0.0150 & 0.5000 & 0 & 0 & 0.0150 \\ 0 & 0 & 0.0150 & 0 & 0 & 0.5000 \\ 0 & 0 & 0 & 0.0150 & 0.5000 & 0 \end{bmatrix} \mu F$$

The MATLAB calculation results and the measurement results of its impedance characteristics are compared in Figure 5-18. The curves of calculation predict the measured impedance well with errors less than 10%.

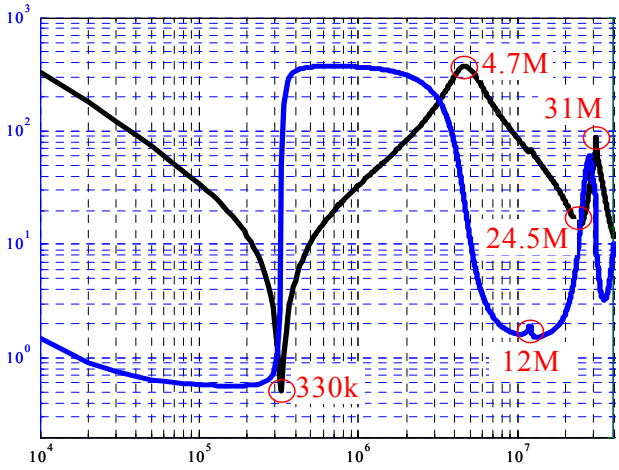

(a) Calculation results

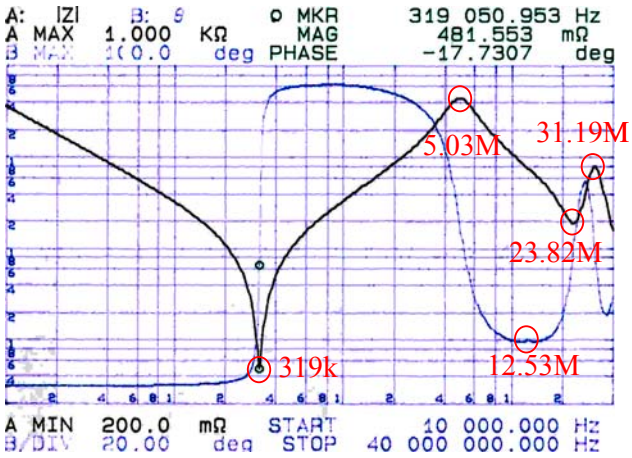

(b) Measurement results

Figure 5-18: Calculation and measurement results of the impedance of the prototype.

5.8. Discussion

A critical examination of Figure 5-10 and Figure 5-14 indicate some discrepancies between the theoretical results and the experimental results:

a) The resonant frequency under load is slightly different from the small signal measurement by impedance analyzer by less than 8%.

b) The series resonant frequency varies with the load. The resonant frequency initially is lower with the low load current and then moves to a higher frequency when the load current becomes higher and changes by approximately 15%.

c) The quality factor Q varies from 5 to 7.1, depending on the load resistance. Q decreases with increasing load current.

d) The measured results below resonance agree with the theoretical results better than those above resonance for both the series and the parallel resonator. The maximum deviation is 12%.

The reasons for these differences may be:

1) The material properties are dependent on voltage, current, frequency and temperature. For instance, the permittivity of the dielectric material and the permeability of the ferrite material as well as their loss factors vary with voltage, frequency and temperature. That may contribute to the variations of the resonant frequency and Q with R_L.

2) The equivalent resistance in calculating the quality factor Q includes all the power losses in series with the module except the load resistance. The current and frequency dependent losses associated with the switching devices and so forth should be taken into account as well.

3) The theoretical calculations are based on the first harmonic assumption [36] which becomes less valid further from the resonant frequency.

4) Experimental error is not established to be a major contributor to the differences between the models and the experimental verification. In continuation of the work it will be especially necessary to include more accurate material models.

The discussion above is also suitable for the explanation of the difference between the simulation results and the measured results in Figure 5-14.

In the calculation that plotted in Figure 5-18, the internal interconnection inductance Lc in (5-12) is estimated to be 14nH each. Figure 5-19 shows the influences of different values of Lc on the impedance curves. One of the most obvious phenomena is that the small impedance "bump" marked in Figure 5-19 moves to lower frequency with an increasing Lc.

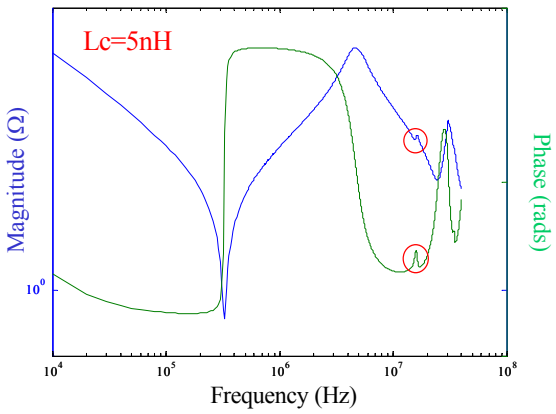

(a) Lc=5nH

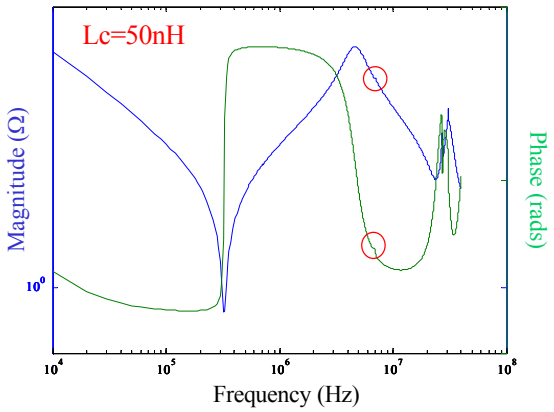

(b) Lc=50nH

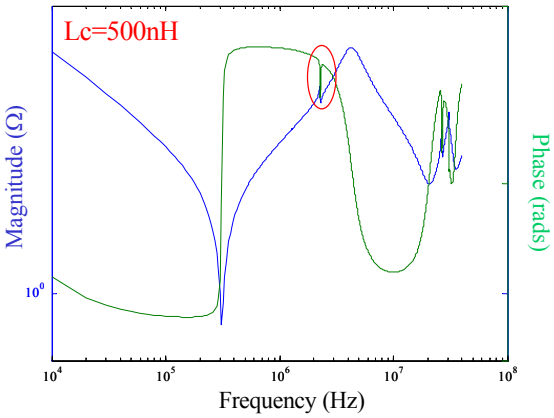

(c) Lc=500nH

Figure 5-19: Sensitivity of impedance to interconnection inductance Lc.

On the other hand, the impedance measurement is very likely to introduce some external interconnection inductance which is represented by L_w. The sensitivity of the impedance to L_w is shown in Figure 5-20. It can be seen that L_w does have an effect on high frequency impedance characteristics but does not change the position of the small "bump" shown in Figure 5-19.

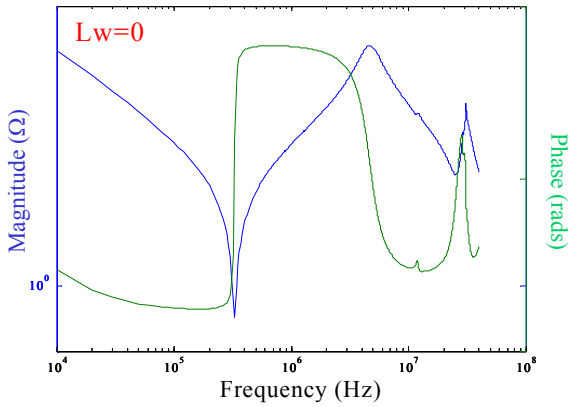

(a) Lw=0

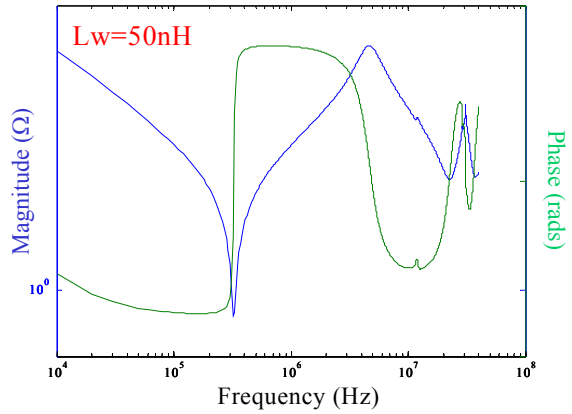

(b) Lw=50nH

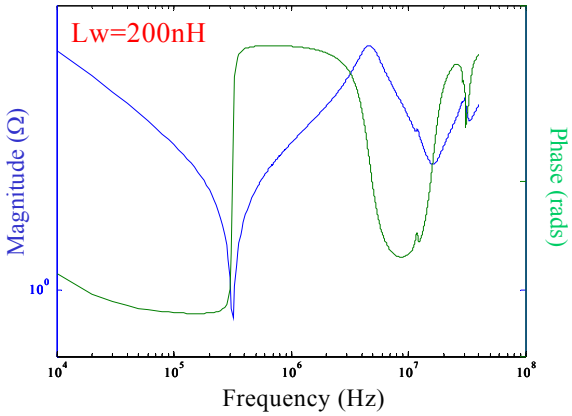

(c) Lw=200nH

Figure 5-20: Sensitivity of impedance to external interconnection inductance L_w.

5.9. Conclusion

An alternative approach for implementing an integrated power resonator module is presented, based on structural changing to some original suggestions. With a multi-cell structure, the chip-like module may be configured for different equivalent functions through different PCB interconnections. The first approximation models as well as the fundamental design formulas are presented. Some design examples are given and the test results with different interconnections fit the used model calculations adequately. Though the designs have not been optimized, it has been shown experimentally that two of these structures work as series or parallel integrated high frequency power resonators. Some advantages and potential advantages of these structures are:

1. Potentially higher power density than the previous structures due to the different active volume arrangement.

2. Better mechanical properties (less mechanical stress, better protection of the ceramic tiles, etc.).

3. Potentially improved manufacturability and modularization.

4. Multi-functionality.

5. The potential to achieve true 3-D-integrations, since the vertical dimension is used for interconnection.

This chapter also presents the impedance modeling of the multi-cell integrated passive based on the generalized multi-conductor transmission structure modal analysis. A typical integrated multi-cell series resonator has been studied as an example. The interconnections determine the voltage and current boundary conditions necessary to solve the matrix equations. The MATLAB calculation results correlate well with the measurement results. The influences of the magnitudes of interconnection inductance on the calculation results have been presented as well.

Chapter 6: Case Study: Electromagnetic Modeling of an Integrated Differential Mode RF EMI Filter

6.1. Introduction

Presently there is a move towards standard blocks of integrated power electronic modules (IPEMs), that can be connected together to perform the desired power conversion, as part of a drive to increase the power density of power electronic units. However, the increasing frequency and close proximity of active, passive and logic devices in IPEMs dramatically increases the susceptibility to RF-EMI between the various components. An integrated conducted RF-EMI power line filter to be used between IPEMs and between IPEMs and power supplies has been proposed in [22] and experimental results presented in [23].

Used as a lossy busbar feeding power to an IPEM, the filter is specifically aimed at the planar layout and interconnect technologies presently being favored in designs. As illustrated in Figure 6-1, the filter consists of two outer copper layers and an inner attenuator which is made from a high permittivity dielectric ceramic metalized on both sides with nickel. The outer conductors are separated from the nickel by a layer of insulating substrate. The two top conductors are connected at each end and the two bottom conductors are connected at each end, forming a 4-terminal device. The outside conductors are designed to carry the full load power. The attenuator is built to absorb the higher frequency components. At very low frequencies, more current is being carried by the less resistive outer conductors. As the frequency increases, the proximity effect starts to concentrate the flow towards the center of the conducting structure. This means that the current density in the nickel starts to increase. Nickel has a higher resistivity and higher relative permeability than copper. This decreases the effective conduction area and further increase the losses at high frequency.

(a) System overview

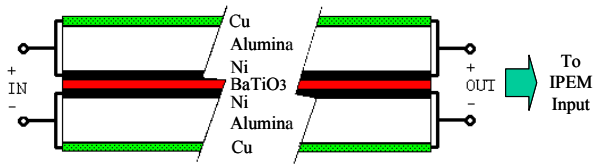

(b) The configurations of the integrated RF-EMI filter

Figure 6-1: Integrated RF-EMI filter for IPEM.

A prototype filter was built to demonstrate the feasibility of the construction processes with a two-conductor- transmission-line-based model presented [23]. However, this structure has shown some unique high frequency characteristics that could not be accurately modeled by either lumped model or two-conductor transmission-line model. On the other hand, a design-oriented model is highly desirable aiming to improve the filter module design. Based on generalized multi-conductor transmission structure theory [37], this paper presents the electromagnetic modeling of an integrated RF EMI filter. The measured performance of the prototype is compared with the calculation results. Some useful conclusions have been drawn to further facilitate the integrated RF EMI filter design.

6.2. Multi-conductor Generalized Transmission Structure Modeling of the Filter

6.2.1. The Preliminary Model Based on Multi-conductor Generalized Transmission Structure

Generalized multi-conductor transmission structure theory has been applied to the modeling of integrated passive components [37] and can be applied to that of the integrated RF-EMI filter as well. The structure in Figure 6-1 can be treated as four parallel conductors with magnetic and capacitive coupling with each other, as shown in Figure 6-2. The total length of the structure is *l*. Conductor 1 and conductor 2 are connected at each end, as well as conductor 3 and 4.

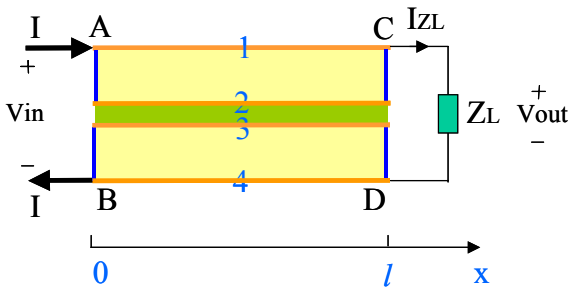

Figure 6-2: 4-conductor model of the integrated RF-EMI filter.

The voltage and current equations presenting in a matrix form are given by

$$\begin{cases} -\dfrac{d}{dx}\mathbf{V} = \mathbf{ZI} \\ -\dfrac{d}{dx}\mathbf{I} = \mathbf{YV} \end{cases} \tag{6-1}$$

in which,

$$\mathbf{Z} = \begin{bmatrix} R_1 + j\omega L_1 & j\omega M_{1,2} & j\omega M_{1,3} & j\omega M_{1,4} \\ j\omega M_{2,1} & R_2 + j\omega L_2 & j\omega M_{2,3} & j\omega M_{2,4} \\ j\omega M_{3,1} & j\omega M_{3,2} & R_3 + j\omega L_3 & j\omega M_{3,4} \\ j\omega M_{4,1} & j\omega M_{4,2} & j\omega M_{4,3} & R_4 + j\omega L_4 \end{bmatrix} \tag{6-2}$$

$$\mathbf{Y} = \begin{bmatrix} G_{1,2} + j\omega C_{1,2} & -(G_{1,2} + j\omega C_{1,2}) & 0 & 0 \\ -(G_{1,2} + j\omega C_{1,2}) & G_{1,2} + j\omega C_{1,2} + G_{2,3} + j\omega C_{2,3} & -(G_{2,3} + j\omega C_{2,3}) & 0 \\ 0 & -(G_{2,3} + j\omega C_{2,3}) & G_{2,3} + j\omega C_{2,3} + G_{3,4} + j\omega C_{3,4} & -(G_{3,4} + j\omega C_{3,4}) \\ 0 & 0 & -(G_{3,4} + j\omega C_{3,4}) & G_{3,4} + j\omega C_{3,4} \end{bmatrix} \tag{6-3}$$

$$\mathbf{V} = \begin{bmatrix} V_1 & V_2 & V_3 & V_4 \end{bmatrix}^T \tag{6-4}$$

$$\mathbf{I} = \begin{bmatrix} I_1 & I_2 & I_3 & I_4 \end{bmatrix}^T \tag{6-5}$$

Through matrix manipulations [3], **V**(x) and **I**(x) can be determined in terms of **V**(0) and **I**(0).

$$\begin{bmatrix} \mathbf{V}(x) \\ \mathbf{I}(x) \end{bmatrix} = \begin{bmatrix} \mathbf{F_V}(x) & \mathbf{G_V}(x) \\ \mathbf{F_I}(x) & \mathbf{G_I}(x) \end{bmatrix} \begin{bmatrix} \mathbf{V}(0) \\ \mathbf{I}(0) \end{bmatrix} = \mathbf{FG}(x) \cdot \begin{bmatrix} \mathbf{V}(0) \\ \mathbf{I}(0) \end{bmatrix} \tag{6-6}$$

Assuming Vin=$V_2(0)$-$V_3(0)$=1, the voltage and current boundary conditions can be given by

$$\begin{cases} V_2(l) - V_3(l) - Z_L\left[I_1(l) + I_2(l)\right] = 0 \\ V_1(0) - V_2(0) = 0 \\ V_1(l) - V_2(l) = 0 \\ V_3(0) - V_4(0) = 0 \\ V_3(l) - V_4(l) = 0 \\ I_1(0) + I_2(0) + I_3(0) + I_4(0) = 0 \\ I_1(l) + I_2(l) + I_3(l) + I_4(l) = 0 \\ V_2(0) - V_3(0) = 1 \end{cases} \tag{6-7}$$

or

$$\mathbf{D}\begin{bmatrix} \mathbf{V}(0) \\ \mathbf{I}(0) \end{bmatrix} = \mathbf{E} \tag{6-8}$$

in which,

$$\mathbf{D} = \begin{bmatrix} FG_{2,:}(l) - FG_{3,:}(l) - Z_L[FG_{5,:}(l) + FG_{6,:}(l)] \\ 1 \quad -1 \quad 0 \quad 0 \quad 0 \quad 0 \quad 0 \quad 0 \\ FG_{1,:}(l) - FG_{2,:}(l) \\ 0 \quad 0 \quad 1 \quad -1 \quad 0 \quad 0 \quad 0 \quad 0 \\ FG_{3,:}(l) - FG_{4,:}(l) \\ 0 \quad 0 \quad 0 \quad 0 \quad 1 \quad 1 \quad 1 \quad 1 \\ FG_{5,:}(l) + FG_{6,:}(l) + FG_{7,:}(l) + FG_{8,:}(l) \\ 0 \quad 1 \quad -1 \quad 0 \quad 0 \quad 0 \quad 0 \quad 0 \end{bmatrix} \tag{6-9}$$

$$\mathbf{E} = \begin{bmatrix} 0 & 0 & 0 & 0 & 0 & 0 & 0 & 1 \end{bmatrix}^T \tag{6-10}$$

The transfer gain of the filter can be obtained as

$$M_V = \frac{V_{out}}{V_{in}} = \frac{V_2(l) - V_3(l)}{V_2(0) - V_3(0)} = V_2(l) - V_3(l) \tag{6-11}$$

6.2.2. Improved Model Considering Measurement Issues

The measurement setup of the transfer gain with an impedance analyzer HP4194A is shown in Figure 6-3(a). However, the input and output terminals share the same ground as illustrated in Figure 6-3(b), thus the measurement results do not reflect the real transfer gain.

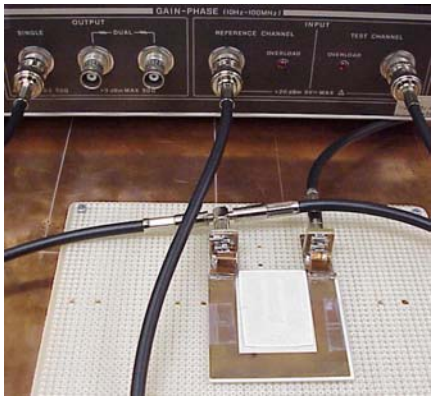

(a) Connections to the impedance analyzer

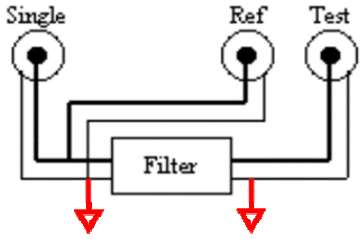

(b) Equivalent connections

Figure 6-3: Measurement setup

To evaluate the discrepancy it results in, an improved model which includes the ground impedance has been proposed, as shown in Figure 6-4. As a matter of fact, the previous model is just a special case of this more generalized model when Z_g is open-circuited. After changing the model, equations (6-1)-(6-5) still apply but with new boundary conditions.

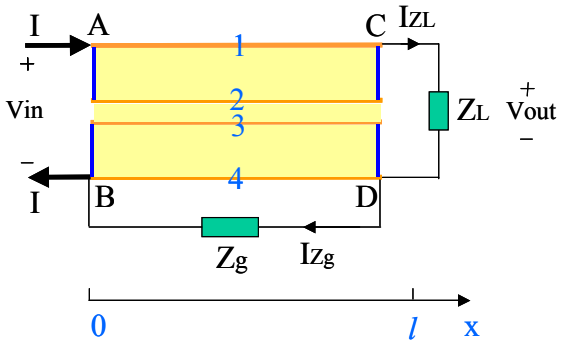

Figure 6-4: The improved model.

The voltage and current boundary conditions for the improved model are given by

$$\begin{cases} V_2(l)-V_3(l)-Z_L\left[I_1(l)+I_2(l)\right]=0 \\ V_1(0)-V_2(0)=0 \\ V_1(l)-V_2(l)=0 \\ V_3(0)-V_4(0)=0 \\ V_3(l)-V_4(l)=0 \\ V_3(l)-V_3(0)-Z_g[I_1(0)+I_2(0)+I_3(0)+I_4(0)]=0 \\ V_3(l)-V_3(0)-Z_g[I_1(l)+I_2(l)+I_3(l)+I_4(l)]=0 \\ V_2(0)-V_3(0)=1 \end{cases} \tag{6-12}$$

or

$$\mathbf{D}\begin{bmatrix}\mathbf{V}(0)\\ \mathbf{I}(0)\end{bmatrix}=\mathbf{E} \tag{6-13}$$

in which,

$$FGK1=FG_{2,:}(l)-FG_{3,:}(l)-Z_L[FG_{5,:}(l)+FG_{6,:}(l)] \tag{6-14}$$

$$FGK7=FG_{3,:}(l)-Z_g[FG_{5,:}(l)+FG_{6,:}(l)+FG_{7,:}(l)+FG_{8,:}(l)] \tag{6-15}$$

$$\mathbf{E}=\begin{bmatrix}0 & 0 & 0 & 0 & 0 & 0 & 0 & 1\end{bmatrix}^T \tag{6-16}$$

$$\mathbf{D}=\begin{bmatrix} FGK1_{1,1} & FGK1_{1,2} & FGK1_{1,3} & FGK1_{1,4} & FGK1_{1,5} & FGK1_{1,6} & FGK1_{1,7} & FGK1_{1,8} \\ 1 & -1 & 0 & 0 & 0 & 0 & 0 & 0 \\ FG_{1,1}(l)-FG_{2,1}(l) & FG_{1,2}(l)-FG_{2,2}(l) & FG_{1,3}(l)-FG_{2,3}(l) & FG_{1,4}(l)-FG_{2,4}(l) & FG_{1,5}(l)-FG_{2,5}(l) & FG_{1,6}(l)-FG_{2,6}(l) & FG_{1,7}(l)-FG_{2,7}(l) & FG_{1,8}(l)-FG_{2,8}(l) \\ 0 & 0 & 1 & -1 & 0 & 0 & 0 & 0 \\ FG_{3,1}(l)-FG_{4,1}(l) & FG_{3,2}(l)-FG_{4,2}(l) & FG_{3,3}(l)-FG_{4,3}(l) & FG_{3,4}(l)-FG_{4,4}(l) & FG_{3,5}(l)-FG_{4,5}(l) & FG_{3,6}(l)-FG_{4,6}(l) & FG_{3,7}(l)-FG_{4,7}(l) & FG_{3,8}(l)-FG_{4,8}(l) \\ FG_{3,1}(l) & FG_{3,2}(l) & FG_{3,3}(l)-1 & FG_{3,4}(l) & FG_{3,5}(l)-Z_g & FG_{3,6}(l)-Z_g & FG_{3,7}(l)-Z_g & FG_{3,8}(l)-Z_g \\ FGK7_{1,1} & FGK7_{1,2} & FGK7_{1,3}-1 & FGK7_{1,4} & FGK7_{1,5} & FGK7_{1,6} & FGK7_{1,7} & FGK7_{1,8} \\ 0 & 1 & -1 & 0 & 0 & 0 & 0 & 0 \end{bmatrix} \tag{6-17}$$

6.2.3. Loss Modeling

The loss modeling is one of the key challenges of the modeling of the entire electromagnetic characteristics. On one hand, each conductor has losses due to the skin effect of itself. On the other hand, it experiences additional losses due to the influence of its neighbours' high frequency magnetic fields, as shown in Figure 6-5.

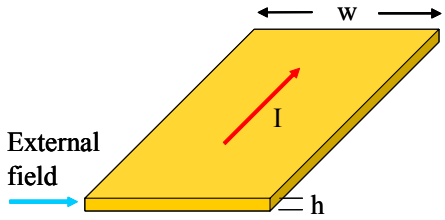

Figure 6-5: A conductor foil with external magnetic field

Based on the one-dimensional assumption, there is inherent orthogonality existing between the skin and proximity effects [38]. The total losses of one conductor can be written as:

$$P = R_{dc} \cdot \frac{\xi}{2}\left[\frac{\sinh\xi + \sin\xi}{\cosh\xi - \cos\xi} I^2 + 4w^2 \frac{\sinh\xi - \sin\xi}{\cosh\xi + \cos\xi} H_e^{\,2}\right] \tag{6-18}$$

in which,

$$\xi = \frac{h}{\delta} \tag{6-19}$$

in which h is the thickness of the conductor sheet and δ is the skin depth.

It is important to note that equation (6-18) equals the sum of the independent solutions for skin effect and the proximity effect, one for an isolated foil conductor and the other for a single foil subject to a uniform magnetic field H_e. In this application, each external field is generated by the current in another conductor. Therefore, (6-18) can be rewritten as:

$$P = FI^2 + GH_e^{\,2} = FI^2 + G'I_e^{\,2} \tag{6-20}$$

Consequently, the losses along each conduction path can be modeled as four resistances: one representing the skin effect losses of the conductor itself and the other three related to the current in the other three conductors, respectively, as shown in Figure 6-6.

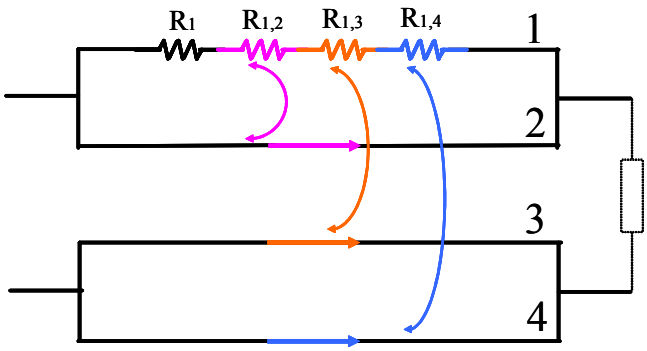

Figure 6-6: Self and mutual resistance at one conduction path.

6.2.4. Modeling of the Inductive Couplings

Considering the inductive couplings between the conductors (without considering the mutual resistances), this four-conductor structure can be modeled as in Figure 6-7(a). At

high frequencies, proximity effect starts to take hold and influence the patterns of current flow, which enhances the high frequency attenuation. Since conductor 1 and 2 (also conductor 3 and 4) are connected at both ends and forms a conductor loop, the current in the other two conductors will induce voltage in the loop thus change the current distribution in the two conductors. A simplified approach to model this proximity effect is adding another two mutual inductances at each conductor loop, representing the corresponding induced voltages by the other two conductors. To be fit into the existing model, each added mutual inductance can be split into two equal mutual inductances on different conductor paths of each loop, as shown in Figure 6-7(b). For example, $M_{a,3}$ (H/m) represents half of the mutual inductance between conductor 3 and the loop a formed by conductor 1 and 2.

As a result, the **Z** matrix in (1) and (2) changes to

$$\mathbf{Z}=\begin{bmatrix} R_1+j\omega L_1 & R_{1,2}+j\omega M_{1,2} & R_{1,3}+j\omega(M_{1,3}-M_{a,3}) & R_{1,4}+j\omega(M_{1,4}-M_{a,4}) \\ R_{2,1}+j\omega M_{2,1} & R_2+j\omega L_2 & R_{2,3}+j\omega(M_{2,3}+M_{a,3}) & R_{2,4}+j\omega(M_{2,4}+M_{a,4}) \\ R_{3,1}+j\omega(M_{3,1}+M_{b,1}) & R_{3,2}+j\omega(M_{3,2}+M_{b,2}) & R_3+j\omega L_3 & R_{3,4}+j\omega M_{3,4} \\ R_{4,1}+j\omega(M_{4,1}-M_{b,1}) & R_{4,2}+j\omega(M_{4,2}-M_{b,2}) & R_{4,3}+j\omega M_{4,3} & R_4+j\omega L_4 \end{bmatrix} \quad (6\text{-}21)$$

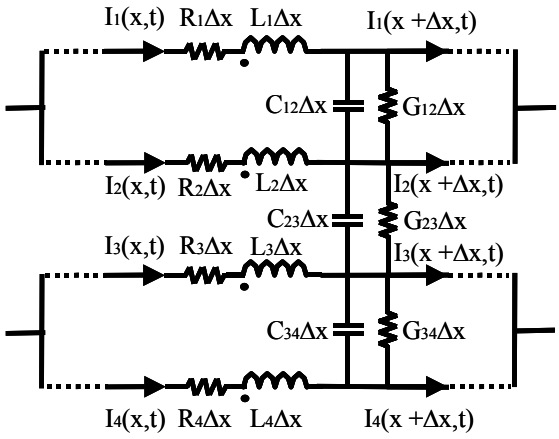

(a) Model without considering proximity effect

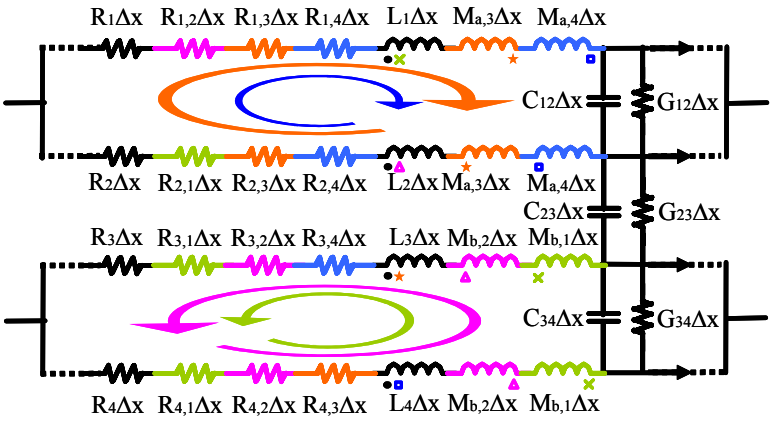

(b) (b) Model with proximity effect considerations

Figure 6-7: Model improvement with proximity effect taken into account (an infinitesimal length).

6.3. Case Study

6.3.1. The Prototype

The picture and dimensions of the prototype of an integrated RF-EMI filter [22] is shown in Figure 6-8.

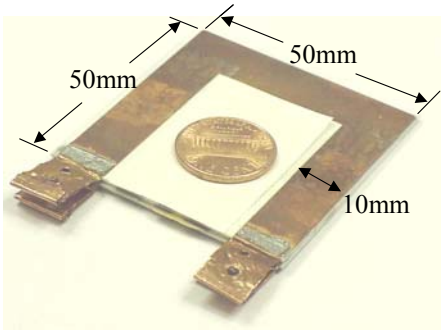

(a) Prototype picture

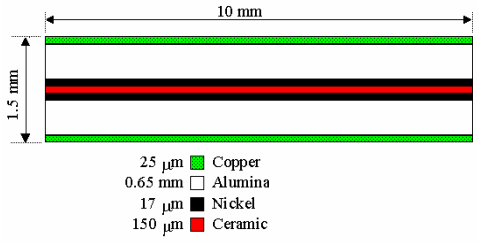

(b) Cross-sectional view and dimensions

Figure 6-8: The prototype of an integrated RF EMI filter.

Some technical parameters are shown in Table 6-1.

Table 6-1: Technical parameters of the RF-EMI filter prototype

Ceramic dielectric material (middle layer)	Y5V ($BaTiO_3$)
ε_r of the dielectric material (middle layer)	14000 (nominal)
Thickness of the dielectric material (middle layer) h_{BaTiO3}	0.15mm
Loss factor of the $BaTiO_3$ layer $\tan\delta_1$	1%
Thickness of the Alumina layer $h_{Alumina}$	0.65mm
ε_r of Alumina	9.9
Loss factor of Alumina $\tan\delta_2$	0.01%
Copper layer thickness	≈ 25μm
Nickel layer thickness	≈ 17μm
Conductor Width w	10mm
Total length of the structure	130mm

6.3.2. Parameters Calculations and Extractions

The inductance matrix used in our calculation is obtained by MAXWELL Q3D simulation. The simulation results are given below with the simulation model shown in Figure 6-9.

$$L_0 = \begin{bmatrix} L_1 & M_{1,2} & M_{1,3} & M_{1,4} \\ M_{2,1} & L_2 & M_{2,3} & M_{2,3} \\ M_{3,1} & M_{3,2} & L_3 & M_{3,4} \\ M_{4,1} & M_{4,2} & M_{4,3} & L_4 \end{bmatrix} = \begin{bmatrix} 93.227 & 76.887 & 59.941 & 54.334 \\ 76.887 & 109.41 & 81.857 & 61.292 \\ 59.941 & 81.857 & 118.63 & 79.464 \\ 54.334 & 61.292 & 79.464 & 96.279 \end{bmatrix} (nH) \qquad (6\text{-}22)$$

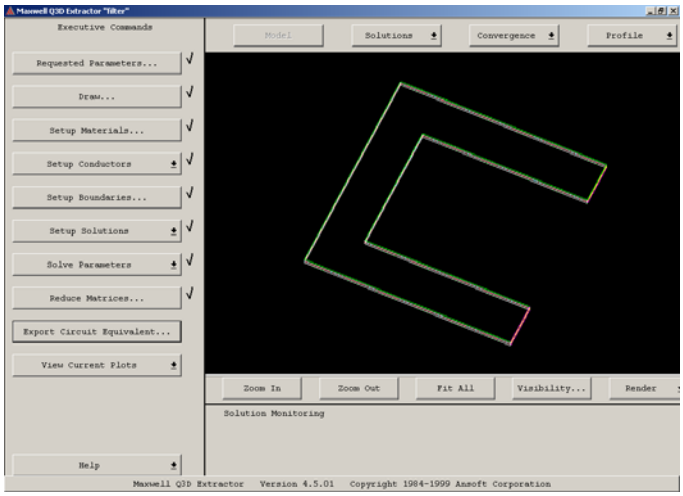

Figure 6-9: MAXWELL Q3D model for inductance matrix extraction.

However, the inductance of the nickel layers change significantly with frequency though those of the copper layers do not change much according to the measurement results. Figure 6-10 shows the variation of the self-inductance of a nickel layer with frequency. With the help of curve-fitting and assumption of unchanged coupling coefficients between conductors, the frequency-dependent inductance matrix can be figured out.

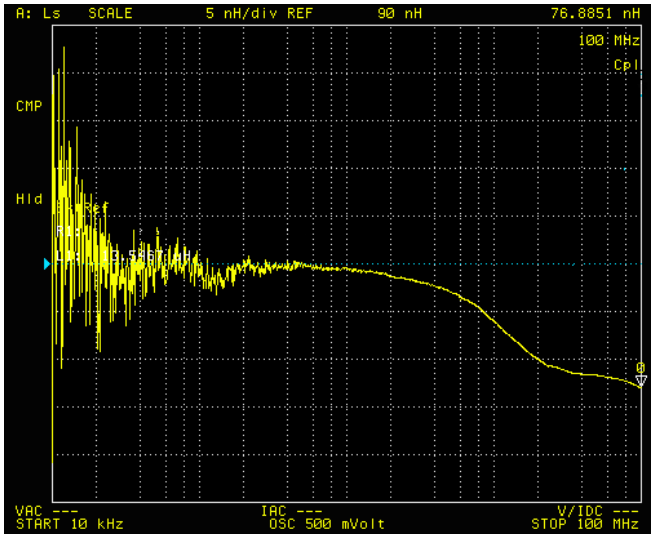

Figure 6-10: Inductance of a nickel layer as a function of frequency.

The four mutual inductances shown in Figure 6-7 are obtained by MAXWELL 2D field simulation.

$$M_{a,3} = M_{b,2} = 28.925nH \tag{6-23}$$

$$M_{a,4} = M_{b,1} = 12.805nH \tag{6-24}$$

Neglecting the fringing effect, the capacitance matrix is given by

$$C = \begin{bmatrix} 0 & C_{12} & 0 & 0 \\ C_{21} & 0 & C_{23} & 0 \\ 0 & C_{32} & 0 & C_{34} \\ 0 & 0 & C_{43} & 0 \end{bmatrix} \tag{6-25}$$

in which the capacitances can be obtained by

$$C_{12} = C_{21} = C_{34} = C_{43} = \frac{\varepsilon_0 \varepsilon_{Alu\min a} w}{h_{Alu\min a}} (F/m) \tag{6-26}$$

$$C_{23} = C_{32} = \frac{\varepsilon_0 \varepsilon_{BaTiO3} w}{h_{BaTiO3}} (F/m) \tag{6-27}$$

However, capacitance may also be a function of frequency. Figure 6-11 shows measurement results of the capacitance of a copper-plated ceramic dielectric tile. The measurement result demonstrates that the relative permittivity of the ceramic material drops from about 14000 at 40Hz to about 6000 at 110MHz.

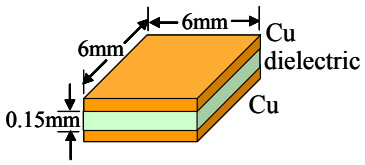

(a) The dimension of the sample

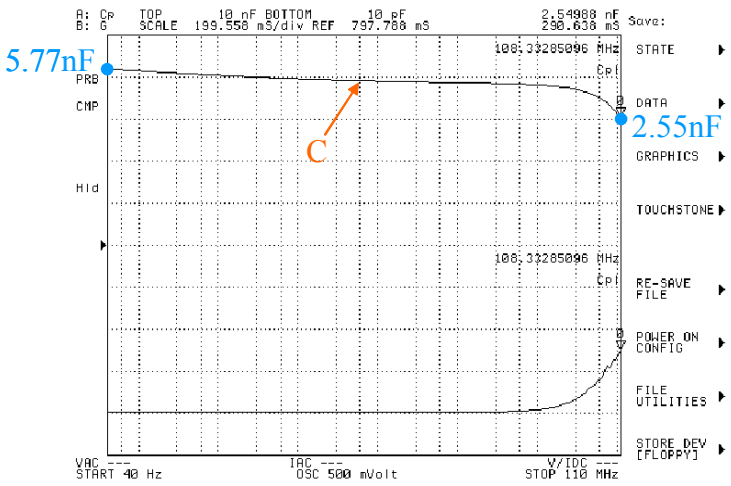

(b) Capacitance vs frequency measurement result

Figure 6-11: The ceramic dielectric material permittivity measurement sample and results.

The conductance matrix is obtained directly from the capacitances using loss factors given in Table I.

$$G = \begin{bmatrix} 0 & G_{12} & 0 & 0 \\ G_{21} & 0 & G_{23} & 0 \\ 0 & G_{32} & 0 & G_{34} \\ 0 & 0 & G_{43} & 0 \end{bmatrix} \tag{6-28}$$

in which the capacitances can be obtained by

$$G_{12}(f) = G_{21}(f) = G_{34}(f) = G_{43}(f) = \omega \cdot C_{12} \cdot \tan \delta_2 \,(\text{S/m}) \tag{6-29}$$

$$G_{23}(f) = G_{32}(f) = \omega \cdot C_{23} \cdot \tan \delta_1 \,(\text{S/m}) \tag{6-30}$$

6.3.3. Calculation Results and Measurement Results

The measured transfer gain with the standard 50 Ω impedance as the load is shown in Figure 6-12. Preliminary calculation results based on the proposed model are shown in Figure 6-13. Compared to the previous model [23], the model proposed in this paper shows remarkable improvements predicting the resonant points and the overall trend. However, there is still significant discrepancy in terms of the high frequency damping. This is due to the simplified loss assumptions that have been used.

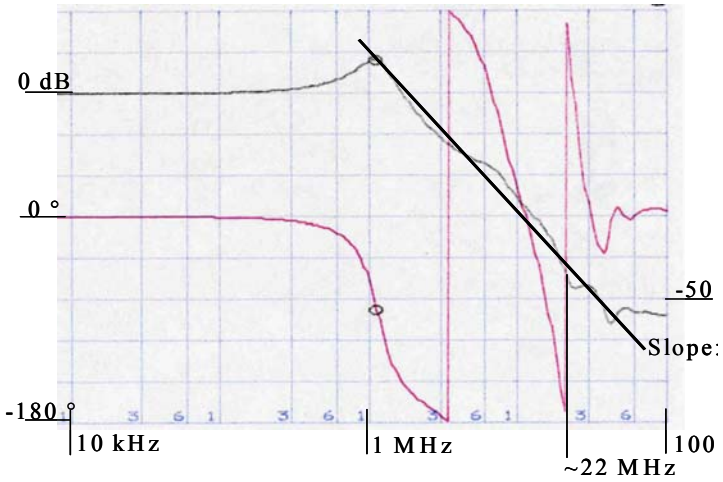

Figure 6-12: Measurement results of transfer gain at Z_L=50Ω.

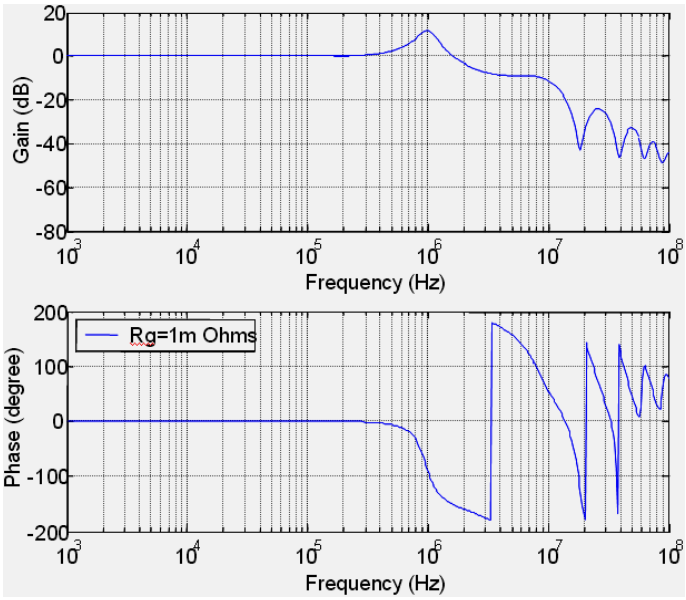

Figure 6-13: Calculation results

6.4. Discussion

As discussed in section II, the measurement setup having been used cannot obtain the real transfer gain. Setting the impedance of Z_g to nearly open-circuited and short-circuited in the model shown in Figure 6-4, the difference caused by the measurement can be calculated, as plotted in Figure 6-14. One obvious difference is that the first resonant frequency shifts to a higher frequency with the common-ground measurement. Although the discrepancy is rather insignificant for this particular module, study has shown that it could be more significant when the inductances are higher.

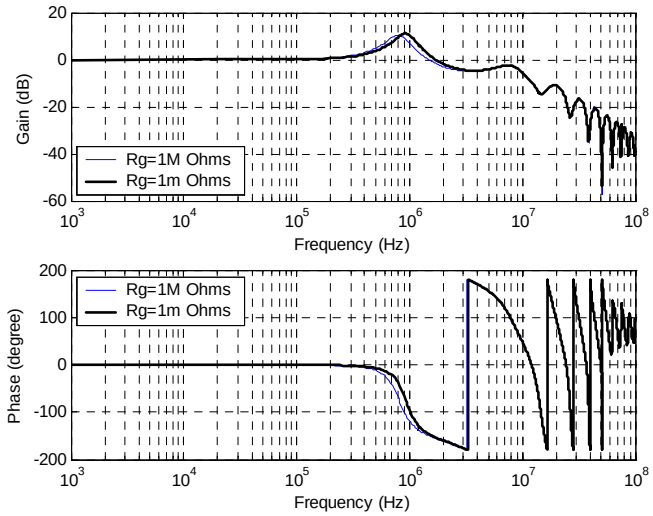

Figure 6-14: Difference made by common-ground measurement setup.

Proximity effect has been taken into account in the proposed model. An apparent effect of the added magnetic coupling between conductors and loops is the decrease of the current in the outer conductors while increasing the current in the inner conductors. This effect not only influences the attenuation but also shifts the resonant points, as compared in Figure 6-13 and Figure 6-15.

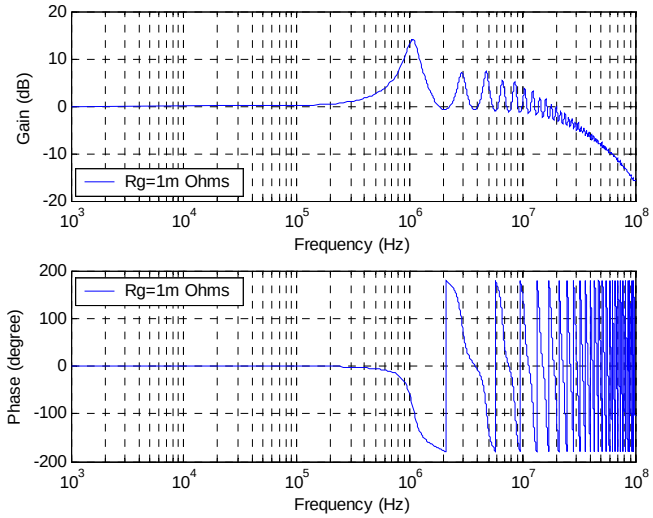

Figure 6-15: Calculation results without considering proximity effects.

The FEM simulation results given in Figure 6-16 show that current crowding occurs at the Nickel-$BaTiO_3$ interface at high frequencies. Meanwhile, the current flows in both copper and nickel layers concentrate more and more to the edges with an increasing frequency. These may significantly reduce the accuracy of the high frequency losses calculation based on equation (6-18). Another method could be curves fitting of the FEM simulation results, which is expected to be more accurate but takes much longer simulation time.

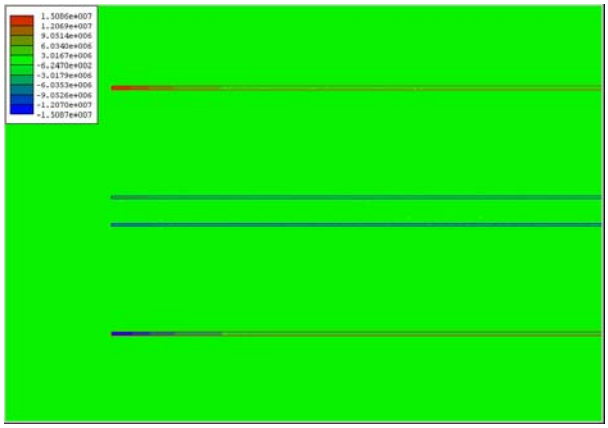

Figure 6-16: Current density distribution inside conductors at 1MHz (Only one edge of a cross section is shown).

Basically, this type of integrated RF EMI filter behaves like a R-C filter but with a variable resistance with frequency, as shown in Figure 6-17. Certainly, the mechanism of

this filter is far more complex than a R-C filter due to the presence of inductance and magnetic couplings as will be discussed next.

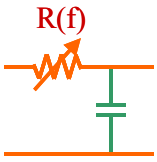

Figure 6-17: Behavioral model of an integrated RF EMI filter.

To study the effect of losses of the nickel layer on the filter performance, the filter transfer gain with different nickel ac resistance has been calculated, as shown in Figure 6-18. Apparently, a filter with a more lossy nickel layer demonstrates a higher roll-off slope.

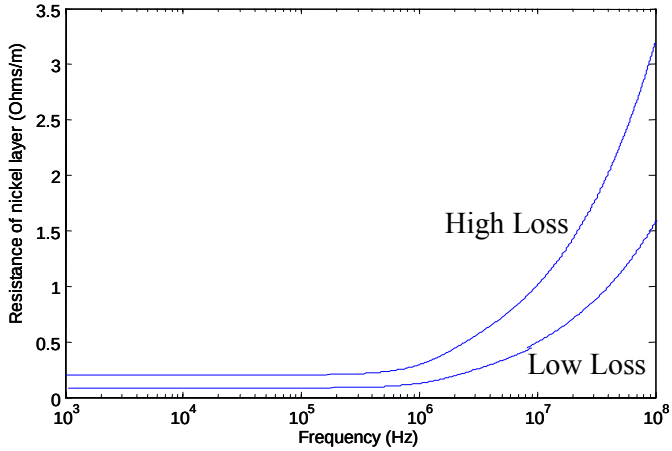

(a) Resistance of the nickel layer as a function of frequency

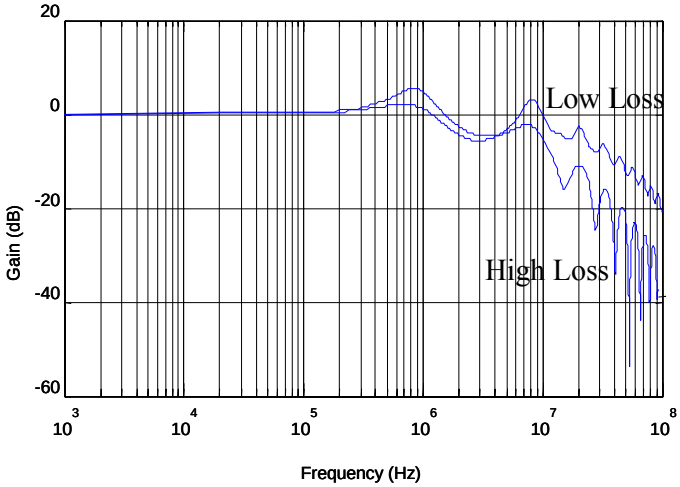

(b) Filter transfer gain with different attenuation.

Figure 6-18: Effect of nickel layer resistance on the filter transfer gain.

On the other hand, the characteristic impedance of the filter element is another key factor to consider in the design. As shown in Figure 6-19, lower the characteristic impedance does help to achieve a higher attenuation at high frequency provided the same losses on each layer.

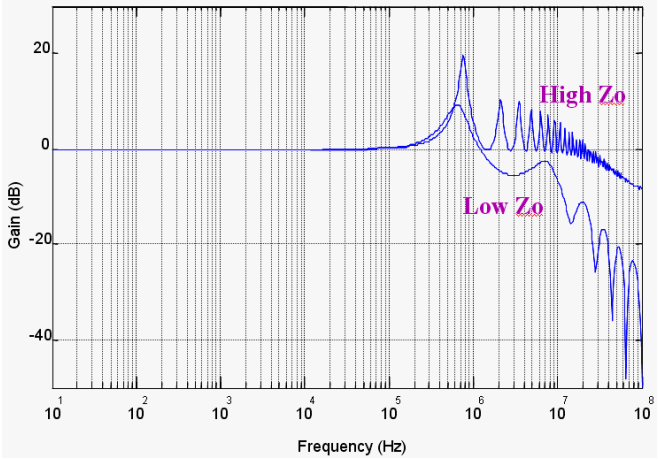

Figure 6-19: Effect of filter element characteristic impedance on the filter transfer gain.

The integrated DM RF-EMI filter, basically a four-conductor structure, can be viewed as two two-conductor transmission structures with magnetic coupling between each other, as shown in Figure 6-20.

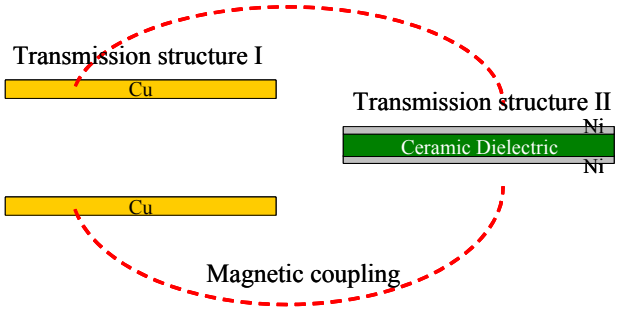

Figure 6-20: Two-conductor transmission structure representation of an integrated RF-EMI filter.

At low frequency, it demonstrates the characteristics of transmission structure I. However, with the current more and more concentrating in the inner nickel layers with increasing frequency, its behavior becomes more and more similar to that of transmission structure II.

There are two types of approaches to improve the high frequency damping factor: one is increasing the losses on the nickel layer, the other is reducing the characteristic impedance of transmission structure II.

In order to enhance the losses hence the proximity effect on the nickel layers, the magnetic flux generated by transmission structure I must be enhanced. A simple way to achieve that is reducing the width of the copper layers of transmission structure I. Certainly, the thickness of the copper layer should be increased at the same time to assure the same current density.

In order to reduce the characteristic impedance, the best way is to increase the width of the nickel layers and decrease the thickness of the dielectric layer.

From the discussion above, reducing the quality factor Q of the filter element is the key to achieve higher attenuation at high frequency. The practical approaches to realize that is summarized in Figure 6-21.

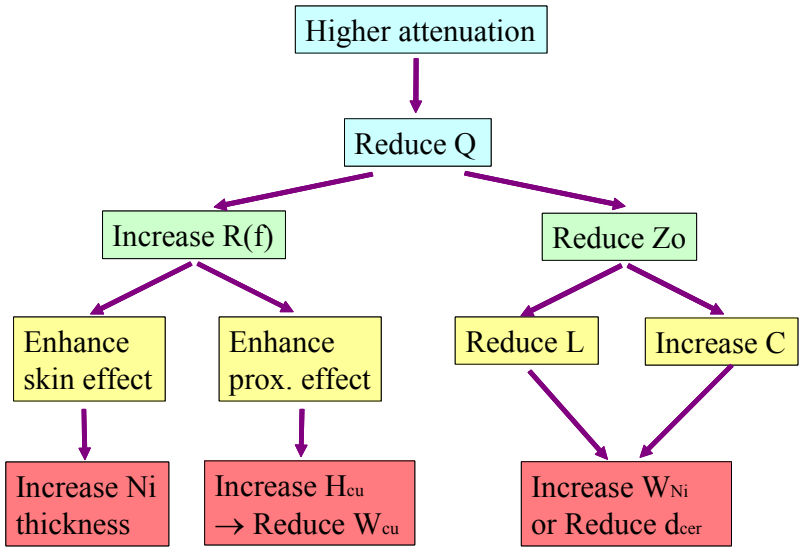

Figure 6-21: Approaches to achieve higher attenuation.

6.5. Proposed New Structure

Figure 6-18 shows that increasing the resistance of the nickel layer does help to enhance the high frequency attenuation. This may be achieved by changing the configurations or dimensions of the filter structure, for example, reducing the copper

width, as described in Figure 6-21. As shown in Figure 6-22, keeping the width of the nickel layers as 10mm, the nickel power losses at 1MHz (MAXWELL 2D simulation) increase with a decreasing copper width. That ends up with a structure having wide and thin nickel layers but narrow and thick copper layers, as shown in Figure 6-23.

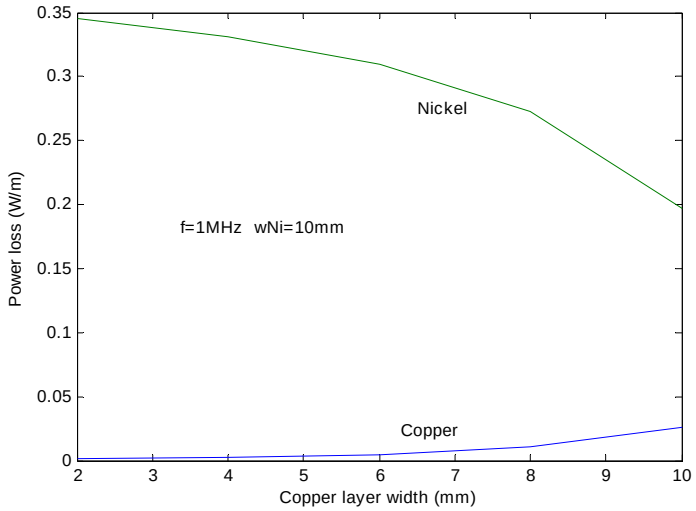

Figure 6-22: The power losses in each layer versus copper width.

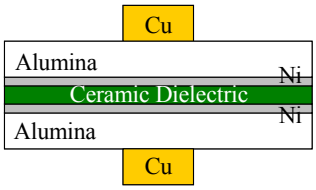

Figure 6-23: Proposed higher attenuation filter structure.

The picture and dimensions of an prototype of the proposed integrated RF-EMI filter is shown in Figure 6-24.

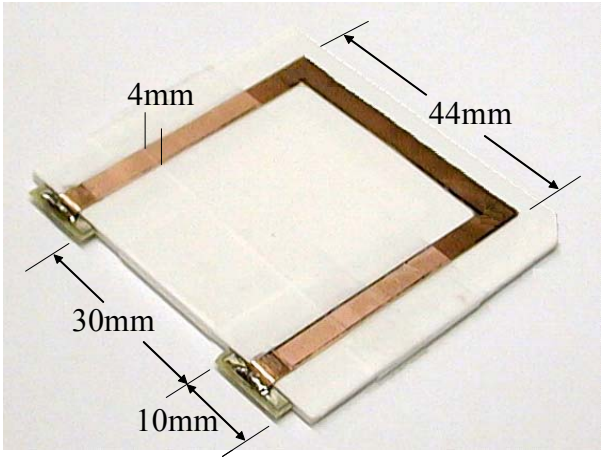

Figure 6-24. The prototype of an integrated RF EMI filter.

Some technical parameters are shown in Table 6-2.

Table 6-2: Technical parameters of the RF-EMI filter prototype

Ceramic dielectric material (middle layer)	Y5V ($BaTiO_3$)
ε_r of the dielectric material (middle layer)	14000 (nominal)
Thickness of the dielectric material (middle layer) h_{BaTiO3}	0.15mm
Loss factor of the $BaTiO_3$ layer $\tan\delta_1$	1%
Thickness of the Alumina layer $h_{Alumina}$	0.65mm
ε_r of Alumina	9.9
Loss factor of Alumina $\tan\delta_2$	0.01%
Copper layer thickness	≈ 60μm
Nickel layer thickness	≈ 17μm
Copper layer width wCu	4mm
Nickel layer width wNi	10mm
Total length of the structure	130mm

The measured transfer gain with the proposed structure are shown in Figure 6-25. Both of the measurements have a standard 50 Ω impedance as the load. From Figure 6-12, the transfer gain of the conventional structure achieves an attenuation of -55dB at 100MHz. As an improvement, the transfer gain of the proposed structure achieves an attenuation of -60dB at 100MHz. Also superior to that of the conventional structure, the maximum attenuation of the proposed structure reaches below -70dB.

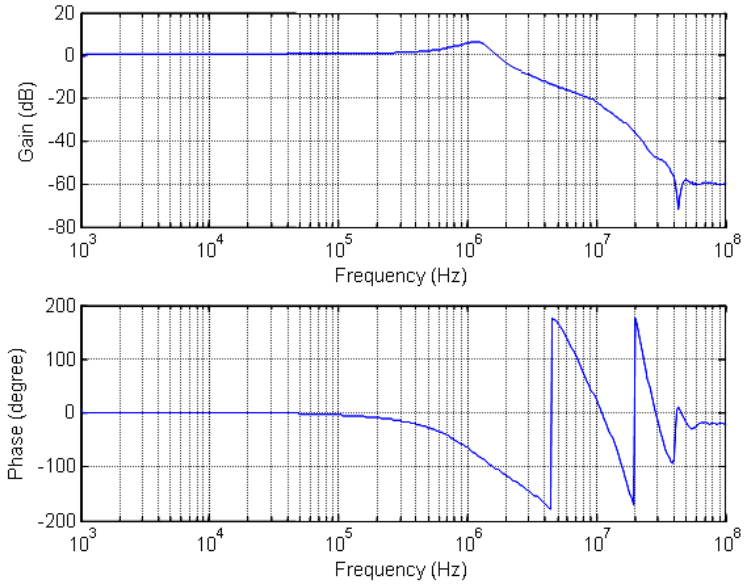

Figure 6-25: Measurement results of transfer gain at Z_L=50Ω with the proposed structure.

6.6. Conclusion

This chapter presents the modeling of an integrated RF-EMI filter based on generalized multi-conductor transmission structure theory. As two remarkable improvements with the proposed model, the measurement issues and high frequency proximity effect have been taken into account. Compared to the previous lumped model and two-conductor-transmission line-based model, the proposed model has shown a more promising prediction on the high frequency characteristics of the integrated filter. As part of the future work, the high frequency loss modeling still needs to be improved for a better accuracy. Some design-oriented issues have also been discussed.

Chapter 7: Simplified Equivalent Circuit Model for Integrated Power Passives

7.1. Introduction

The frequency plane modeling of integrated passives structures based on generalized transmission structure theory have been presented in Chapter 3 and Chapter 4. However, the calculation based on matrix modal analysis is rather complex and takes a lot of computer time especially when the number of turns is large. Furthermore, the operating frequency of an integrated resonant module is normally around its 1st resonant frequency and hardly goes to the 2nd resonant frequency. Therefore, a more simplistic higher order lumped element model which covers the operating range up to the 2nd resonant frequency may be good enough for the general design purpose.

Typical impedance of an integrated series resonant module is shown in Figure 7-2. Its first order approximation model is given in Figure 7-2(a) which can be further simplified to Figure 7-2(b). However, this model neglects the existing high frequency impedance peak as illustrated in Figure 7-2 at f_p and shows an ideal series resonator behavior at high frequency as shown in the dotted curve in Figure 7-2. As discussed in Chapter 4, the high frequency 2nd resonant peak is caused by the parallel resonance between the winding inductance and the inter-winding capacitance. This chapter focuses on the calculation of the inter-winding capacitance on which the higher order lumped equivalent circuit is based. As substantiated by small-signal measurement, this model can be applied to both conventional spiral winding structure and multi-cell structure integrated passive components.

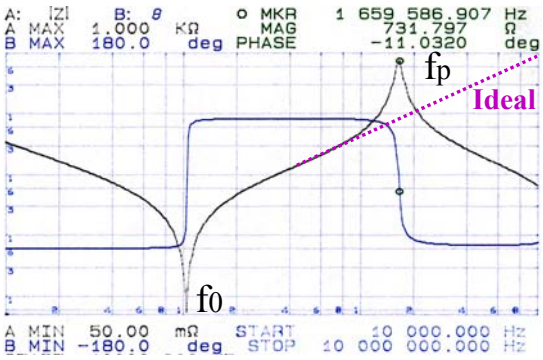

Figure 7-1: Typical impedance of an ISRM

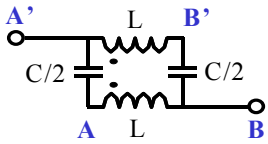

(a) The previous 1st order approximation model

(b) The previous ideal model

Figure 7-2: 1st order approximation lossless model.

7.2. Inter-winding Capacitance Calculation

As discussed in the previous section, the high frequency impedance peak can be modeled as a parallel resonance between the winding inductance and the inter-winding capacitance. It is now necessary to examine the exact planar structure to establish the nature of this capacitive coupling.

7.2.1. Inter-winding Capacitance Calculation -Conventional Spiral Winding Structure

As illustrated in section 3.2, the in-plane capacitance (see Figure 3-3) between two adjacent L-C cells can be calculated using the Schwartz-Christoffel transformation. To apply the calculation results to the physical spiral winding structure integrated power passives, a 2-turn structure shown in Figure 7-3(a) is taken into investigation as a preliminary example. The winding consists of four sections of coplanar transmission lines and a single capacitor $C_{1,1}$ which contribute to the generation of inter-winding capacitance. Since most of the total inductance is generated by the winding inside the core, the two sections of coplanar transmission lines outside the core may be simplified as capacitors, too. The whole winding on one side of the ceramic dielectric substrate can be modeled as coplanar transmission lines cascaded with capacitors with point C connected back to D, as illustrated in Figure 7-3(b) and (c).

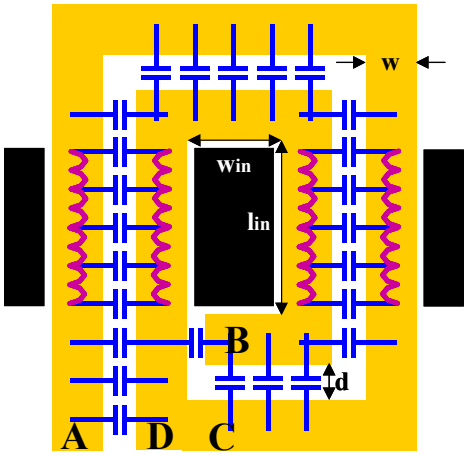

(a) Winding top view with distributed parameters

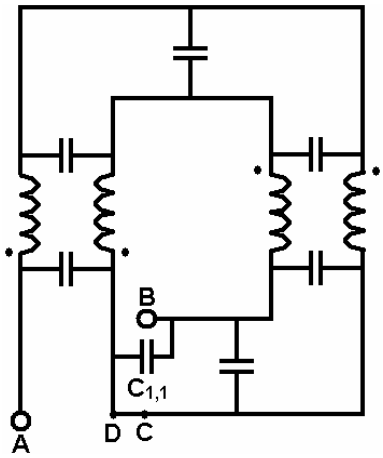

(b) Cascaded transmission line model

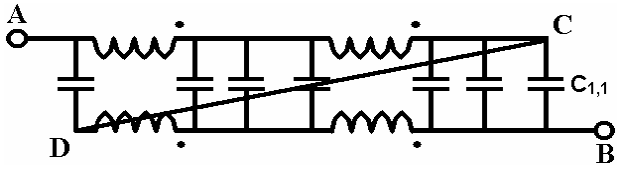

(c) Unwound cascaded transmission line model

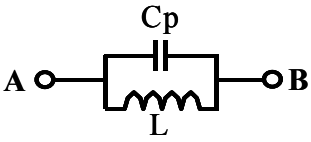

(d) Lumped model

Figure 7-3: Cascaded transmission line model for a 2-turn conductor winding on one side of the ceramic dielectric substrate.

With the same principle, the transmission-line-based model for a multi-turn conductor winding on one side of the ceramic dielectric substrate is shown in Figure 7-4(a). The lumped model is a parallel LC structure, as shown in Figure 7-4(b).

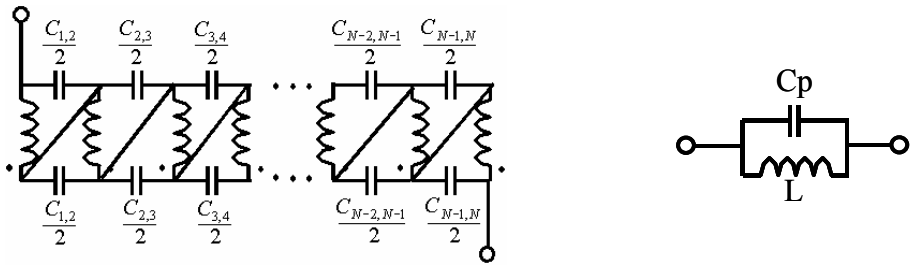

(a) Transmission-line-based model (b) Lumped model

Figure 7-4: Multi-turn winding model for conductor on one side.

With C_{gd} known, C_p can be obtained by

$$C_p = \begin{cases} C_{1,1} & N = 1 \\ \dfrac{1/2}{\dfrac{1}{C_{1,2}} + \dfrac{1}{C_{1,2}+C_{2,3}} + \cdots + \dfrac{1}{C_{N-2,N-1}+C_{N-1,N}} + \dfrac{1}{C_{N-1,N}}} & N > 1 \end{cases} \tag{7-1}$$

in which,

$$l_{1,1} = w,\ l_{n,n+1} = 2(w_{in} + l_{in}) + 8w + 8(n-1)(w+d) \quad \text{(n=1, 2, 3…, N-1)} \tag{7-2}$$

$$C_{1,1} = C_{gd} \cdot l_{1,1} \tag{7-3}$$

$$C_{n,n+1} = \begin{cases} C_{1,1} + C_{gd} \cdot l_{n,n+1} & n = 1 \\ C_{gd} \cdot l_{n,n+1} & n = 2, 3, 4, \ldots, N-1 \end{cases} \tag{7-4}$$

7.2.2. Inter-winding Capacitance Calculation - Multi-cell Structure

The inter-winding capacitance calculation of a multi-cell structure integrated series resonant module is very similar to that of a spiral-winding structure as shown in section 7.2.1. The top view of the winding pattern of an N-cell structure integrated series resonator is shown in Figure 7-5 on which the PCB interconnections underneath the core are represented in dotted lines. In terms of the conductor on one side of the dielectric substrate, it has the same form of equivalent circuit as shown in Figure 7-4.

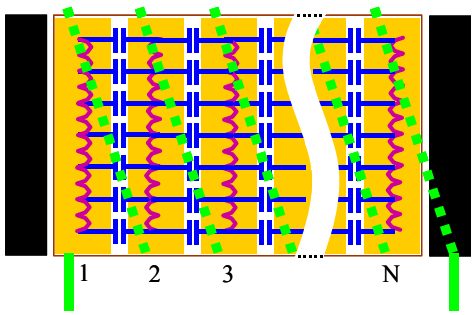

Figure 7-5: Winding top view with distributed parameters: multi-cell structure.

With C_{gd} known, C_p can be obtained by

$$C_p = \begin{cases} 0 & N = 1 \\ \dfrac{1/2}{\dfrac{1}{C_{1,2}} + \dfrac{1}{C_{1,2}+C_{2,3}} + \cdots + \dfrac{1}{C_{N-2,N-1}+C_{N-1,N}} + \dfrac{1}{C_{N-1,N}}} & N > 1 \end{cases} \tag{7-5}$$

in which,

$$C_{n,n+1} = C_{gd} \cdot l \quad (n=1,2,3,4\ldots N-1) \tag{7-6}$$

7.3. The Complete Higher Order Impedance Model

In order to include the behavior of the high frequency resonant peak shown in Figure 7-1, the 1st order approximation model for an integrated series resonant module in Figure 7-2(a) can be improved by adding a parallel capacitor to the inductor on each side while taking the losses into account, as shown in Figure 7-6. The two inductors refer to the top and bottom conductor windings, respectively. Each of the winding has an inherent inter-winding capacitance C_p as discussed in section 7.2. Between the top and bottom conductor windings, there is a total series resonant capacitance C which has been equally split into two capacitors, representing the distribution of the capacitance C. R_L represents the copper and core losses associated with the windings while G_C represents the dielectric losses.

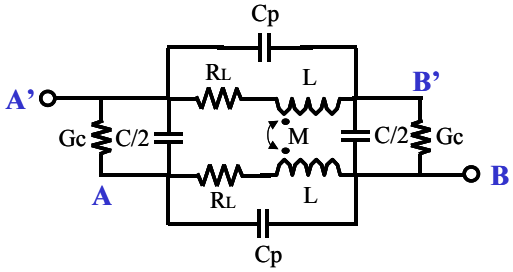

Figure 7-6: The complete higher order equivalent circuit of an ISRM.

In Figure 7-6, the series resonant capacitance

$$C = \frac{\varepsilon_0 \varepsilon_r l_c w}{t} \tag{7-7}$$

in which, the winding conductor length

$$l_c = 2N(w_{in} + l_{in}) + 4N(N+1)(w+d) - 4N \cdot w - (8N+1)d \tag{7-8}$$

The total impedance of an ISRM from the equivalent circuit model in Figure 7-6 is given by

$$Z_{A'B} = \frac{1}{2G_C + j\omega C} + \frac{1}{\dfrac{1}{\dfrac{R_L + j\omega(L+M)}{2}} + j\omega(2C_p)} = Z_0 \left[\frac{1}{j\dfrac{\omega}{\omega_0} + Q(2G_C R)} + \frac{1}{\dfrac{1}{\dfrac{1}{Q}\left(\dfrac{R_L}{2R}\right) + j\dfrac{\omega}{\omega_0}}} + j\frac{\omega}{\omega_0}\left(\frac{\omega_0}{\omega_{01}}\right)^2 \right] \tag{7-9}$$

in which,

the series resonant frequency

$$\omega_0 = 2\pi f_0 = \frac{1}{\sqrt{\dfrac{L+M}{2} C}} \tag{7-10}$$

the parallel resonant frequency

$$\omega_{01} = 2\pi f_{01} = \frac{1}{\sqrt{\dfrac{L+M}{2} 2C_p}} = \frac{1}{\sqrt{(L+M)C_p}} \tag{7-11}$$

the characteristic impedance

$$Z_0 = \omega_0 \left(\frac{L+M}{2} \right) = \frac{1}{\omega_0 C} = \sqrt{\frac{L+M}{2C}} \tag{7-12}$$

the quality factor

$$Q = \frac{Z_0}{R} = \frac{\omega_0 (L+M)}{2R} = \frac{1}{\omega_0 CR} \tag{7-13}$$

the total resistance

$$R = \frac{1}{2}(R_L + G_C) \tag{7-14}$$

From equation (7-9), it is obvious that a series resonance will occur at $\omega=\omega_0$ and a parallel resonance will occur at $\omega=\omega_{01}$.

7.4. Case Study

7.4.1. Conventional Spiral Winding Structure

A 3-turn integrated series resonant module prototype has been constructed with its pictures and parameters shown in Figure 4-3 and Table 4-1, respectively.

According to the equations in section 3.2, 7.2.1 and 7.3, the calculation results for series and parallel capacitance are C=420nF and C_p=748pF, respectively. They are very close to the impedance analyzer test results C=437nF and C_p=760pF. The inductance L≈M=10.9μH. The power losses estimation is based on equations of [5][24]. The simulation results based on the model in Figure 7-6 and the impedance analyzer test results are compared in Figure 7-7. It can be seen that the measured series resonance occurs at f_s=72.9kHz and the parallel resonance at f_p=1.22MHz which fit the calculation results f_s=74.7kHz and f_p=1.25MHz very well. As an improvement, the calculation results based on the proposed higher order model predict the occurring of both the series resonance and the high frequency parallel resonance.

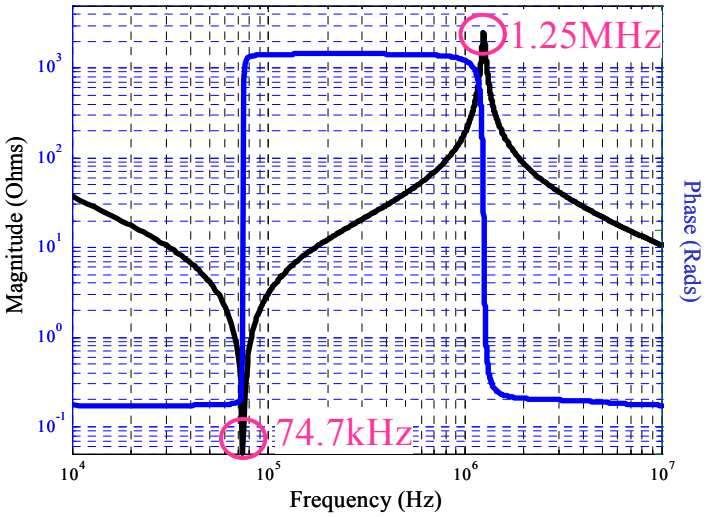

(a) Simulation results

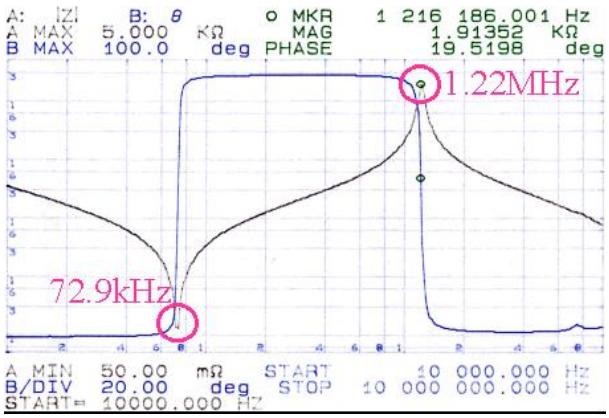

(b) Impedance analyzer measurement results

Figure 7-7: Simulation results and the small-signal test results.

7.4.2. Multi-cell Structure

A 5-cell integrated series resonant module prototype has been constructed with its pictures and parameters shown in Figure 7-8 and Table 7-1, respectively.

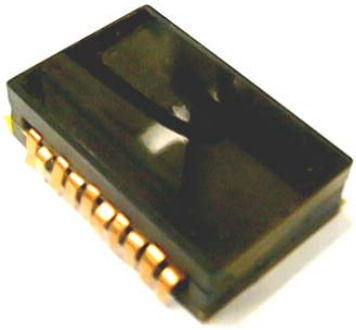

(a) External view

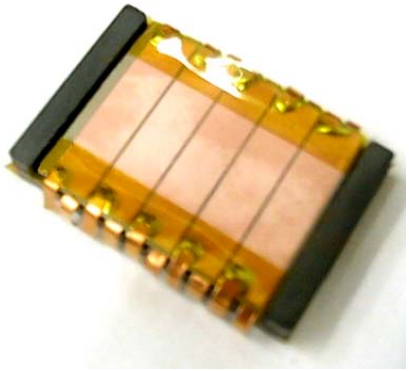

(b) Internal view

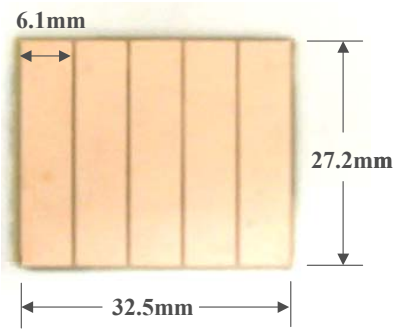

(c) Dimensions

Figure 7-8: Pictures of the prototype.

Table 7-1: Technical parameters for the module

Magnetic core	Philips E43/10/28-3F3 (center leg removed) and PLT43/28/4-3F3
Air gap	≈80μm
Dielectric material	Y5V
ε_r of the dielectric material	14000 (nominal)
Dimensions of the ceramic substrate	28mm×33mm×0.33mm
tanδ of the dielectric material	1% at 1MHz
Width of the copper strips	≈6.1mm
Copper thickness	≈50μm
Dimensions of the module	28mm×43mm×12mm

The calculation results and the impedance analyzer test results are compared in Figure 7-9. It can be seen that the measured series resonance occurs at f_s=70kHz and the parallel resonance at f_p=2.35MHz which fit the simulation results f_s=68.5kHz and f_p=2.25MHz very well.

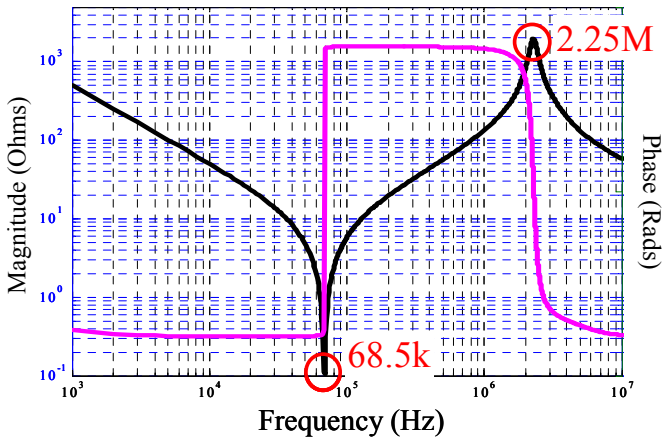

(a) Simulation results

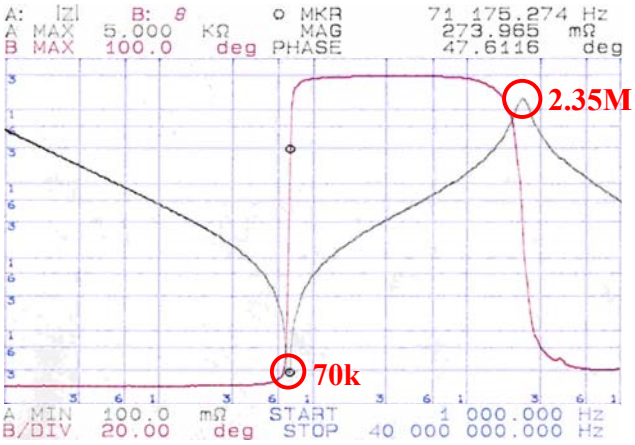

(b) Impedance analyzer measurement results

Figure 7-9: Simulation results and the small-signal test results.

7.5. Discussion

Figure 7-10 shows the variation of C_p with the spacing between turns d and number of turns, with given specifications and variable permittivity. Apparently, C_p always drops with d. Increasing d is probably the most effective method to reduce the inter-winding capacitance.

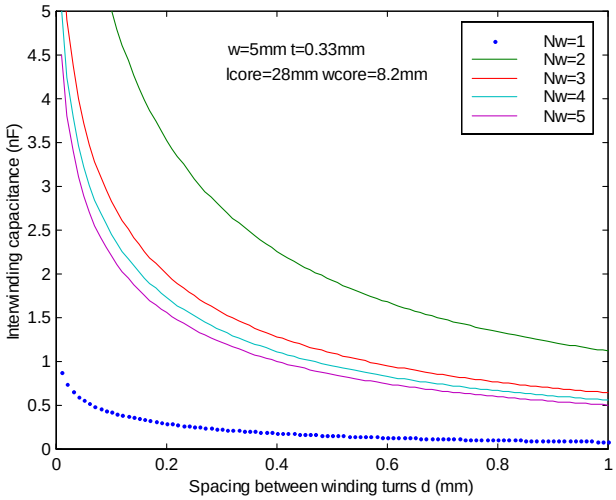

Figure 7-10: Inter-winding capacitance versus d with various numbers of turns.

Figure 7-11 shows the characteristics of inter-winding capacitance as a function of core aspect ratio (the ratio of the width to the length of the core center leg) with various numbers of turns. It has the same specifications but d is fixed as 0.5mm.

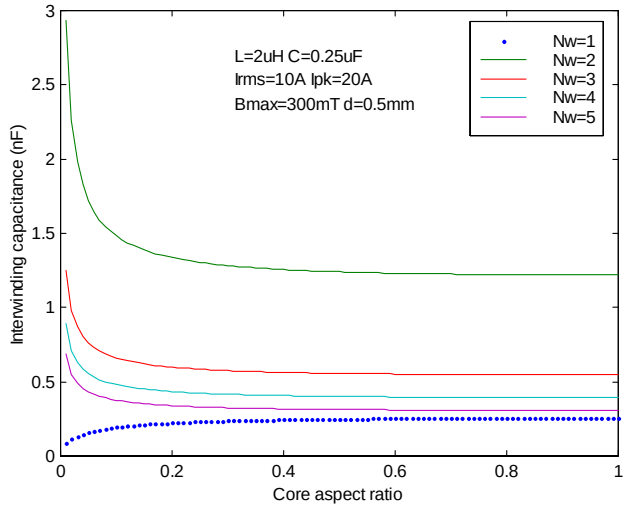

Figure 7-11: Inter-winding capacitance versus core aspect ratio with various N.

From Figure 7-10 and Figure 7-11, it is obvious that the total inter-winding capacitance when N>1 decreases with the number of turns. Actually, the inter-winding capacitance C is proportional to 1/N, provided each turn has the same length. However, the inductance increases with the number of turns with a higher order, or $L \propto N^2$. Therefore, the parallel frequency will move to a lower frequency increasing the number of turns even if the inter-winding capacitance itself becomes lower.

The best method to reduce C_p may be cutting of the extra dielectrics between windings. But this leads to higher complexity and lower reliability, thus needs further evaluation. Though increasing d and core aspect ratio will help to reduce C_p, they may increase the total volume.

7.6. Conclusion

A higher order frequency plane model for integrated series resonant module as an example of integrated power passives has been presented in this chapter. A transmission-line-based lumped model of the conductor windings on ceramic dielectric substrate has been proposed. The calculation of the inter-winding capacitance in this model is based on Schwarz-Christoffel transformation (see Chapter 3). This model has been verified by small-signal test results and can be easily implemented into the design algorithm as part of the high frequency design considerations. Some practical design issues have also been

discussed. It is possible to apply the modeling approach to more complicated integrated structures.

Chapter 8: Conclusion

8.1. Introduction

This dissertation can be divided into three main sections. The first section is devoted to the generalized transmission structure model, for both two-conductor and multi-conductor structures. Applying the models in the first section to practical structures, the case studies on frequency plane modeling of the spiral winding structure and multi-cell structure integrated passive modules as well as the integrated RF-EMI filter form the second section of this dissertation. This also includes design issues, practical implementation and test of the multi-cell integrated reactive components. The third and last section is concerned with an improved lumped circuit model other than a distributed circuit model given in previous sections. This aims to simplify the calculation and make it easier to be implemented in design software for general design purpose. This concluding chapter serves as a short summary and evaluation of each section, and some suggestions for future work are given.

8.2. Generalized Transmission Structures

This section treats the modeling of integrated electromagnetic power passives for integrated power electronics modules by using a distributed conductive structure approach. The distributed L-C cell is chosen as the basis for any further modeling. This section presents the modeling of an L-C cell through the proposed generalized transmission structure theory that can be applied to both balanced and unbalanced current distributions. A generalized transmission structure without load shows series resonant characteristics while shows parallel resonance with a short-circuited load. The calculation results correlate well with the impedance measurement results. It is also useful to facilitate the practical design.

The proposed theory has been extended to cascaded structures and multi-conductor structures as well. In a multi-conductor transmission structure, a bunch of parallel

conductors with the same length may have both magnetic and capacitive coupling between each other. As one of the most important steps in determining the capacitive coupling between conductors of a basic building block, capacitance between two adjacent conductor strips on the same side of a dielectric substrate can be calculated by Schwartz-Christoffel transformation. Having multiple variables coupled with each other, the voltage and current equations can be written in a matrix form and modal analysis has been employed. The relationship between voltages and currents at different positions of the transmission structures can be obtained by matrices manipulations.

8.3. Case Studies: Frequency Plane Modeling of Integrated Passive Modules

Practical integrated passives structures generally can be treated as one or more of multi-conductor transmission structure section(s) connected with each other in certain patterns. From a mathematic point of view, different structures only lead to different boundary conditions.

Firstly, the conventional spiral winding structure integrated passives has been modeled based on the proposed generalized transmission structures. The spiral winding of an integrated SR module can be divided into 5 sections, two in-core sections (B and D) and three overhang sections (A, C and E). An impedance transformation has been conducted to map section A, C and E into the corresponding equivalent multi-conductor transmission structures in which all the conductors in each section are in the same length. Impedance of the structure can be obtained by applying the voltage and current boundary conditions to the transmission structure equations. The calculation has been verified by small-signal measurement results. The causes of the resonance at different frequency range have been identified.

Secondly, an alternative approach to construct a planar integrated reactive power module is presented in this section. Enclosed in a planar core, a few copper strips plated on both sides of a high permittivity ceramic substrate generate a series of so-called L-C cells. Various equivalent circuits may be realized with this chip-like module using different PCB interconnections between the L-C cells. The experimental results show its

potential as an integrated high frequency power resonator. Some advantages and potential advantages of these structures are:

1) Potentially higher power density than the previous structures due to the different active volume arrangement.
2) Better mechanical properties (less mechanical stress, better protection of the ceramic tiles, etc.).
3) Potentially improved manufacturability and modularization.
4) Multi-functionality.
5) The potential to achieve true 3-D-integrations, since the vertical dimension is used for interconnection.

The part inside the core of a multi-cell structure is a simple multi-conductor transmission structure. Modal analysis is used to solve the matrix equations. The determination of boundary conditions on the ends of each L-C cells should consider the voltage drop at PCB interconnections as well. The MATLAB simulation results correlate well with the measurement results.

Thirdly, the multi-conductor generalized transmission structure model has been applied to an integrated RF EMI filter. It is basically a four-conductor structure: two nickel layers sandwiching a high permittivity ceramic dielectric substrate and two copper layers placed on both sides of the substrate with Alumina (or other insulation materials) layers in between as insulations. Utilizing the high frequency proximity effect, it is able to achieve high attenuation at high frequencies without affecting the low frequency conducting feature. Compared to the previous lumped model and two-conductor-transmission line-based model [23], the proposed model has taken proximity effect and measurement issues into account, therefore demonstrated a more promising prediction on the high frequency characteristics of the integrated filter. However, the high frequency loss modeling still needs to be improved for a better accuracy. Based on the electromagnetic losses simulation results, a new structure that may achieve a higher attenuation at high frequencies has been proposed and investigated.

8.4. An Improved Lumped Circuit Model for Integrated Passive Modules

This section presents a higher order frequency plane model for integrated series resonant module. The cause for the occurring of the high frequency impedance peak is identified as the parallel resonance between the winding inductance and its inter-winding capacitance. The inter-winding capacitance can be calculated from a transmission-line-based lumped model using Schwartz-Christoffel transformation. This model simplifies the calculation significantly compared with the distributed transmission structure model while improving the accuracy by one order compared to the conventional first order approximation model. Not only the fundamental resonance, but also the parallel resonant peak can be covered in the calculation. This is sufficient for most of the general-purpose designs to evaluate the high frequency performance and can be easily implemented in the design-oriented algorithm to facilitate the design and optimization of an ISRM due to the dramatic saving of computer time.

Bibliography

[1] J. D. van Wyk, J. A. Ferreira, "Some present and future trends in power electronic converters," *Proc. IEEE IECON'92*, vol. 1, pp. 9-15, 1992.

[2] I. Hofsajer, J. D. van Wyk, J. A. Ferreira, "Functional component integration in a multi-kilowatt resonant converter," *Proc. EPE'93*, vol. 2, pp. 125-130, 1993.

[3] K. Laouamri, J. C. Crebier, J.-P. Ferrieux, T. Chevalier, "Construction and modeling of integrated LCT structure for PFC resonant converter," *Proc. of PESC'01*, vol. 4, pp. 1949 –1954, 2001.

[4] S. J. Marais, J. A. Ferreira, J. D. van Wyk, "Planar integrated output filters for hybrids," *Proc. PESC'97*, vol. 2, pp. 1143-1149, 1997.

[5] L. Zhao, J. T. Strydom, J. D. van Wyk, "Design considerations for an integrated LC resonant module," *Proc. 2000 CPES Power Electronics Seminar*, pp. 355-359, Sept. 17-19, 2000.

[6] L. Zhao, J. T. Strydom, J. D. van Wyk, "An integrated resonant module for a high power soft-switching converter," Proc. PESC'01, vol. 4, pp. 1944 -1948, 2001.

[7] M. C. Smit, J. A. Ferreira, J. D. van Wyk, "Modeling and technology evaluation for integrated resonance components," *D.Eng. Dissertation*, Rand Afrikaans University, 1994.

[8] R.J. Kemp, P.N. Murgatroyed, N.J. Walker, "Self resonance in foil inductors," *Electronics Letters*, vol. 11, No. 15, pp. 337-338, July 1975.

[9] R. Reeves, "Inductor-capacitor hybrid," *Proc. IEE*, vol. 122, No. 11, pp. 1323-1326, November, 1975.

[10] O.H. Stielau, J. D. van Wyk, M. Ehsani and I, J. Pitel "Integrated reactive components in power electronic circuits*," Record of IEEE Power Electron. Spec. Conf*., vol. 2, pp. 831-838, 1990.

[11] M. C. Smit, J. A. Ferreira and J. D. van Wyk, "Application of transmission line principles to high frequency power converters," *Proc. PESC'92*, vol. 2, pp. 1423-1430, 1992.

[12] R. Chen, J. T. Strydom, J. D. van Wyk**, "**Design of planar integrated passive module for zero-voltage-switched asymmetrical half-bridge PWM converter," IEEE Trans. on Industry Applications, vol. 39, No. 6, pp. 1648-1655, Nov.-Dec., 2003.

[13] J. Smit, J. A. Ferreira, J. D. van Wyk and M. Ehsani, "A new ultrasonic series resonant converter with integrated LCT*," Record of IEEE Power Electron. Spec. Conf*., vol. 2, pp. 729-733, 1990.

[14] M. C. Smit, J. A. Ferreira, J. D. van Wyk, "Technology for manufacture of integrated planar LC structures for power electronic applications," *Proceedings EPE 93*, Brighton, vol. 2, pp. 173-178, September 1993.

[15] N. Murgatroyed, N.J. Walker, Lumped circuit model for inductor-capacitor hybrid, *Electronics Letters*, vol. 12, No. 1, pp. 2-3, Jan. 1976.

[16] O.H. Stielau, "High frequency, high power resonant electronic converter for induction heating," *D. Eng. thesis*, Industrial and Electronics Technology Research Group, Faculty of Engineering, Rand Afrikaans University, Jan. 1991.

[17] M. Ehsani, P. Le Polles, M. S. Arefeen, I. J. Pitel and J. D. van Wyk, "Computer-aided design and application of integrated LC filters," *IEEE Trans. on Power Elect.*, vol. 11, No. 1, pp. 182-190, 1996.

[18] J. T. Strydom, J. D. van Wyk, "Improved loss determination for planar integrated power passive modules," *Seventeenth Annual IEEE Applied Power Electronics Conference and Exposition*, vol. 1, pp. 332 –338, 2002.

[19] S. J. Marais, J. A. Ferreira, "A new approach to model component parasitics," Conference Record of the 1995 IEEE Thirtieth IAS Annual Meeting, vol. 2, pp. 1031 –1037, 1995.

[20] M. Shoyama, K. Harada, et al., "Voltage resonant buck-boost converter using multi-layer-winding transformer," *Conf. Rec. Power Electronics Specialists Conf. (PESC '89)*, Milwaukee, WI, pp. 895-901, June 1989.

[21] R. Chen, F. Canales, B. Yang, P. Barbosa, J. D. van Wyk, F. C. Lee, **"**Integration of electromagnetic passive components in DPS front-end DC/DC converter - a comparative study of different integration steps," *the Eighteenth Annual IEEE Applied Power Electronics Conference and Exposition (APEC '03),* vol. 2, pp. 1137–1142, 9-13 Feb. 2003.

[22] J. D. van Wyk, Jr., P. J. Wolmarans, J. D. van Wyk, W. A. Cronje, "Integrated RF-EMI transmission line filters for integrated power electronics modules," *Proc. CPES Seminar 2002*, pp. 439-444, Blacksburg, VA, April 14-18, 2002.

[23] P. J. Wolmarans, J. D. van Wyk, J. D. van Wyk, Jr.; C. K. Campbell, "Technology for integrated RF-EMI transmission line filters for integrated power electronic modules," *Conference Record of the 37th IAS Annual Meeting of the Industry Applications Society*, vol. 3, pp. 1774 –1780, 2002.

[24] L. Zhao, J. T. Strydom, J. D. van Wyk, "Optimization and design of an integrated L-C resonant module for medium and high power applications," Proc. PESC'01, vol. 2, pp. 594-599, 2001.

[25] I. W. Hofsajer, J. A. Ferreira, J. D. van Wyk, "Design and analysis of planar integrated L-C-T components for converters," *IEEE Trans. on Power Electronics*, vol. 15, No. 6, pp. 1221-1227, 2000.

[26] S. R. Seshadri, *Fundamentals of Transmission Lines and Electromagnetic Fields*, Addison-Wesley Publishing Company, 1971.

[27] L. Zhao, J. T. Strydom, J. D. van Wyk, "An alternative planar multi-cell structure integrated reactive module," *Conference Record of the Thirty-Sixth IEEE IAS Annual Meeting*, vol. 4, pp. 2217-2223, 2001.

[28]. H. Nishiyama and M. Nakamura, "Capacitance of a strip capacitor," IEEE Transactions on Components, Hybrids, and Manufacturing Technology, vol. 13, No. 2, pp. 417-423, 1990.

[29] Harris Hancock, *Elliptic integrals*, John Wiley & Sons, Inc., 1917.

[30] Paul F. Byrd, Morris D. Friedman, *Handbook of elliptic integrals for engineers and scientists*, Springer - Verlag New York Heidelberg Berlin, 1971.

[31] Harry Urkowitz, "Capacitance between thin film conductors deposited on a high-dielectric-constant substrate," *Proc. of the IRE*, V.50, pp. 2142-2143, 1962.

[32] J. A. Brandão Faria, *Multiconductor transmission-line structures: Modal analysis techniques*, John Wiley & Sons, Inc. 1993.

[33] C. R. Sullivan and S. R. Sanders, "Design of microfabricated transformers and inductors for high-frequency power conversions," *IEEE Trans. Power Elect.*, vol. 11, no. 2, pp. 228-238, 1996.

[34] W. M. Chew and P. D. Evans, "High frequency inductor design concepts," *Proc. 22nd Annu. Power Electronics Specialists Conf.*, pp. 673-678, 1991.

[35] J. Hu and C. R. Sullivan, "The quasi-distributed gap technique for planar inductors: design guidelines," Proc. *IEEE Industry Applications Soc. Annu. Meeting*, pp. 1147-1152, 1997.

[36] Marian K. Kazimierczuk, Dariusz Czarkowski, *Resonant power converters,* Singapore: John Wiley & Sons, 1995.

[37] L. Zhao, J. T. Strydom, J. D. van Wyk, "The Modeling of Planar Multi-cell Integrated Reactive Components Based on Multi-conductor Generalized Transmission Structure Theory," *Conference Record of the Thirty-Seventh IEEE IAS Annual Meeting*, vol. 3, pp. 1787 –1794, 2002.

[38] W. G. Odendaal, "A generic approach for the modeling of high power density magnetic components," *D Ing Dissertation,* Faculty of Engineering, Rand Afrikaans University, Johannesburg, South Africa, 1997.

Vita

The author, Lingyin Zhao, was born in May 1975 in Xi'an, P. R. China. He received the B.S. degree from Zhejiang University, Hangzhou, China, in 1996, and the M.Eng degree from Nanyang Technological University, Singapore, in 1999, both in electrical engineering. In 1999, the author came to the Center for Power Electronics Systems (CPES), Virginia Polytechnic Institute and State University for his Ph. D. study. He completed this work in May 2004.